
# Instrumentation development and experimental design for a next generation detector of the highest energy cosmic rays.

Clement Laurence Stephen Pryke

February 1996

*Submitted in accordance with the requirements*
*for the degree of Doctor of Philosophy.*

The University of Leeds
Department of Physics

The candidate confirms that the work submitted is his own and that appropriate credit has been given where reference has been made to the work of others.

# Abstract

There is currently great international interest in the construction of a next generation detector of the highest energy cosmic rays ($> 10^{19}$ eV). Due to the extremely low rate of these events such a device must have an effective aperture of $\sim 10,000$ km$^2$ sr. The implementation of a classical ground array of particle detector units covering such an area is now possible at realistic cost due to recent technological advances. The conceptual design is for a system of semi-autonomous detector stations linked by a digital radio communications network, powered by solar cells, and with data acquisition synchronized through the use of satellite receivers. Chapter 1 discusses the background to, and reasoning behind, the proposed experiment; the remainder of this thesis concerns development work towards its realization.

In Chapter 2 the development of techniques which allow the generation of event time-stamps with a relative accuracy of $< 10$ ns rms error by autonomous systems using low-cost, off-the-shelf, Global Positioning Satellite (GPS) receiver modules is described. Performance over a baseline of $> 10$ km is demonstrated which is several times better than that required for the giant array application. To extract maximal information from a simple low cost particle detector the use of flash analogue to digital converters (FADCs) is highly advantageous. Investigation of these devices and the design and testing of a 100 mega sample per second (MSPS) transient capture system is described in Chapter 3.

The selection and optimization of a suitable particle detector unit requires anticipation of the characteristics of the ground level shower front. In Chapter 4 investigations of the relevant predictions of the MOCCA shower simulation code are presented. Water Čerenkov detectors are believed to be the most cost effective technology for a next generation array. Detailed phenomenological analysis of the behaviour of a possible detector unit is presented in Chapter 5, together with some test data from a prototype. Procedures which allow the simulation of a complete array of such units on an event-by-event basis have been developed, and are described in the final chapter. Verification of the realism of the simulation procedures is accomplished by careful cross-checking against results from the Haverah Park experiment.

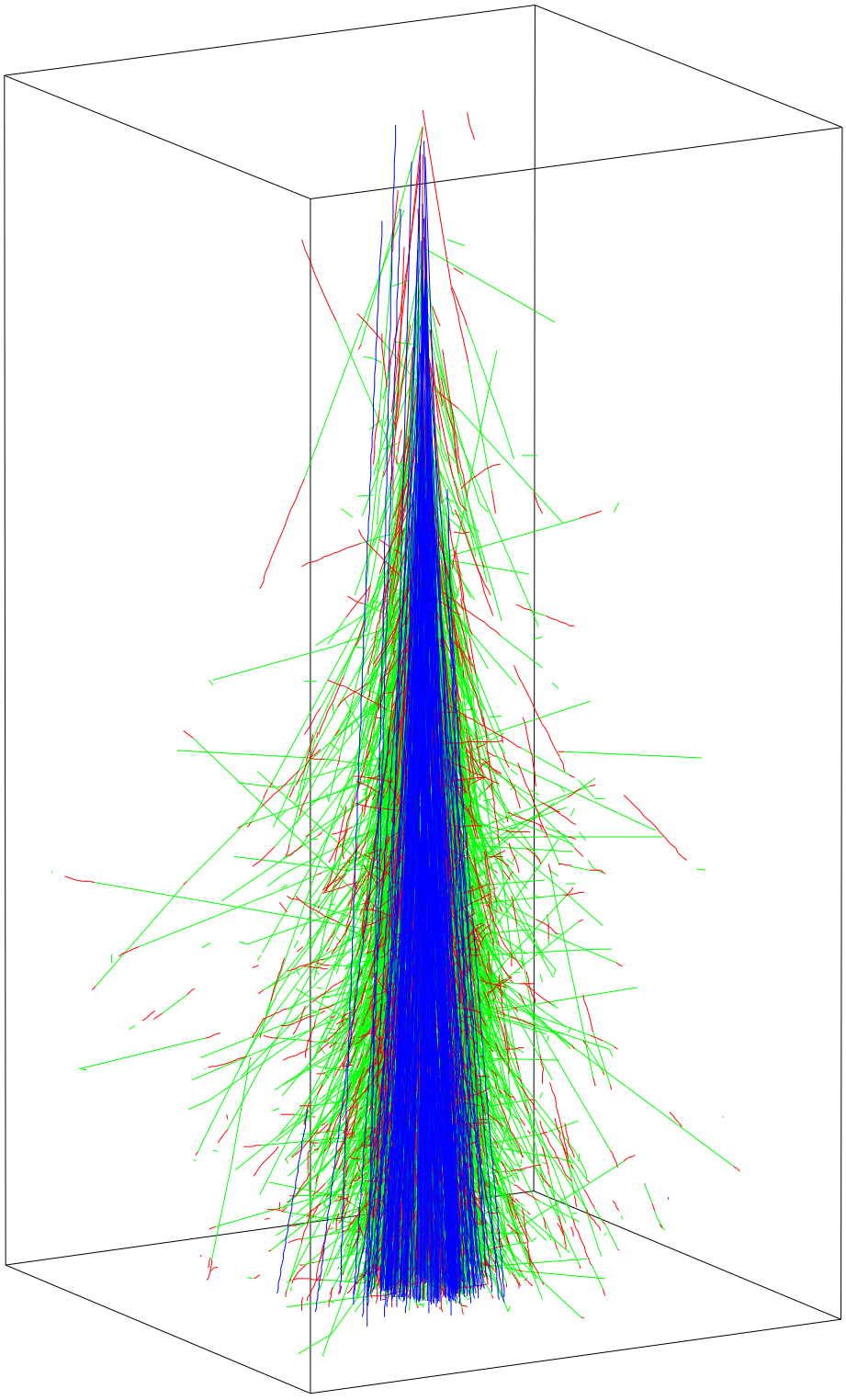

Figure 0.1: *3D projection of a simulated $10^{19}$ eV EAS. A sample of the particle tracks beyond 300 m from the shower axis are shown. The frame box is $6 \times 6 \times 12$ km high, and the colour code is $\gamma$ green, e red, and $\mu$ blue.*

# Contents

# List of Figures

LIST OF FIGURES

# List of Tables

# Key to Abbreviations

| | |
|---|---|
| ADC | Analogue to Digital Converter |
| CPU | Central Processing Unit |
| EAS | Extensive Air Shower |
| em | electromagnetic |
| FADC | Flash Analogue to Digital Converter |
| FWHM | Full Width at Half Maximum |
| GPS | Global Positioning Satellite |
| ldf | lateral distribution function |
| mfp | mean free path |
| MOCCA | MOnte Carlo CAscade |
| MSPS | Mega Samples Per Second |
| PMT | Photo Multiplier Tube |
| pps | pulse per second |
| PRN | Pseudo Random Number (code number of GPS satellites) |
| rms | root mean square |
| SA | Selective Availability |
| TRS | Time Recovery Satellite |
| UTC | Universal Time Coordinated |
| UHECR | Ultra High Energy Cosmic Ray (in this work $> 10^{19}$ eV) |
| VEM | Vertical Equivalent Muon |

# Acknowledgments

I would like to thank my supervisors Alan Watson and Jeremy Lloyd-Evans for good, always critical, advice on all I have done. During my first two years "down in the lab" in Leeds I was lucky to have the opportunity to work with Paul (Oggy) Ogden. Apart from driving him mad with constant questions and demands for components I learned a lot from him, both in terms of actual electronic design and technique, but equally important, the stoical attitude required when working with things which really should work but simply refuse to do so! I would also like to thank the powers that be for providing during that period what I hope is the coldest working environment that I will ever have to put up with.

Doing experimental work at Haverah Park with Simon Hart was enjoyable, and he also made a good flat-mate who seemed quite able to put up with my argumentative nature, despite his complaints.

I would like to thank James Cronin for inviting me to take part in the Giant Array Design Study Group, and finding money for me to stay for the full duration of the workshop. Despite working stupidly hard I enjoyed being at Fermilab, and met a lot of good people there — Ken Gibbs was largely responsible for keeping me sane, and I would like to thank Lucy Fortson for leaving it to the last minute (I think?).

Finally I am grateful to my parents for providing some financial support during the last three and a half years, and to my mother for proof reading the final draft manuscript.

# Chapter 1

## Introduction

### 1.1 Brief history of the extensive air shower field

From balloon flights made by Victor Hess as early as 1912 [1] it became clear that the ionization of the atmosphere increased very markedly with increasing altitude (after a small initial fall). This would not be expected if the origin was entirely from radioactive decay of material in the Earth's crust, as had previously been suggested; instead the inference was correctly drawn that there is a flux of highly penetrating radiation striking the Earth's atmosphere from above. The nature of this radiation remained unclear for many years, although it was shown by means of the "latitude" and "east-west" effects that the primary radiation included particles with energies as great as $10^{10}$ eV, and also that the majority were positively charged.

The phenomena now known as extensive air showers (EAS) were discovered by Auger and co-workers [2] in 1938 near Paris, and also working at mountain altitudes. Using two or three simple counters, operated in coincidence, and separated by a variable distance of up to 300 m, they demonstrated that there are large time and space correlated showers of particles impinging at ground level. Using simple and elegant arguments they were able to show that the energy spectrum of the primary particles initiating these showers extended to at least $10^{15}$ eV — a jump of 5 orders of magnitude over previous results.

Pioneering work by Bassi, Clark and Rossi [3] in 1953 at MIT demonstrated that an array of ground level detectors could reconstruct the incidence direction of an EAS by a simple relative timing technique. This led to the Agassiz experiment which ran from 1954–1957 and was probably the first system which may be called an EAS array. In the course of this work many techniques were developed which are still being actively used today (see Clark *et al.* [4] for details). As a follow up to the Agassiz system the first of the "giant" EAS arrays was constructed by Linsley and Scarsi at Volcano Ranch in New Mexico USA (8 km$^2$ area), commencing operation in 1959 [5]. In 1962 a shower was recorded using this detector with primary energy held to be $\approx 10^{20}$ eV [6] — an increase of 5 orders of magnitude over Auger's result.

Since that time progress has been relatively slow. A small number of additional giant air shower detectors were constructed during the 1960s and '70s, including the Haverah Park experiment in the UK [7, 8], the SUGAR system in Australia [9], and the Yakutsk array in the USSR [10]. These experiments made measurements of energy spectra and arrival direction distribution, and further events above $10^{20}$ eV were reported. A major step forward was made in the 1980s when the "Fly's Eye" remote sensing technique was introduced in which air showers are detected via the nitrogen fluorescence light which they produce in the atmosphere [11].

Recently there have been some exciting developments; on October 15 1991 an EAS was recorded by the Fly's Eye detector which was apparently initiated by a particle having energy of $3.2 \times 10^{20}$ eV [12]. The Fly's Eye technique is pseudo-calorimetric, and relies much less heavily on shower and detector modelling than conventional ground arrays. Hence the existence of events above $10^{20}$ eV — long a matter of vigorous debate — has become difficult to deny. The largest EAS detector constructed to date is the AGASA system in Japan, a conventional scintillator array having 100 km$^2$ area [13]. On December 3 1993 an event with inferred primary energy of $1.7$–$2.6 \times 10^{20}$ eV was recorded by this detector [14]. Some details of the current experimental situation are presented in section 1.3.

Constructing viable theories which allow the production of particles at these energies, and their propagation to Earth, is extremely problematic. In section 1.4 a brief review is presented.

It is clear that to settle some of the remaining questions in this field a next generation detector is called for. The required capabilities of such a system, and the currently proposed experimental solution, are discussed in section 1.5.

## 1.2 Anatomy of an extensive air shower

The accepted theory is that EAS are initiated by particles with very high kinetic energy colliding with air molecules in the upper atmosphere and initiating hadronic and electromagnetic cascades of secondary particles. Due to the steeply falling flux of incident particles with increasing energy, direct observation of the primaries is only possible up to $\sim 10^{14}$ eV by using high altitude balloon and satellite borne experiments. Above this limit information regarding the energy, arrival direction, and nature of the particles can only be deduced by observing the cascade secondaries. Hence a reasonably detailed understanding of shower development processes must be invoked.

Fortunately the rapid progress of particle physics over the last thirty years has provided excellent knowledge of fundamental particle interaction properties, and the energy frontier has been pushed remarkably high. The center of mass energy available at the first interaction of a $10^{20}$ eV cosmic ray is $\approx$ 400 TeV — only two orders of magnitude above the available energy of the world's most powerful $p\overline{p}$ collider to date, the Tevatron at Fermilab USA. However, it must be remembered that "standard" collider experiments are principally designed to probe rare interactions which result in products having large transverse momenta (high

$p_t$), and in any case do not yield direct information regarding proton-nucleus and nucleus-nucleus collisions. The advent of the next generation LHC experiment at CERN will be a big step forward, as this machine will be capable of colliding heavy ion beams at extremely high energies (Pb-Pb collisions will have a center of mass energy of $\approx 1$ PeV!).

The modern approach to the problem of EAS modelling, in common with many problems in high energy physics research, is the Monte Carlo technique. Computer code is written embodying the interaction mean-free-paths, branching ratios and energy transfer distributions of the fundamental cascade processes, together with a model of the atmosphere and the geomagnetic field. It is then, in principle, possible to simulate the development of individual showers, complete with all fluctuations. By running batches of showers the average characteristics under a variety of different assumptions may be predicted, and compared against experimental data. However, it is important to note that much progress was made in shower modelling without the use of powerful computers; see Rossi [15] for an excellent discussion of early analytic cascade theory.

A simple qualitative description of an ultra-high energy cascade is useful, and will be given here. When working with EAS it is convenient to consider position in the atmosphere in terms of g cm$^{-2}$ of overlying air mass. The relation between depth in g cm$^{-2}$ and altitude above sea level is approximately exponential with scale height $\approx 8$ km, but somewhat modified by the atmospheric temperature gradient. Sea level is at a depth of $\approx 1000$ g cm$^{-2}$. Cosmic rays enter the upper atmosphere and penetrate to some depth before interacting with an air molecule. The interaction cross section rises with energy, and also with the mass of the primary particle.

At each successive generation of the nucleonic shower approximately half of

the energy continues in nuclear particles, the bulk, on average, being carried by a single "leading-nucleon". The remainder of the incident energy produces pions, with roughly one sixth each going to $\pi^+$, $\pi^-$ and $\pi^0$. The charged pions of the initial generations have such high Lorentz factors that decay is effectively suppressed, and the bulk make nuclear collisions, and so give rise to a pionic cascade. However, the proper lifetime of the $\pi^0$ is so short that the great majority will decay to gamma rays before interacting, even at the highest energies ($\pi^0 \rightarrow \gamma + \gamma$). Thus at each generation of the pionic cascade one third of the available energy is lost to the electromagnetic cascade, and the remaining energy is distributed amongst a larger number of particles. Note that the nucleonic cascade continues to "feed" the pionic cascade deep into the shower development.

After some number of generations the individual charged pion energies have dropped sufficiently that they start to decay into muons before they can interact (e.g. $\pi^+ \rightarrow \mu^+ + \nu_\mu$). This takes place at approximately $E_\pi \leq 20$ GeV, and at this point the remaining pion energy is "dumped" into muons which undergo little further interaction, and mostly penetrate to ground level.

The number of pion generations required to degrade to the "decay energy" determines the fraction of the total shower energy which is transferred to the electromagnetic cascade. Hillas' simulations indicate [16] the following numbers; in a $10^{19}$ eV proton-initiated shower 2.4% of the primary energy goes into muons, 96% into the electromagnetic cascade, and the remainder into neutrinos and hadronic particles which survive to sea level. These should be compared to the equivalent numbers for a $10^{15}$ eV shower: 13% into muons, and 81% electromagnetic. If $f_\mu$ is the muonic energy fraction a full set of simulations demonstrate that $f_\mu \propto E_p^{-0.18}$, which can be qualitatively understood on the basis of the above cascade description.

Figure 1.1 is a schematic diagram showing the principal cascade processes in a

shower initiated by an incident cosmic ray nucleon. Not shown are the Čerenkov (forward beamed) and fluorescence (isotropic) photons, given off principally by the electromagnetic cascade, and which reach ground level in large numbers over a wide area. Note that the figure, and the above description, neglects many cross-over pathways between the three principal sub-cascades identified, and are highly simplified. For example the process of photo-pion production provides a mechanism for the electromagnetic shower to feed back into the pionic cascade.

The interaction of a nuclear primary is more complex with a random degree of fragmentation taking place at each step of the nucleonic cascade. As a consequence the incident energy is more rapidly degraded into multiple product particles, and for a nucleus of atomic mass $A$ the hadronic cascade is, to a first approximation, equivalent to the superposition of $A$ nucleon showers each of energy $E/A$.

## 1.3 Status of techniques and measurements in the highest energy regime

The observation of extreme ultra-large EAS ($> 10^{19}$ eV) is a research field which is now more than 30 years old. Due to the extremely low flux of such events, and hence the need for enormous detector systems, progress has been somewhat slow. However, thanks to persistent efforts on the part of the scientists involved we now have a good body of experimental data, and powerful techniques.

### 1.3.1 Giant detectors and giant showers, 1959–1995

The previous and current giant air shower detectors have already been mentioned. In this section some technical information regarding these systems is given, together with illustrations of selected ultra-high energy events.

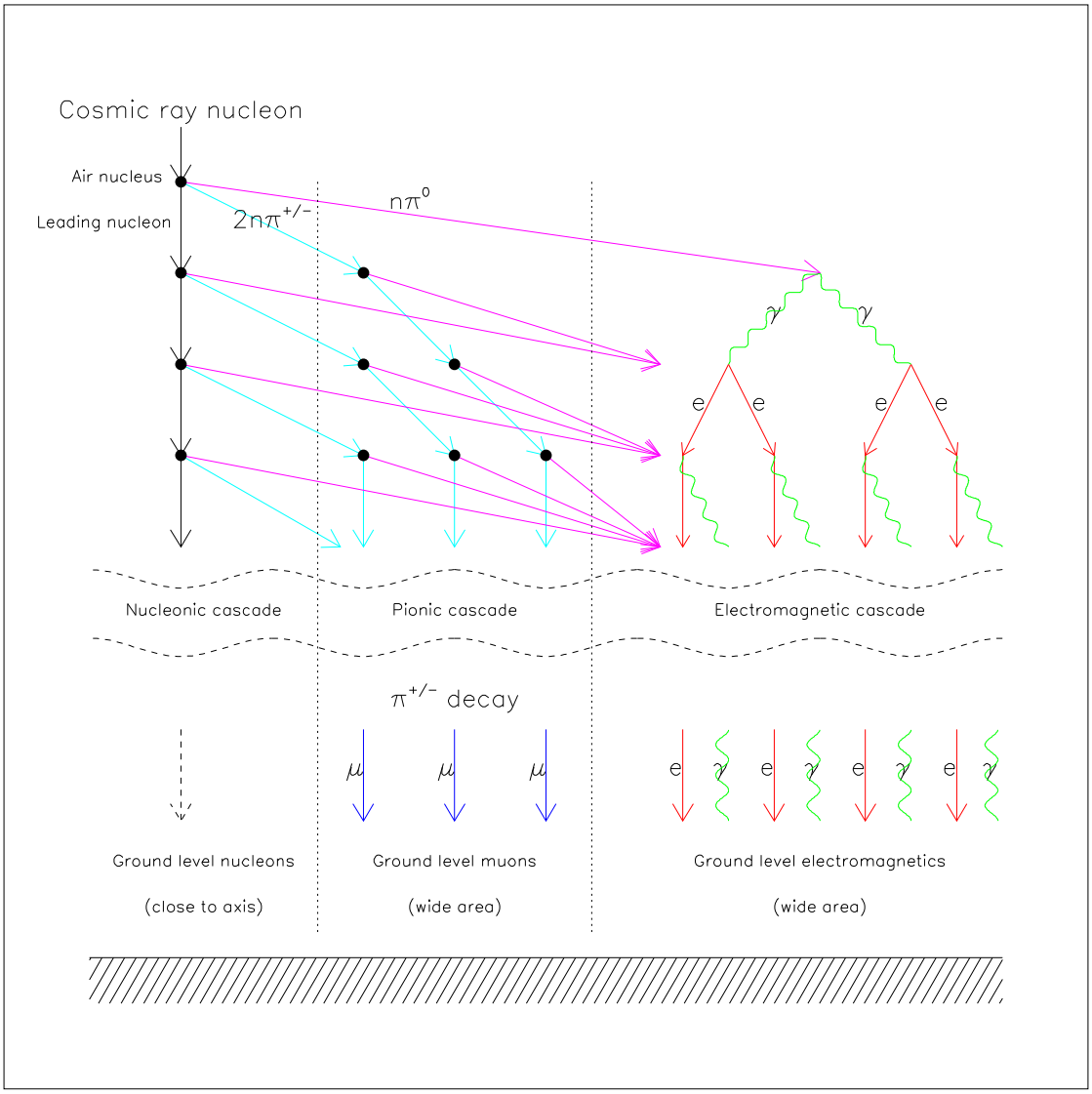


Figure 1.1: *Schematic diagram showing the principal EAS cascade processes. An incident cosmic ray nucleon is assumed, and the resulting shower divided into three categories; the nucleonic cascade consisting of the surviving primary itself in the guise of a "leading-nucleon", the pionic cascade, and the electromagnetic cascade which is fed by neutral pion decay. This picture is, of course, highly simplified.*

The Volcano Ranch array was a system of $19 \times 3.3$ m$^2 \times 9$ cm thick scintillator detectors arranged in a hexagonal grid with spacing of 885 m between units [17]. Each detector was linked to a central location by high bandwidth cable, and recording was by means of oscilloscope photography. This instrument was the first to observe a cosmic ray event apparently initiated by a primary particle with energy $\geq 10^{20}$ eV; the event is shown in the upper part of figure 1.2.

The Haverah Park array reached peak development in the late 1970s when, in addition to the $225 \times 2.25$ m$^2 \times 1.2$ m deep water Čerenkov detectors of the main array (deployed in clusters of up to 34 m$^2$), a system of $30 \times 1$ m$^2$ units was operated in a central area [18]. Although primarily intended to study EAS of lower energies a small number of ultra-large showers were recorded by this system in conjunction with the main array. A single such event having energy of $1 \times 10^{20}$ eV is illustrated in figure 1.3. This is probably the best measured EAS event at $\geq 10^{20}$ eV ever recorded by a ground array system.

The Akeno Giant Air Shower Array (AGASA) commenced operation in 1991, and with 100 km$^2$ collecting area, is the largest ground array yet constructed [13]. It is a system of $111 \times 2.2$ m$^2 \times 5$ cm thick scintillator detectors arranged in a non-uniform grid with characteristic spacing of $\approx 1$ km. The lower part of figure 1.2 shows the highest energy AGASA event to date, this also being the largest ever recorded by a ground array.

The Volcano Ranch, Haverah Park, and Yakutsk arrays all relied on high bandwidth cables to bring the detector signals to a central location for trigger formation, although some of the outer Haverah Park detectors were slaved to the central subarray using microwave links. The AGASA too relies on cable links, in this case serial optical fiber connections between strings of detector units. Of the previous ground array experiments SUGAR was unique in that none of the detectors sta-

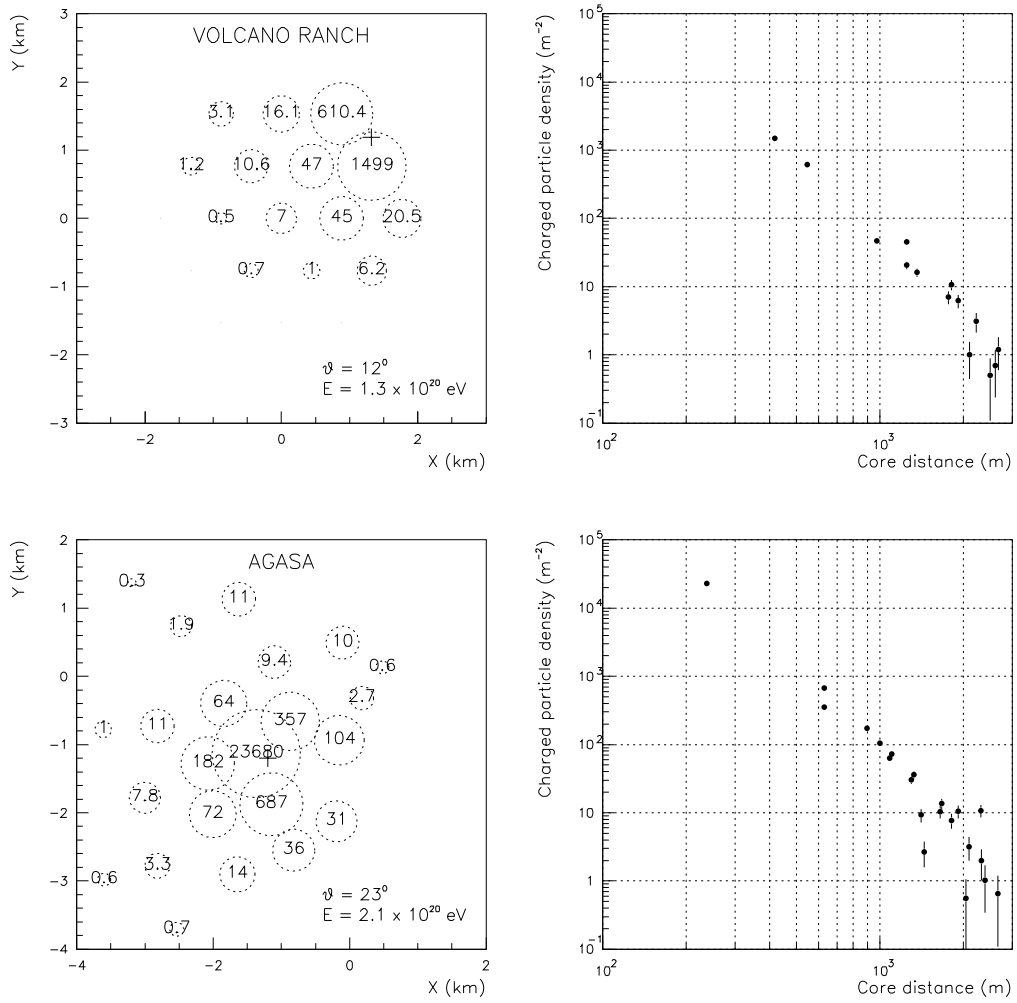


Figure 1.2: *Two ultra-large EAS events recorded using ground array systems. Each event is shown on the left as a detector map displaying recorded signal density, and on the right as a plot of signal density versus distance from the inferred core position. The radii of the circles in the left plots is proportional to the logarithm of the signal magnitude. The upper plots show the first event recorded for which an energy of* $\geq 10^{20}$ *eV was claimed, registered in 1961 by the Volcano Ranch system [6]. The lower plots show the currently largest ever ground array event, assigned an energy of* $2.1 \times 10^{20}$ *eV, and recorded in 1993 by the AGASA system [14].*

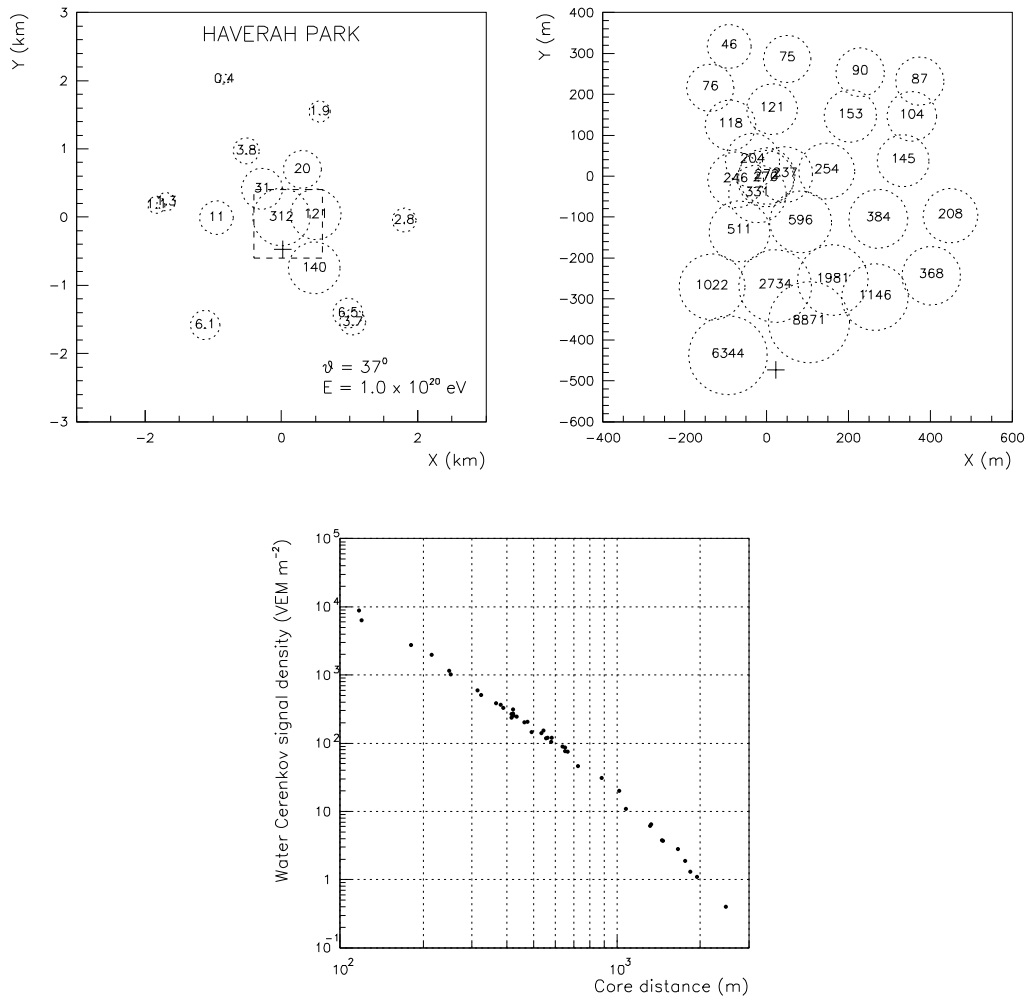


Figure 1.3: *An exquisitely well measured ultra-large EAS event recorded by the Haverah Park system [17]. This event fell close to an "infilled" array of smaller high dynamic range detectors, and hence was measured in very great detail. Assigned event energy was* $1 \times 10^{20}$ *eV. The commonly assumed EAS property of axial symmetry is dramatically demonstrated, since there are a large number of redundant observations each having very high statistical weight.*

tions were cable linked [9]. Each SUGAR unit operated autonomously, triggering on local coincidence between two buried 6 $m^2$ liquid scintillator detectors, and recording data from which EAS events were extracted by off-line cross matching of event time-stamps. The required time synchronization was achieved by means of a dedicated radio broadcast system. Unfortunately, SUGAR was ahead of its time in relation to the technology then available, and was dogged by reliability problems.

A completely different approach to EAS detection, suggested by Greisen [19], and also by Suga and Chudakov, has been aggressively developed at the University of Utah USA, leading to the advent of the Fly's Eye detector in the mid 1980s [11]. This technique exploits the isotropic fluorescence light given off when nitrogen molecules ionized by the passage of an EAS de-excite to make a remote calorimetric measurement of the longitudinal shower profile. Two systems of light collection mirrors and photomultipliers were constructed, viewing the night sky in a pixelated manner. A sub-set of EAS events triggered both systems allowing stereoscopic reconstruction of the shower track, and hence a very good understanding of the random errors in energy assignment when using a single detector. Figure 1.4 illustrates the largest event recorded by the Fly's Eye experiment, this also being the highest energy EAS ever observed by any system. Although this experiment is no longer running the same group are currently constructing a massively upgraded system known as Hi-Res [20], a portion of which is already operating.

### 1.3.2 Energy spectrum

Careful experiments by the Japanese Akeno collaboration using a series of ground arrays with increasing detector spacings have provided an excellent, cross calibrated, and hence self-consistent measurement of the cosmic ray energy spectrum from $10^{14.5}$–$10^{19.5}$ eV [21, 22, 23]. The complete differential numerical flux spec-

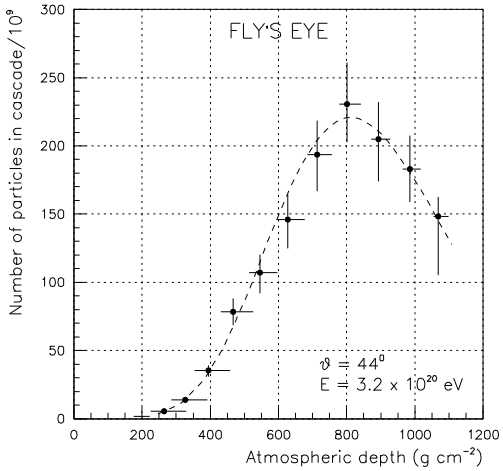


Figure 1.4: *The current largest ever EAS event recorded by the Fly's Eye experiment in 1991 [12]. The Fly's Eye is an optical detector which measures nitrogen fluorescence light produced by the electromagnetic EAS cascade. It thus observes the longitudinal shower profile in a pseudo-calorimetric manner. In this event the rise and fall of the cascade curve is clearly seen, leading to good accuracy in the energy assignment procedure. The calculated energy of this event is* $3.2 \times 10^{20}$ *eV; note that the peak of the cascade curve corresponds to* $>$ *200 billion particles.*

trum is shown in figure 1.5, in both the simple form $J(E)$, and modified form $J(E) \times E^3$. To a first approximation the spectrum over this 5 decade range is a featureless power-law with slope index $\gamma \approx 3$ ($J(E) \propto E^{-\gamma}$). Hence the modified form $J(E) \times E^3$ accentuates the spectral features; there are a number of apparently rather sharp transitions in the slope. Below the "knee" at $10^{15.7}$ eV $\gamma = 2.62 \pm 0.12$, and from $10^{15.7}$–$10^{17.8}$ eV $\gamma = 3.02 \pm 0.03$. Above $10^{17.8}$ eV there is a steepening to $\gamma = 3.16 \pm 0.08$, until the "ankle" which occurs in the region $10^{18.8}$–$10^{19.0}$ eV. Due to the currently limited statistics the slope in the highest energy region is somewhat dependent on the ankle energy selected; if $E_{ankle} = 10^{18.8}$ eV $\gamma = 2.7^{+0.2}_{-0.4}$, while for $E_{ankle} = 10^{19.0}$ eV $\gamma = 2.3^{+0.5}_{-0.3}$. This last result of the Akeno experiments may be compared to the Haverah Park result $\gamma = 2.7 \pm 0.2$ based on $E_{ankle} = 10^{19.0}$ eV [24].

Since the assignment of event energy by ground array experiments is a some-

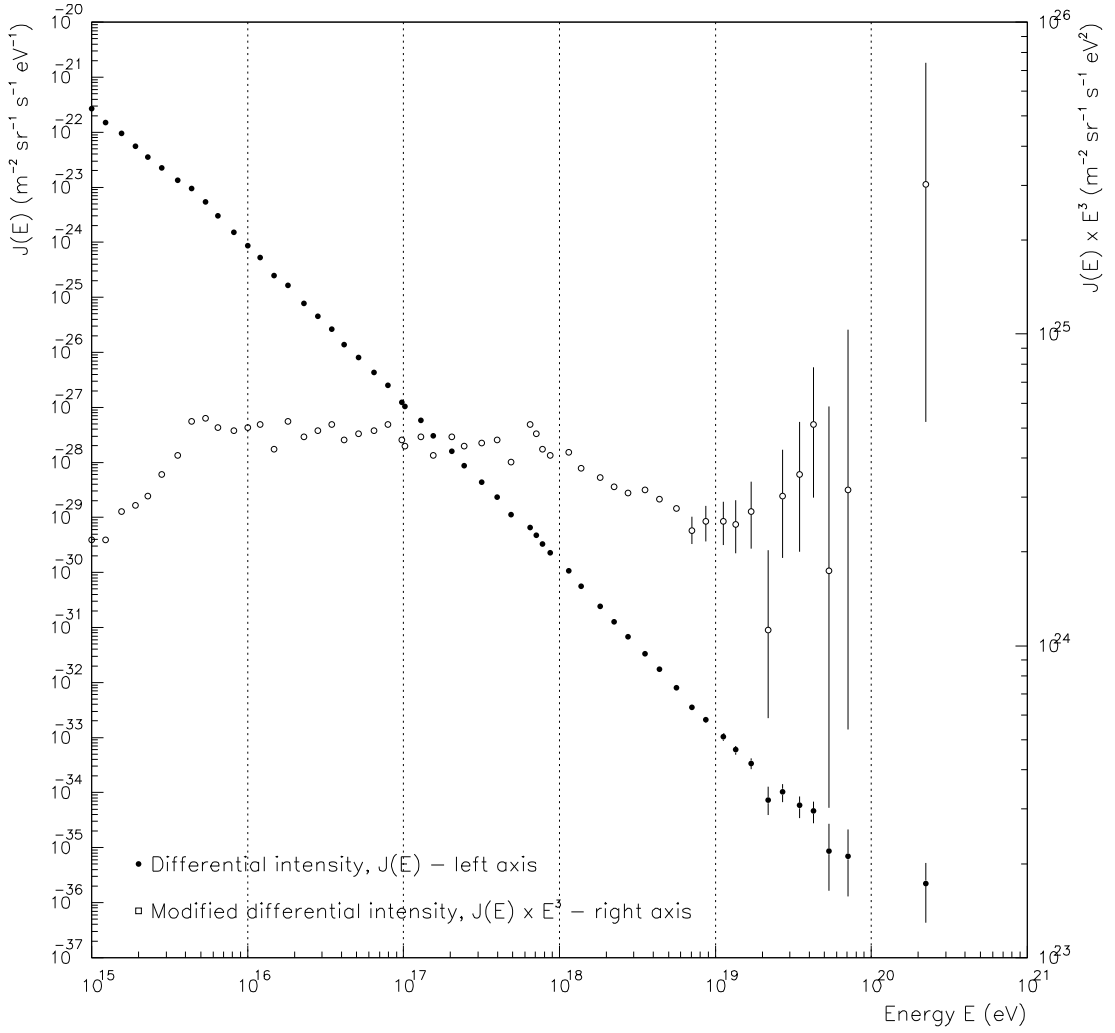


Figure 1.5: *The differential energy spectrum of primary cosmic rays from $10^{15.5}$–$10^{19.5}$ eV, as measured using a series of ground arrays with increasing detector spacings at Akeno in Japan [23, digitized from figure 13]. The points at $E > 10^{18.75}$ eV are from the 100 km$^2$ AGASA system. The spectrum is plotted both in the simple form (filled circles — left axis), and as a modified spectrum multiplied by $E^3$ to accentuate the small changes in slope of the underlying power law (open circles — right axis). The change in slope clearly seen at $\approx 10^{15.5}$ eV is often called the "knee". Note also the increase, and subsequent decrease, in the slope at $\approx 10^{18}$ eV, and $\approx 10^{19}$ eV respectively. These may similarly be dubbed the "shin" and "ankle".*

what indirect process, and has been the subject of controversy, it is interesting to compare the full energy spectra of several of the experiments which have probed the highest energy regime. Such a comparison is shown in figure 1.6 for the Haverah Park, AGASA and Fly's Eye instruments. The published data from each of these experiments at present relates to comparable exposures at the highest energies[1]. Note that only a $\approx 15\%$ systematic reduction of the assigned event energy is required to bring the two ground array experiments into good agreement with the Fly's Eye results[2]. Also note that both AGASA and Fly's Eye have recorded events well above $10^{20}$ eV.

### 1.3.3 Primary mass composition

Due to the extremely low flux of high energy cosmic rays direct observation of the primary particles is impossible above $\sim 10^{14}$ eV. Current balloon data indicates that as the knee of the energy spectrum at $\approx 10^{15.5}$ eV is approached the composition is becoming increasingly dominated by heavy particles [27]. At $\approx 10^{14}$ eV total energy per particle the percentages of $p$, He, C-O, Ne-S, and $Z > 17$ are found to be $12 \pm 9$, $25 \pm 14$, $26 \pm 12$, $15 \pm 8$, and $21 \pm 10$.

There have been innumerable suggestions and attempts to infer information regarding the chemical composition at higher energies from features of the ground level EAS; these fall into two broad categories. The first involve measuring the shower muon content in conjunction with a second component, usually either the electron or the Čerenkov light flux [28]. Comparison with shower model calculations is then made directly to infer primary mass, normally only on a statistical basis. The second group of methods introduce a further level of indirection, and

[1]The Yakutsk experiment in the former Soviet Union also has a comparable exposure.

[2]The error bars of the two highest energy Fly's Eye points plotted have been modified from those published to take account of the non-Gaussian behaviour of very small event samples [25].

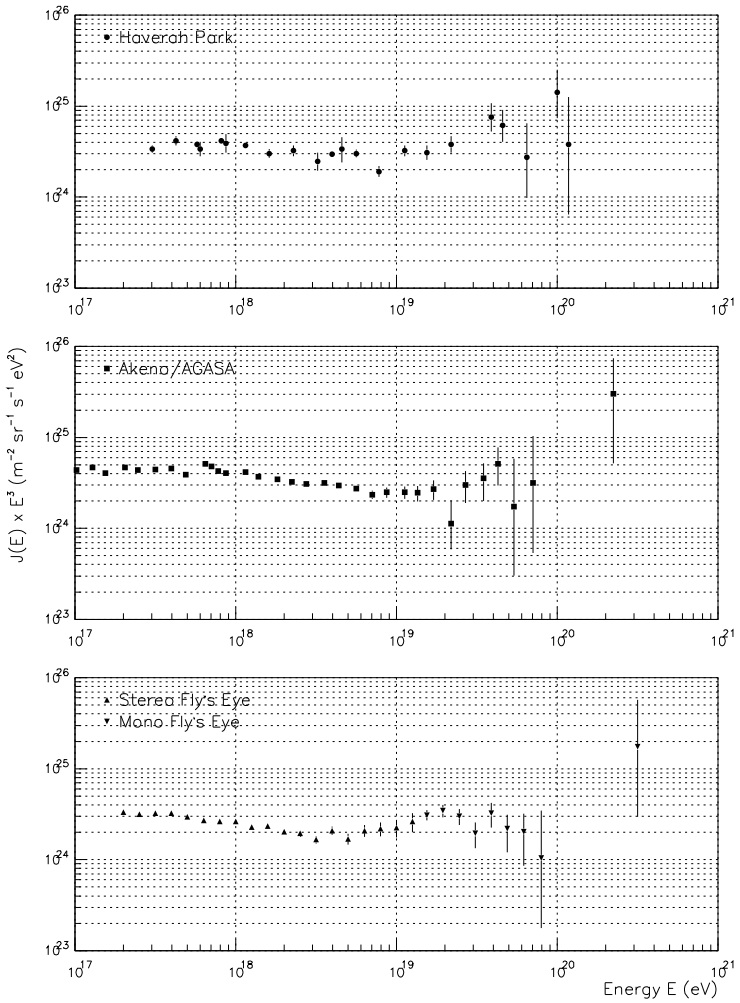


Figure 1.6: *Comparison of the differential energy spectra of primary cosmic rays above $10^{17}$ eV as observed by the Haverah Park, AGASA and Fly's Eye experiments. The upper plot shows the Haverah Park spectrum [24, table 2], and the center plot that from AGASA/Akeno [23, digitized from figure 13]. The lower plot displays the equivalent energy spectrum derived by the Fly's Eye collaboration. Below $10^{19.2}$ eV stereo data is used, since the experiment has much higher resolution in this mode [26, table 1]. Above that energy the stereo data yields insufficient statistics, and monocular data is plotted [26, digitized from figure 11]. The "dip and bump" structure is clearly seen by all three experiments.*

attempt to infer information regarding the depth of maximum shower development $X_{max}$ from a measurable ground level parameter, usually either the lateral or temporal spread of the ground level particles or the Čerenkov light flux [29, 30, 31, 32]. This depth of maximum information must then be translated into compositional information, again using models of shower development. For both groups of method the accuracy with which primary particle mass may be deduced is subject to severe constraints due to both shower-to-shower fluctuations, and uncertainties in interaction modelling at energies far above those comprehensively probed by accelerator experiments.

Of course combinations of two or more of the above techniques have been employed simultaneously, but it is important to realize that *no convincing absolute data on primary cosmic ray mass has ever been obtained using indirect methods.* However, the best work did confidently infer $\sigma(X_{max})$, the rms fluctuation in the depth of maximum shower development, and $d\overline{X}_{max}/d\log(E)$, the rate of increase of the mean depth of maximum with increasing shower energy. The quantity $d\overline{X}_{max}/d\log(E)$ is often called the elongation rate.

In addition to its powerful pseudo-calorimetric shower energy measurement capabilities the Fly's Eye technique has also represented a major step forward in the area of compositional sensitivity, $X_{max}$ being measured directly for each event (see figure 1.4). Encouragingly it turned out that the earlier indirect measurements of $\sigma(X_{max})$ and $d\overline{X}_{max}/d\log(E)$ were largely vindicated [33]. Figure 1.7 shows the results of the Fly's Eye studies of $X_{max}$. A very specific interpretation of this data has been offered [34] on the basis of comparisons with sophisticated Monte Carlo calculations of shower development, the results of which are also indicated in the figure. If we postulate that the shower simulations are essentially correct then we are seeing a composition which reaches a maximum mean mass at

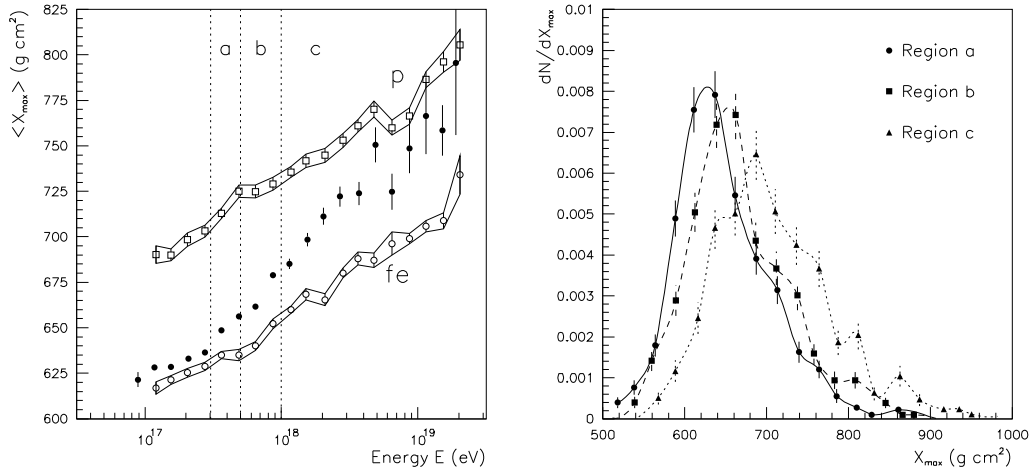


Figure 1.7: *Direct measurement of the depth of EAS maximum development by the Fly's Eye experiment. The left plot indicates the mean depth of maximum shower development* $\overline{X}_{max}$ *as a function of shower energy [26, digitized from figure 16], while the right plot shows the distribution of individual* $X_{max}$ *values within the energy intervals a,b and c identified [34, digitized from figure 7]. The left plot also shows the results of extensive Monte Carlo calculations, the two bands showing the predicted values of* $\overline{X}_{max}$ *for showers initiated by proton and iron primaries.*

about $10^{17.5}$ eV and then becomes progressively lighter at higher energies[3] There is additional support for this thesis from the shape of the $X_{max}$ distributions in the three energy intervals indicated; note that $\sigma(X_{max})$ is growing with energy — this is consistent with an increasingly large proportion of lighter primaries at higher energies.

The Fly's Eye collaboration have gone further and proposed a correlation between the structure of the energy spectrum (see figure 1.6), and the perceived changes in mass composition [35]. As will be discussed in section 1.4, the origin of cosmic rays even at lower energies ($> 10^{15}$ eV) is far from established. Hence we must be careful not to draw inferences from the rather scant data at higher energies

[3]The elongation rate which the MOCCA program predicts for a given primary type is much closer to the measured value of $74 \pm 4$ g cm$^{-2}$ per decade, and hence would suggest that the Fly's Eye data is consistent with a compositional mix which does not vary rapidly with energy.

which may be motivated more by what we expect to see based on canonical, but unproven, astrophysical theories, than experimental fact.

### 1.3.4 Arrival direction

The arrival direction of the highest energy cosmic rays shows no obvious structure or anisotropy. However, further investigation is currently severely constrained by the very limited number of events yet recorded. Figure 1.8 shows events from Volcano Ranch and Haverah Park plotted on the four octants of the celestial sphere which make up the northern hemisphere. For simple astrophysical reasons it is very difficult to understand why clustering of events does not occur at energies $\geq 10^{19}$ eV; this will be discussed below. Recently it has been claimed that the available data above $2 \times 10^{19}$ eV shows a statistically significant correlation with the supergalactic plane [36].

## 1.4 Astrophysical problems presented by the highest energy cosmic rays

It is rather difficult to identify potential sources for the highest energy cosmic rays based on current physical knowledge, and in the light of two simple and powerful constraints which candidate objects must satisfy. Theories can be split into two broad categories; top-down and bottom-up scenarios. In top-down theories ultra-high energy particles are produced directly by the release of energy which has been preserved in compact, meta-stable objects since the early universe when, according to standard cosmogenic theories, the prevailing energy density was extremely high. Such theoretical constructs are classed as topological defects, and include magnetic monopoles, cosmic strings etc. [37]. Bottom-up scenarios can be split into two sub-categories; iterative/gradual acceleration, and single-shot processes.

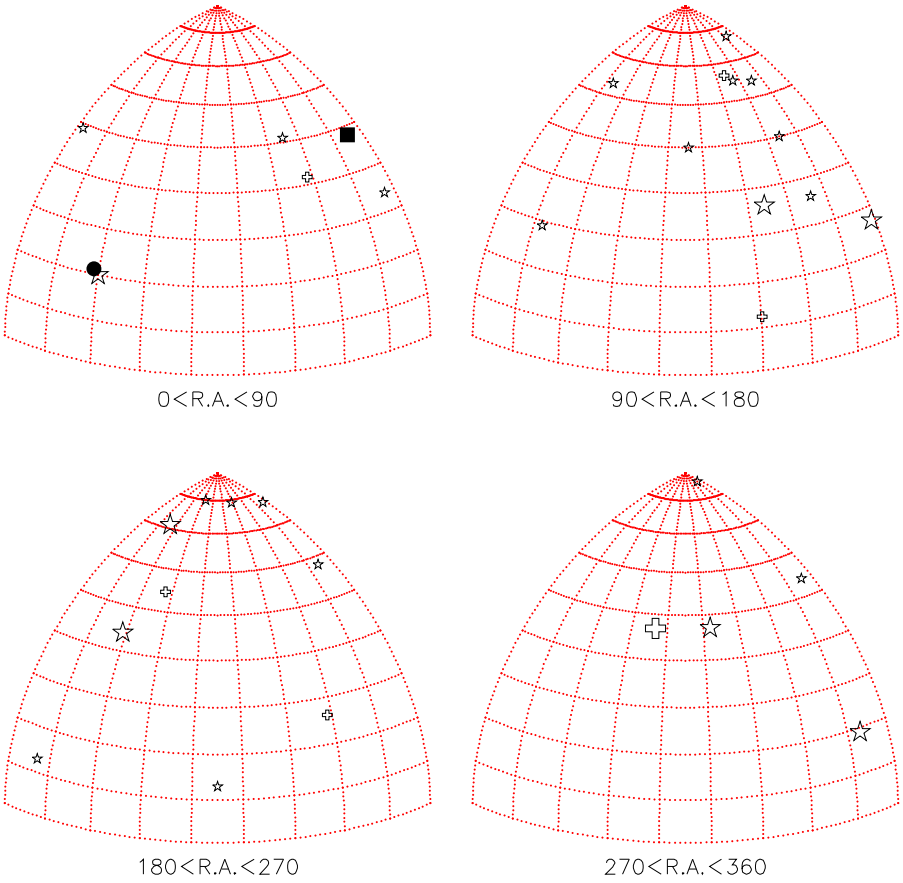


Figure 1.8: *Arrival directions of the highest energy cosmic rays plotted on the northern celestial hemisphere. The large crosses and stars are events detected by the Volcano Ranch and Haverah Park arrays respectively, and satisfy the cuts zenith angle $\theta > 45°$, and $E > 10^{20}$ eV. (The smaller symbols are similar but energy cut is $E > 4 \times 10^{19}$ eV.) The solid circle and square are the AGASA $2.1 \times 10^{20}$ eV and Fly's Eye $3.2 \times 10^{20}$ eV events.*

Cosmic rays below the spectral knee are widely believed to be accelerated from normal inter stellar matter (ISM) by the shock fronts which surround expanding supernova ejecta shells [38]. The theory of iterative acceleration through encounters with regions of moving magnetic field is due originally to Fermi [39]. Modern variants involve the multiple scattering of particles across a supersonic shock front by centers of magnetic turbulence, both up and down stream of the shock. Such a process, where at each iteration particles gain energy proportional to their energy and a fixed fraction escape, results naturally in a power law spectrum with $\gamma$ somewhat greater than 2 (as is observed). The proposition that supernova remnants (SNRs) are the source of cosmic rays below the knee has been widely accepted for many years, although only recently has direct evidence been obtained for the existence of very high energy particles in these objects [40]. This work is based on X-ray spectroscopy of SN1006, combining both high spatial and energy resolution, and yielding extremely convincing evidence for the presence of 100 TeV electrons. Such acceleration conditions can confidently be expected to produce protons and ions of as great, or greater energy.

It is also generally agreed that due to the limited time duration of supernova shocks ($\sim 10^4$ years), and hence the limited time available for acceleration, the energy spectrum of their product particles will start to cut off at $\sim 10^{14}$–$10^{15}$ eV. This corresponds rather nicely with the observed spectral knee, although the apparent sharpness of the knee is perhaps a little puzzling; we might expect SNR to have a wide range of characteristic lifetimes, and corresponding maximum acceleration energies[4]. The magnetic trapping condition discussed below will also result in gradual spectral cut off of SNR, due to the limited field strength of the scattering centers (protons will turn down before heavier nuclei). The origin of the

[4]This statement refers to the Akeno energy spectrum results which are displayed in figure 1.6. However, the latest results from the high altitude Tibet array show a more gradual change in the spectral index across the knee [41].

cosmic rays above the knee is something of a mystery. A possibility is secondary re-acceleration of the high end of the SNR energy spectrum in weaker, but much larger scale, shocks which may permeate galactic space [42] — this might explain the increase in spectral slope above the knee, and in any case if the particles had an entirely different source it is difficult to accept that the match in flux intensity across the knee occurs by chance.

A re-acceleration scenario requires that the cosmic rays above the knee be trapped within the galaxy by disordered magnetic fields for a sufficient period of time for the energy gain to take place, and leads to a more general requirement which any proposed site of gradual or iterative acceleration must satisfy. The Larmor radius of an ultra-relativistic particle is,

$$r_L = 1.08 \frac{E_{15}}{Z B_{\mu G}},$$

where $r_L$ is the gyro-radius in parsecs, the particle has charge $Ze$ and energy $E_{15}$ in units of $10^{15}$ eV, and the magnetic field strength $B_{\mu G}$ is in units of microgauss. Hence the characteristic size of an iterative or gradual accelerating region must be much greater than $2r_L$. Unless current measurements and models of the galactic magnetic field strengths (few $\mu$G) are profoundly wrong it seems impossible that above $\sim 10^{18}$ eV we are seeing re-accelerated SNR produced particles, and above $\sim 10^{19}$ eV it becomes difficult to contend that their origin is in our galaxy at all, given the experimental fact that some particles are observed to arrive from high galactic latitudes. It is hence commonly accepted that ultra-high energy cosmic rays (UHECRs) must have an extragalactic origin, and the observed changes in spectral slope at $\approx 10^{18}$ eV and $\approx 10^{19}$ eV are sometimes held to be clues as to a change-over in origin in this energy range [42, 35].

Figure 1.9 shows some possible acceleration sites for UHECRs on the basis of

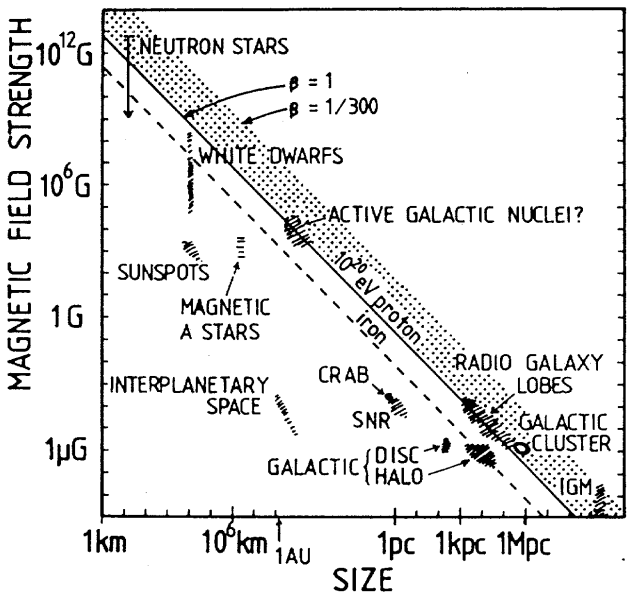


Figure 1.9: *Potential acceleration sites of the highest energy cosmic rays. Objects below the solid diagonal line cannot accelerate protons beyond $10^{20}$ eV even for scattering center velocity c; the dashed line indicates a similar limit for iron nuclei. For more realistic values of $\beta$ the proton limit will lie somewhere in the shaded band. Reproduced from [43].*

the magnetic containment constraint. Note that even if the velocity of the scattering centers is highly relativistic ($\beta \approx 1$) many objects are immediately ruled out. Apparently the size×magnetic field strength requirement would also apply to single-shot acceleration mechanisms [43] where an ultra-strong potential gradient might be directly available for particle acceleration, for instance in the magnetosphere of a rotating super-massive black hole [44]. It cannot be emphasized too strongly that the mere existence of such particles (an experimental fact!) is extremely puzzling on the basis of the required acceleration conditions alone. The situation is compounded, however, by the difficulty of getting UHECRs from extragalactic sites of production to the Earth.

In 1966 it was pointed out by Greisen [45], and independently by Zatsepin

and Kuzmin, that interactions with the then newly discovered cosmic microwave background radiation (CMBR) would render the universe increasingly opaque to cosmic ray protons at energies approaching $10^{20}$ eV. (In the rest frame of such a proton low energy photons appear to be hard gamma rays.) Photo-pion production interactions with the high energy tail of the 2.7 K black body spectrum will result in energy loss for protons at energies $\geq 5 \times 10^{19}$ eV (e.g. $p + \gamma_{2.7K} \rightarrow n + \pi^+$), and the loss will become intense above $10^{20}$ eV. There is an additional small effect at lower energies due to photo-pion interactions with IR photons[5], and due to pair production interactions ($p + \gamma_{2.7K} \rightarrow p + e^+ + e^-$). Figure 1.10 shows calculations by Cronin [46] of the mean residual particle energy as a function of distance assuming initially mono-energetic proton beams of $10^{20}$ eV, $10^{21}$ eV, and $10^{22}$ eV. Heavy nuclei will start to interact with the CMBR at approximately the same total energy per particle by the processes of photo-disintergration, and also through the giant dipole resonance, and the rate of energy degradation will be even more rapid. These predictions are based on very well understood physics, and represent a second powerful constraint on the potential sources of the highest energy cosmic rays.

If the sources of UHECRs are extragalactic and uniformly distributed throughout the universe then the flux at Earth would be dominated by those sources at cosmological distances. We would thus expect to see a turn-down and subsequent cutoff of the energy spectrum between $5 \times 10^{19}$ eV and $1 \times 10^{20}$ eV — an anticipated effect often referred to as the GZK cutoff. Due to this firm theoretical prediction the experimental data displayed in figure 1.6 has been the source of much controversy; the Fly's Eye spectrum suggests that a cutoff is indeed observed, whilst the Haverah Park spectrum shows no such feature, and the AGASA result lies somewhere in between. However, due to the current limited statistics the question

[5]This effect also places an additional constraint on compact source candidates such as active galactic nuclei (AGNs); the ambient optical and IR photon densities should not be so strong as to preclude the presence of UHE particles in the acceleration region.

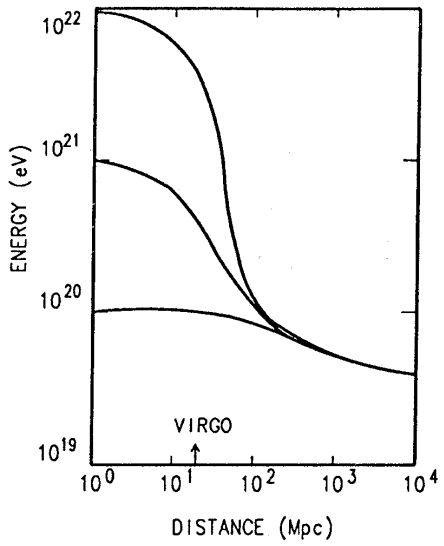


Figure 1.10: *Energy degradation of ultra-high energy protons via interactions with the cosmic microwave background radiation. The mean proton energy is shown as a function of distance assuming initially mono-energetic proton beams of $10^{20}$ eV, $10^{21}$ eV, and $10^{22}$ eV. Reproduced from [46].*

remains unsettled. Additionally, the situation has been greatly modified in the last few years by the observation of "super-GZK" events by the Fly's Eye and AGASA systems (as displayed in figures 1.2 and 1.4). This has led to the proposal that there is a "gap" in the spectrum between the expected cutoff of particles from extragalactic sources, at $\approx 5 \times 10^{19}$ eV, and the emergence of a new source which, due to a "super-hard" injection spectrum, (and presumably relative proximity to the earth), becomes apparent at $> 10^{20}$ eV [47]. The present author finds such theories, whilst interesting, somewhat far-fetched given the current experimental information, and resting, as they do, on an implicit acceptance of such things as the Fly's Eye Monte Carlo based compositional information.

By reference to figure 1.10 we can see that it is highly unlikely that super-GZK particles have their origin more than 100 Mpc from the Earth. Most of the even

faintly plausible acceleration sites, for instance very powerful radio galaxies, are at distances much greater than this. Additionally, based on current knowledge of the strength of large scale ordered magnetic fields in the galactic disc and halo, and the rather sketchy estimates of the fields in extra-galactic space, such particles should not be deflected by more than a few degrees from the directions of their sources. However, no obvious correlation with known astrophysical objects is found [48].

In summary UHECRs *must* have their origin at distances of $< 100$ Mpc, and their arrival directions *should* be close to the directions of the sources. It is extremely difficult to construct viable theories of acceleration based on the known characteristics of objects within this volume of space, or in fact anywhere in the universe. However, the current investigation of these question is presently severely hampered by the limited experimental data available.

## 1.5 Towards a next generation experiment

The origin and nature of cosmic rays remains a major unsettled question in high energy astrophysics, particularly above the maximum tenable SNR acceleration energy of $\sim 10^{15}$ eV. To gain insights above this energy it is natural to turn to the highest energy particles since these must have their source(s) relatively close by in the universe and should travel largely undeflected to the earth. Even if the particles above $10^{19}$ eV do not share a common origin with those below, they nevertheless represent a fascinating phenomenon which may well impact on our knowledge of fundamental physics and cosmology. The single greatest constraint on further progress in this field is the very low flux of the highest energy events — for events above $10^{20}$ eV the rate is approximately 1 km$^{-2}$ sr$^{-1}$ per century! The current AGASA system has an acceptance of the order of 100 km$^2$ sr, and the Hi-Res system shortly to become operational will have a similar time averaged

aperture at the highest energies. There is thus a clear need for a next generation experimental system to be designed and constructed which can improve upon this number by 1–2 orders of magnitude.

### 1.5.1 Detector requirements

The basic requirements which an experimental system must satisfy if it is to rapidly advance our knowledge of the highest energy regime may be summarized as follows:

- The ability to collect a statistically meaningful sample of UHE events at an acceptable rate. ($\sim$ 100 events per week with primary energy $> 10^{19}$ and $\sim$ 1 event per week with energy $> 10^{20}$ eV may be appropriate numbers.)
- The ability to reconstruct EAS events with reasonable, *and demonstrable*, accuracy. ($\approx 1.5^{\circ}$ rms space angle error in shower incidence direction assignment, and $\approx 30\%$ rms energy assignment error would seem acceptable.)
- The ability to search the entire celestial sphere for point sources, clustering, and/or large scale anisotropy in UHECR arrival directions. (Sky coverage should probably be sufficiently uniform that no region receives less than half of the mean all-sky exposure.)
- The ability to measure shower parameters which are expected to be sensitive to the nature of the primary particles. (As a minimum it should be possible to split the observed data set into heavy primary and light primary enriched subsets when working with the hypothesis that UHECRs are a mix of ordinary atomic nuclei.)

### 1.5.2 The proposed Auger experiment

Global interest in the construction of a next generation experiment has been growing in recent years; workshops were held in Paris, France (April 1992), Adelaide, Australia (January 1993), Tokyo, Japan (September 1993), and culminated in a six-month design study group which met at Fermilab, USA (February–July 1995). A design report document [49] has been produced, and the formation of a large international collaboration which will build and operate the instruments took place in Paris in November 1995.

The reference design calls for a hybrid system made up of a surface array operating in conjunction with a Fly's Eye style fluorescence detector. This will exploit the power of both available experimental techniques, the sum of the two being many times more effective than either alone. The great strength of a particle detector array is that it can operate 24 hours a day under any weather conditions; however, as discussed above, event energy assignment and compositional parameter interpretation are subject to model uncertainties. A fluorescence system, on the other hand, requires clear moon-less nights ($\approx 10\%$ on-time), but makes a pseudo-calorimetric measurement of shower energy, and can directly determine the depth of cascade maximum development for each event observed. The proposed experiment will effectively use the Fly's Eye type detector as a calibration tool for the surface system; coincident data will allow training, and fine tuning, of the ground array analysis procedures. Of course, in addition, the events observed by both systems will form a sub-set of extremely high quality data.

The design report document calls for two detectors systems each having an area of 3000 km$^2$ located in the northern and southern hemispheres. The surface arrays are to be 1650 water Čerenkov units, each 10 m$^2$ in area $\times$ 1.2 m deep, arranged in a hexagonal grid with a spacing of 1.5 km between stations. There

will be a single fluorescence detector located approximately in the center of each site. The ground array units will not be cable linked; instead they will communicate using digital radio techniques, and time synchronization between detector stations will be achieved by use of the Global Positioning Satellite (GPS) system. The data network topology has yet to be finalized; the competing options are for a "fraternal" system where on-line EAS event recognition takes place through each detector communicating with its nearest neighbors, and a "federal" system where trigger formation occurs at a central location. Power for each station will be provided by a battery backed system of solar cells.

The proposed experiment thus relies on several areas of new, and rapidly developing, technology, but all required elements already exist in the commercial sector. This thesis concentrates on three main areas of development work amongst those needed to make the Auger experiment a reality. In Chapter 2 the development of techniques which allow the generation of event time-stamps with a relative accuracy of $< 10$ ns rms error by autonomous systems using low-cost, off-the-shelf, GPS receiver modules is described. To extract maximal information from a simple particle detector the use of flash analogue to digital converters (FADCs) is highly advantageous. The author has investigated these devices and designed a 100 mega sample per second (MSPS) transient capture system; this work is described in Chapter 3.

The optimization of the Auger experimental design involves anticipation of the characteristics of ultra-large EAS, in conjunction with an understanding of the behaviour of practical particle detector systems. In Chapter 4 investigations of the relevant predictions of the MOCCA shower simulation code are presented. The author has carried out a detailed analysis of the response of the proposed water Čerenkov detector unit; this is discussed in Chapter 5. Finally, the simulated response of the complete ground array system is presented in Chapter 6, where the

predictions of the simulation procedures are also carefully checked against existing experimental data.

# Chapter 2

## GPS based event time-stamping

The proposal to build a next generation detector of the highest energy cosmic rays array described in section 1.5.2 is feasible, both in cost and logistical terms, only if physical point-to-point connections can be avoided. The ground array systems envisaged are large networks of semi-autonomous detector stations, spread over a wide area, using solar power, and linked only by radio communications.

Air shower arrays have traditionally relied upon detector relative timing to allow event incidence angle reconstruction. Additionally a key element of the autonomous detector concept is that on-line event recognition should also rely upon timing. Each detector unit will form low level triggers and assign these event time-stamps. The second level trigger will be formed by searching for time and space correlation of these event times.

One method of obtaining autonomous event time-stamp synchronization is through the exploitation of the Global Positioning Satellite (GPS) system. Currently available commercial GPS time-stamping systems typically deliver synchronization only at the level of microseconds, and cost upwards of $5000 per unit.

There are other more conventional multi-site experiments in astrophysics, and probably other subject areas, where highly correlated data acquisition at remote locations is required. Examples are the stereo Fly's Eye EAS detectors [11], Whipple

Čerenkov TeV gamma ray telescopes [50], and the SPASE/AMANDA coincidence experiment at the South Pole [51].

Two demonstration GPS based event time-stamping systems were developed and tested at Leeds by the author; this work is described in the sections which follow. Four similar systems have also been constructed and deployed at the South Pole for use in the SPASE/AMANDA coincidence experiment [51], where their performance and reliability has been good. Much of the following work is published elsewhere [52, 53].

## 2.1 The GPS system

The GPS system is a US Government Department of Defense network which disseminates precise time and position information continuously to suitably equipped users anywhere on or above the surface of the earth [54]. Unrestricted civilian access to the standard positioning service (SPS) is allowed subject to a deliberate performance degradation known as selective availability (SA). The system consists of a constellation of 24 satellites, which have orbital period of half the sidereal day, and are each uniquely identified by a pseudo random number (PRN) code. The satellite transmissions make use of spread spectrum techniques, and are thus highly immune to interference or jamming. A user must receive signals from at least four satellites to determine position, but if position is known, only a single satellite need be tracked to determine time. Access to UTC absolute time is available through the system with a precision of $\leq 1$ $\mu$s.

## 2.2 SA and scheduled common view

The SA degradation is implemented by applying slowly varying random offsets from true GPS system time to the apparent time as broadcast by each satellite. This effect is clearly shown in figure 2.1, where the time interval between the 1 pps (1 pulse per second) marks from a GPS receiver, and the 1 pps marks from a rubidium atomic time standard have been recorded over a 12 hour period. Every 2 hours the time recovery satellite (TRS) is changed, the satellite used during each block being indicated by the PRN code at the top of the figure.

The high stability of the Rb clock over periods of the order of hours allows the SA time frame "dither" to be seen. The maximum amplitude of the fluctuations is $\approx$ 300 ns, and the time period typically several hundred seconds. However, importantly, the maximum rate of change of the offset is $< 1$ ns $s^{-1}$. This means that all receivers using the same TRS will see the same offset from true GPS time over a very wide geographic area. (The discontinuities visible on satellite switching indicate that each satellite has a different random offset. The linear line sections during PRN 15 & 20 tracking periods indicate that SA was not applied to these satellites when this data was taken [55].)

Assuming that the average frequency of the GPS 1 pps marks tends to a perfect 1 Hz long term, the gradient of a line fit to the data shown in figure 2.1 represents the offset of the Rb clock from this value, and is $\sim$ 1 part in $10^{10}$. Making the same assumption, the line fit curvature indicates that the frequency of the Rb clock changes by $\sim$ 1 part in $10^{12}$ during the run. These figures are consistent with the performance that can be expected from a clock of this type.

To overcome SA in applications requiring only relative accuracy it is necessary that all GPS receivers are tracking the same satellite set at any given time. How-

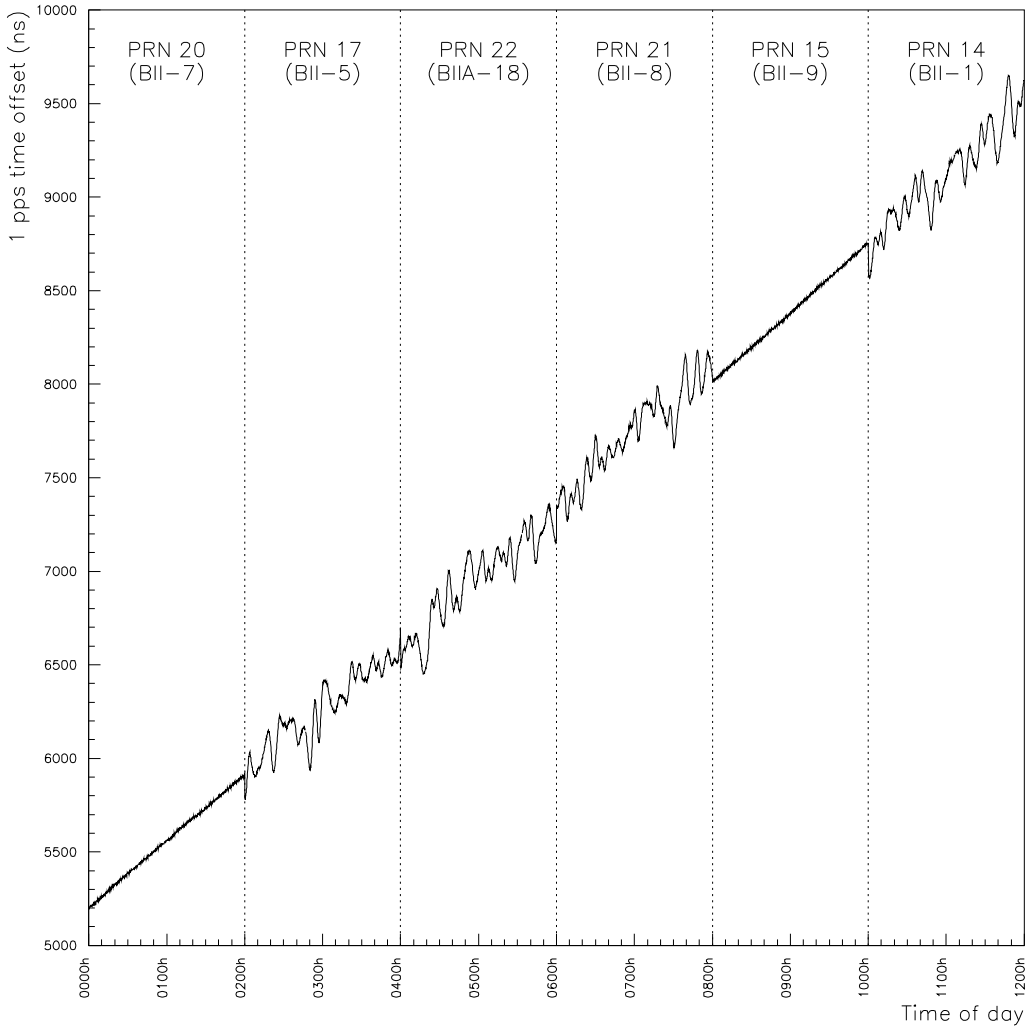


Figure 2.1: *GPS time from single satellites versus rubidium atomic clock time during the afternoon of 5/5/94. The PRN code of the GPS satellite being tracked during each 2 hour period is given at the top of the figure.*

ever, when time only is required, it is simpler, and more robust, to fix receiver position and solve for time from a single satellite. The antenna coordinates to be used can be surveyed by running all receivers in navigation mode for many hours, and taking the average position of each. It is clearly necessary that the relative precision of the coordinates used should be significantly better than the distance traveled at velocity $c$ in the time period to which synchronization is required.

To ensure that all receivers use the same TRS at given time a list of tracking periods with the associated satellite PRN can be drawn up in advance and distributed to each event time-stamping unit. This situation can then be referred to as a scheduled common view. Since the satellites have half sidereal period they rise and set four minutes earlier each solar day. Provided this effect is taken into account a schedule will remain valid for many months, since the orbits are maintained to high precision. However, the above assumes that the satellites will remain continuously operational; in practice test and maintenance outages do occur, both with and without prior warning. A practical experimental system would therefore need to make allowances for possible satellite failures, by having at least one level of backup schedule in place.

If SA error is eliminated by the above technique, the remaining possible error sources are threefold providing only relative accuracy is required. These are, mismatch of the ionospheric/tropospheric delay correction error, multipath propagation error, and receiver delay mismatch and noise. These effects are discussed by Lewandowski and Thomas [56]. Civilian GPS receivers use a mathematical model to correct for the propagation delay of the atmosphere. The accuracy of the model is limited, so a residual error remains, the magnitude of which may vary between different atmospheric paths. In the reference above it is stated that the mismatch of this error is $< 8$ ns over a 1000 km baseline provided the TRS elevation angle is $> 30°$. Multipath error effects may be minimized by good antenna selection

and location, whilst receiver noise and delay mismatch may be measured through co-located testing.

## 2.3 Description of the event time-stamp system

Each event time-stamping system consists of three main elements:

- A low cost commercial GPS receiver module with antenna.
- A circuit board carrying custom designed time-stamping electronics.
- A PC type computer for control and data acquisition purposes.

The structure of a single system is shown in figure 2.2. The GPS receiver module used is a Magnavox[1] GPS Engine$^{TM}$ (scientific model), which is a highly integrated 6 channel C/A code receiver, and has special time recovery modes [57]. One of these allows the user to lock position at given coordinates, and solve for time from a specified single satellite. A 1 pps output is provided which has a fast rising edge. Due to the internal clock rate of the receiver being 10 MHz, the 1 pps signal has an inherent jitter of $\pm 50$ ns. However, a data message is provided over the serial communications link giving the offset in ns of the last 1 pps mark from correct satellite time. Data is also provided over this link giving the date, time of day, and detailed status information. The GPS antenna used is a simple, low-cost, patch type device with an integral preamp.

The custom electronics consists of a 100 MHz, free-running, 28 bit counter, the value of which is read "on-the-fly" by two latches. Latch A is triggered by the arrival of 1 pps marks from the GPS receiver, and latch B by pulses indicating the

[1]The Magnavox GPS business has now been bought out by Leica Inc.

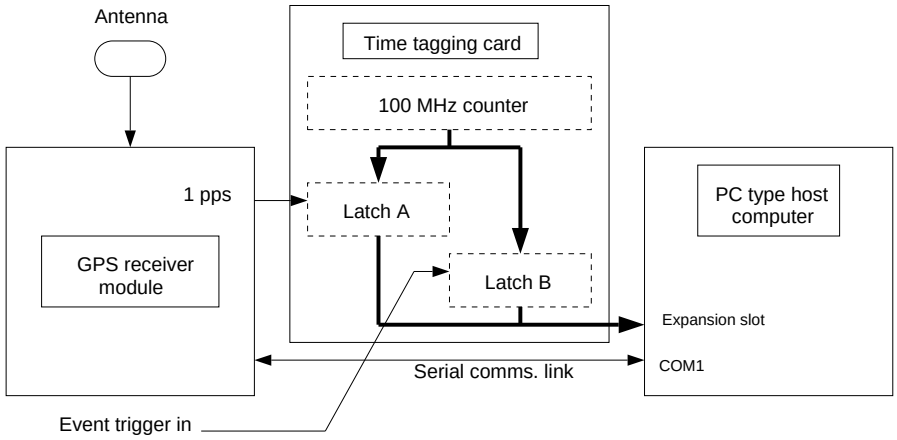


Figure 2.2: *Structure of the GPS based event time-stamping systems.*

events which are to be time-stamped. The data acquisition computer reads the latch values, and reconstructs the time of each event by simple linear interpolation between the 1 pps marks.

The interpolation is achieved using equation 2.1. $X_1$ is the count value at the beginning of a 1 second interval, $O_{X_1}$ being the corresponding offset in ns. Similarly the count value at end of the 1 second interval is $X_3$, with corresponding offset $O_{X_3}$. Count value at event time is $X_2$, and the time of day at beginning of the second is $T$ seconds.

$$Event\ Time = T + \frac{X_2 - (X_1 + O_{X_1})}{(X_3 + O_{X_3}) - (X_1 + O_{X_1})} \tag{2.1}$$

## 2.4 Testing of the event time-stamp system

To test an autonomous event time-stamping system it is necessary to have pairs of events occurring a known time interval apart across the required baseline. This

can be done by sending a test pulse between two locations using a link which has a measurable propagation delay. If the link has a stable, but unknown delay, random error of the time-stamping system may still be measured. Due to the variable geometry which occurs in the GPS system, it is difficult to envisage a source of systematic offset scaling with distance, which would not also vary with satellite motion. Hence it is very probably acceptable to use such a link for longer baseline testing. In the sections which follow testing of the time-stamping systems is described over several baselines.

### 2.4.1 Co-located and over a 500 m baseline using a high bandwidth cable link

Initial testing was conducted with the two systems co-located in the laboratory. Field tests were then carried out at the Haverah Park site using a 500 m run of high bandwidth cable (Aerialite). The test set-up is shown in figure 2.3. The event to be time-stamped was simply a pulse generator running at approximately 1.25 Hz, but asynchronously to the 1 pps marks, so that events fell in all parts of the second interval over time. Apart from this trigger input the two systems were fully independent, tracking satellites according to the schedule, reconstructing event times, and logging these to disk. At the end of a test run the event time lists were collected from each computer, matched up, and the event time from system #2 subtracted from that from system #1 to yield the apparent time interval.

For testing and presentation purposes a schedule was drawn up dividing the day into twelve two-hour blocks. In a practical system the schedule would consist of unequal track times, some of which could be up to 4 or 5 hours in duration depending on satellite availability. To ensure uninterrupted satellite tracking it is desirable that the TRS should always be at a fairly high elevation angle ($> 25°$).

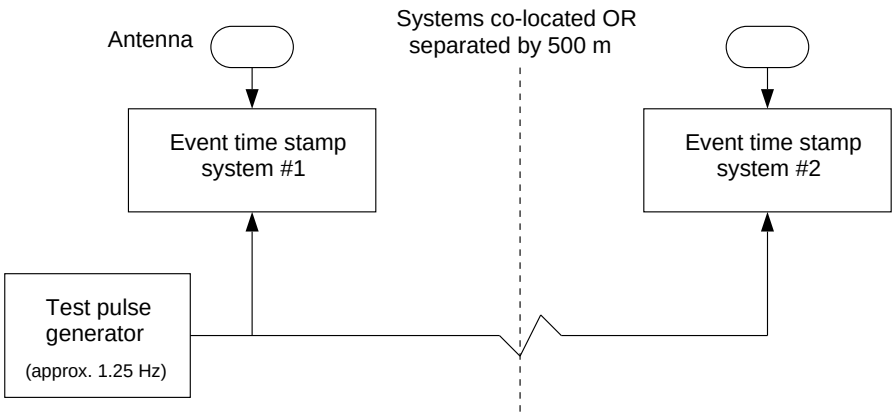


Figure 2.3: *Experimental set-up for co-located and 500 m baseline event time-stamping system tests.*

The results presented here were obtained after the systems had been evaluated and were well understood. However, they were fully repeatable.

To minimize systematic error it is clearly crucial that the GPS antenna cables, 1 pps mark cables, and test event injection cables are exactly the same lengths. More surprisingly, it was also found that performance is optimum when the antennae are aligned in the same horizontal plane, and with the same rotational orientation. This is presumably due to asymmetric antenna gain patterns, and hence a mismatch occurring in the received signal power from the TRS when misaligned. How a slight differential in the input level produces a relative 1 pps offset is not understood.

Initially high stability 100 MHz oven controlled crystal oscillators (OCXO) were used to drive the time-stamping counter, (the MilliRen Technology 245-0501). However, it was found that when employing simple linear interpolation across a single second using equation 2.1 equally good results could be obtained using a cheap non-ovened device, (the IQD IQXO-132B). Since proof of a low cost system was a major objective the less expensive oscillator was used for all the results detailed here.

Before time recovery runs commenced the relative positions of the antenna mounts at the locations used were first surveyed to sufficient accuracy. This was done by placing the engines in a low dynamics navigation mode, one at each location, and logging apparent position for a period of 24 hours. It was found that to measure the baseline with $\approx 1$ m repeatability it was necessary to subtract the averages from *concurrent* 24 hour data sets.

**Co-located results** Figure 2.4 shows the results from a typical 12 hour run with the event time-stamping systems co-located. Since the systems are triggered simultaneously any deviation from a time interval of zero represents the measurement error. It can be seen that the observed error has at least three components; a random jitter which varies on an event-by-event basis, a slower varying wander in the short term mean, and a seemingly fixed offset from zero. The wander effect has a wide range of characteristic periods, from 10 minutes to many hours. In the analysis presented here I have chosen to call the mean of each 12 hour data set the offset error, and the standard deviation the random error. This is a somewhat arbitrary decision since these two quantities are not independent. The slow varying wander will lead to a smearing of the short term distribution and an increased value for the standard deviation.

In figure 2.4 it can be seen that excursions of the error value occur on the TRS switches at 0200h and 0400h. Apparently even though the receivers are commanded to change TRS at the same second, the move into the new satellite time frame does not always take place at an exactly equal rate. In a practical system data collected for approximately one minute after a TRS switch would probably need to be discarded, and has been excluded from the analysis presented here.

Table 2.1 shows the offset error (mean), and random error (standard devia-

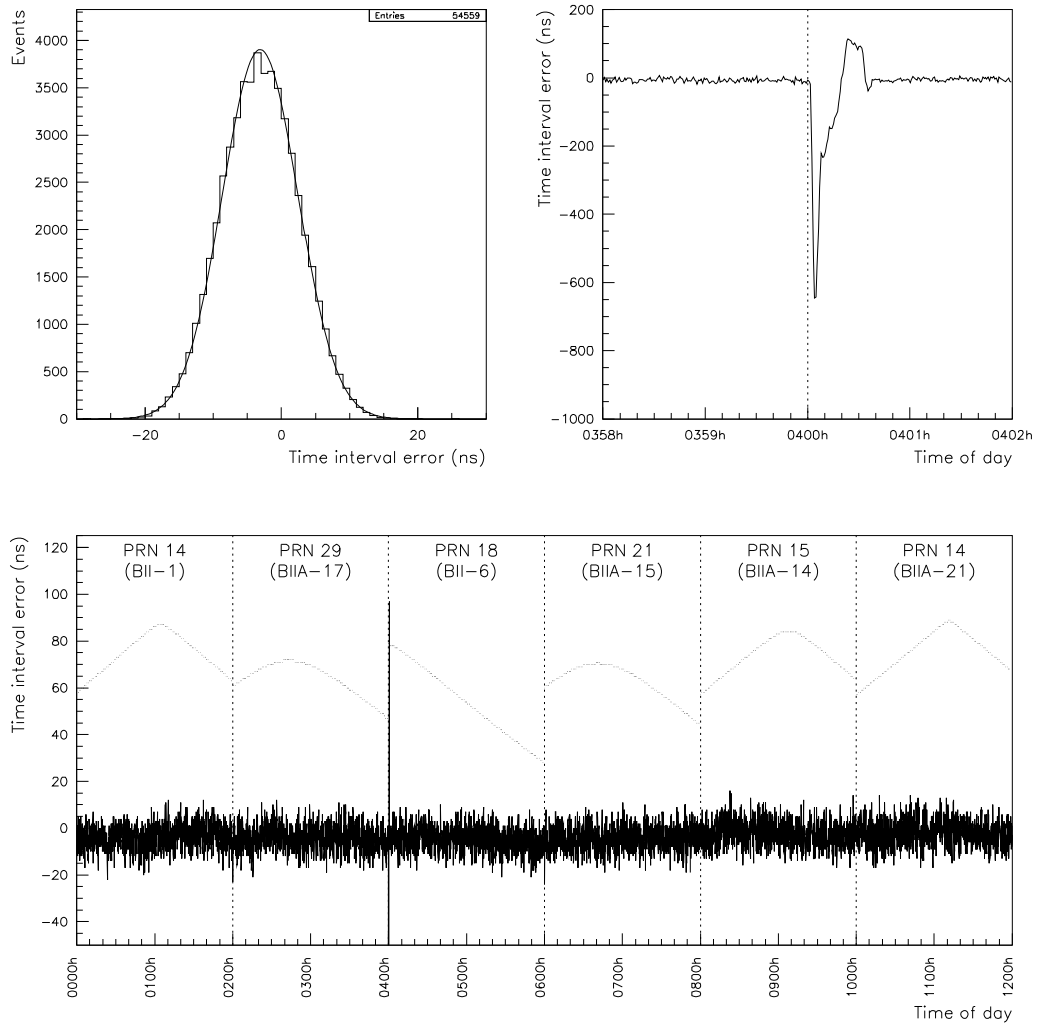


Figure 2.4: *Apparent event time difference with the time-stamping systems co-located during the morning of 2/4/94. The upper line of the lower plot shows the elevation angle of the satellite being used for time recovery, its PRN code being given at the top of the plot. The upper left plot shows the distribution of the data. The upper right plot is an expanded view of the switch-over transient at 0400h.*

| Day of run | Offset error in ns (mean) | Random error in ns ($\sigma$) |
|---|---|---|
| 2/4/94 am | $-3.6$ | 5.6 |
| 2/4/94 pm | $-4.4$ | 5.9 |
| 3/4/94 am | $-3.6$ | 5.6 |
| 3/4/94 pm | $-9.7$ | 6.7 |
| 4/4/94 am | $-6.2$ | 6.6 |
| 4/4/94 pm | $-4.5$ | 5.9 |
| 5/4/94 am | $-4.0$ | 5.7 |
| 5/4/94 pm | $-4.7$ | 5.9 |
| Average | $-5.1 \pm 0.8$ | $6.0 \pm 0.2$ |

Table 2.1: *Results from 4 days of running with the event time-stamping systems co-located*

tion) of the results from eight consecutive co-located 12 hour runs between 2/4/94 and 5/4/94. Since each run consists of $\approx 50,000$ data points, the fluctuations in these values are far larger than would be expected from simple random (Gaussian) behaviour, and are the result of the slow varying wander mentioned above. The average offset error and random error over the 4 day period are also shown in table 2.1, the error bounds being calculated on the assumption of Gaussian behaviour in these 8 observations, i.e. that the slow varying wander does not have significant components with characteristic periods $> 12$ hours. The peak time interval measurement errors recorded during the complete 4 day logging period were $+21$ ns and $-34$ ns.

**500 m separated results** Figure 2.5 shows the results from a typical 12 hour run with the event time-stamping systems separated by 500 m at the Haverah Park field station. Since the time-stamp from system #2 is subtracted from that from system #1, the time interval between the pulse leaving the central location and arriving at the far end of the cable is negative. Short term random jitter, and slower varying wander are apparent, as for the co-located run in figure 2.4.

The propagation delay of the cable was measured directly using a standing wave extrapolation technique [58], and found to be $2418 \pm 1$ ns. By adding this value to the apparent delay measured by the time-stamping systems values for offset error and random error were obtained. Table 2.2 shows these quantities for eight consecutive 500 m separated runs between 21/4/94 and 24/4/94. As for the co-located data, the fluctuations are far larger than would be expected from Gaussian statistics. The average offset error and random error over the complete 4 day period are also shown in table 2.2, the error bounds again being calculated on the assumption of Gaussian behaviour over time periods $> 12$ hours.

Since the average offset error for co-located ($-5.1 \pm 0.8$ ns) and 500 m separated runs ($-3.7 \pm 1.2$ ns) agree within their error bounds there is no evidence that the slow varying wander does in fact have significant components with characteristic periods $> 12$ hours, or that relocation of the systems caused a change in the long term fixed component of the offset error. Since the cable is buried beneath soil to a depth of $\approx 1$ m the possibility of a diurnal (temperature) variation in its propagation delay may be discounted.

The peak time interval measurement errors recorded during the complete 4 day logging period were +21 ns and $-35$ ns, a very close match to the co-located values.

**Interpretation of results** Since the timing counter runs at 100 Mhz the precision of each pulse marked is $^{+0}_{-10}$ ns maximum error with a rectangular distribution. Event time reconstruction via simple linear interpolation leads to a symmetrical triangular error distribution with a base from +10 ns to -10 ns. When event times are subtracted to give time intervals the error distribution is Gaussian in shape. A simple Monte Carlo simulation, which takes account of the small fluctuations in the 100 MHz oscillator frequency, indicates that a standard deviation of 5.3 ns would be expected if behaviour of the GPS receivers were perfect. The results

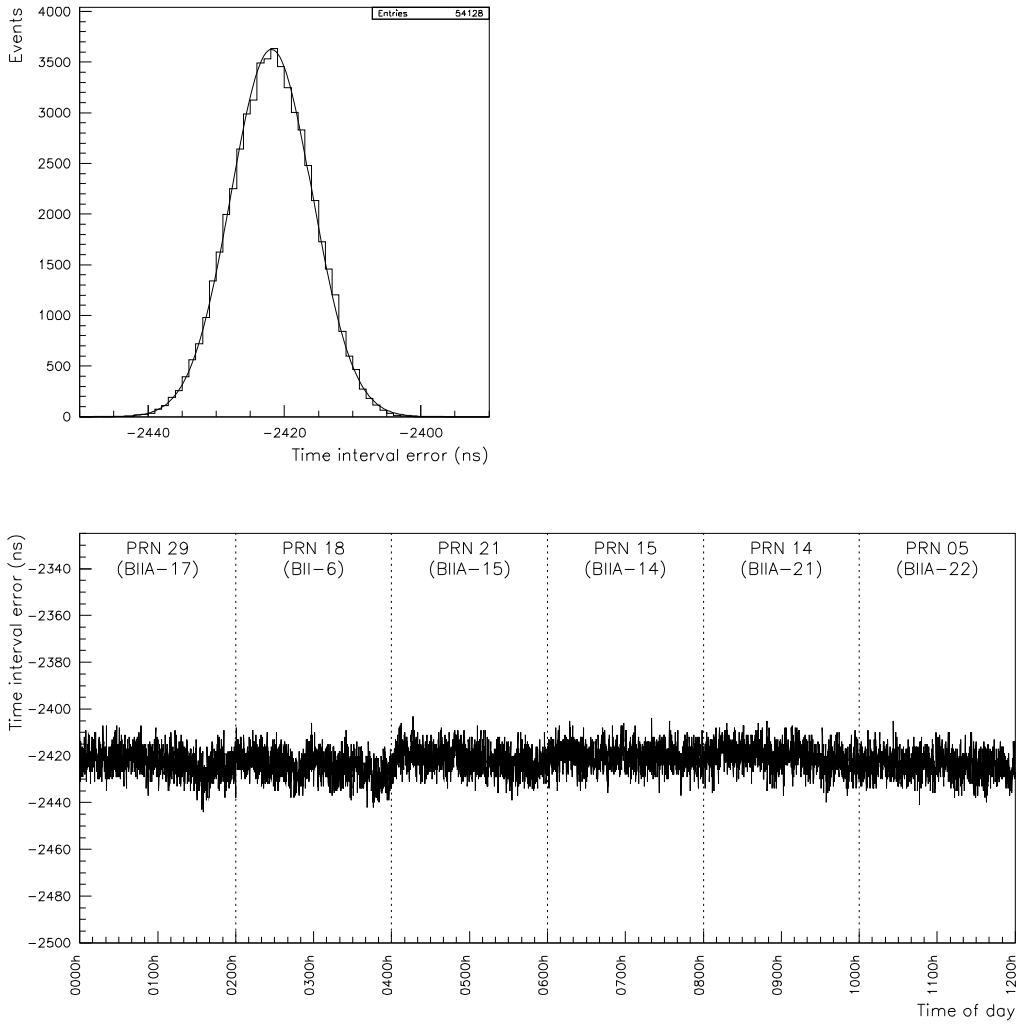


Figure 2.5: *Apparent event time difference with the time-stamping systems separated by 500 m during the morning of 21/4/94. This run is equivalent to that shown in figure 2.4. The PRN of the satellite is again shown at the top of the lower plot. The tracking schedule has been brought forward by 2 hours to compensate for the cumulative effect of the satellites rising four minutes earlier per day. The upper left plot shows the distribution of the data.*

| Day of run | Offset error in ns (mean) | Random error in ns ($\sigma$) |
|---|---|---|
| 21/4/94 am | $-4.3$ | 6.0 |
| 21/4/94 pm | $-3.9$ | 6.0 |
| 22/4/94 am | $-4.1$ | 6.2 |
| 22/4/94 pm | $-2.0$ | 5.9 |
| 23/4/94 am | $-7.0$ | 6.4 |
| 23/4/94 pm | $-2.1$ | 6.0 |
| 24/4/94 am | $-3.4$ | 6.0 |
| 24/4/94 pm | $-2.7$ | 5.9 |
| Average | $-3.7 \pm 1.2$ | $6.1 \pm 0.1$ |

Table 2.2: *Results from 4 days of running with the event time-stamping systems separated by 500 m*

of this simulation are shown in figure 2.6. It can be assumed that the additional random error observed is due to receiver noise, and the effect of the slow varying wander mentioned above.

The cause of the offset error, and the slow varying wander which leads to fluctuations of this error among the 12 hour data sets, is not fully understood. For the co-located case the antennae are exposed to exactly the same RF signal and environment, so effects such as mismatch of the atmospheric delay correction error, and multipath propagation can be discounted. There is certainly an internal delay mismatch between the two receivers. This can be demonstrated by swapping them over between the two time-stamping systems; some mirroring of the offset error about zero does occur. It is probable that a component of the slow varying wander is due to changes in this receiver delay mismatch, or possibly variations within the custom electronics. Also, it is probable that a component results from residual antenna gain pattern mismatch, even when the antennae are highly aligned. Preliminary testing indicates that any variation in the receiver delay mismatch is not linked with a temperature differential between the two systems. Additionally, if it

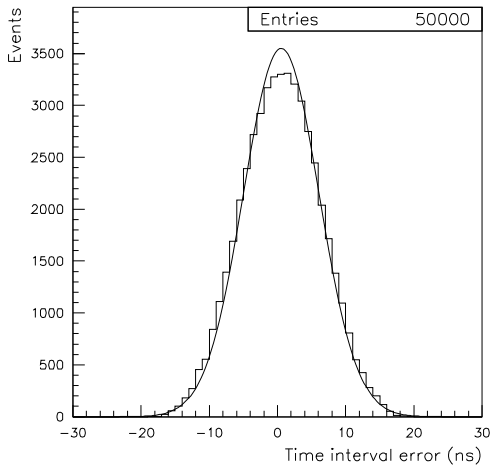


Figure 2.6: *Simulated time interval measurement error of event time-stamp system.*

were, a diurnal effect would be expected in the 500 m separated data sets, since the building at one location was thermostatically heated, whilst the other was not.

There is little evidence for multipath propagation error effects in the 500 m separated data, as performance is very similar to the co-located runs. However, it should be noted that the potential for this effect at the Haverah Park site is minimal, the ground being flat with few obstructions. It may be that in less favorable antenna environments this effect could degrade separated performance by $\sim 10$ ns. Multipath error may be reduced by the use of more expensive choke-ring type antennae.

### 2.4.2 Over an 11 km baseline using an L-band radio link

The footprint diameter of highly inclined ultra-large energy EAS at ground level can be as great as $\approx 10$ km. Hence testing of the GPS based event time-stamping system was carried out over a much longer baseline than the 500 m described in section 2.4.1. This was achieved by making use of an L-band radio phase transfer

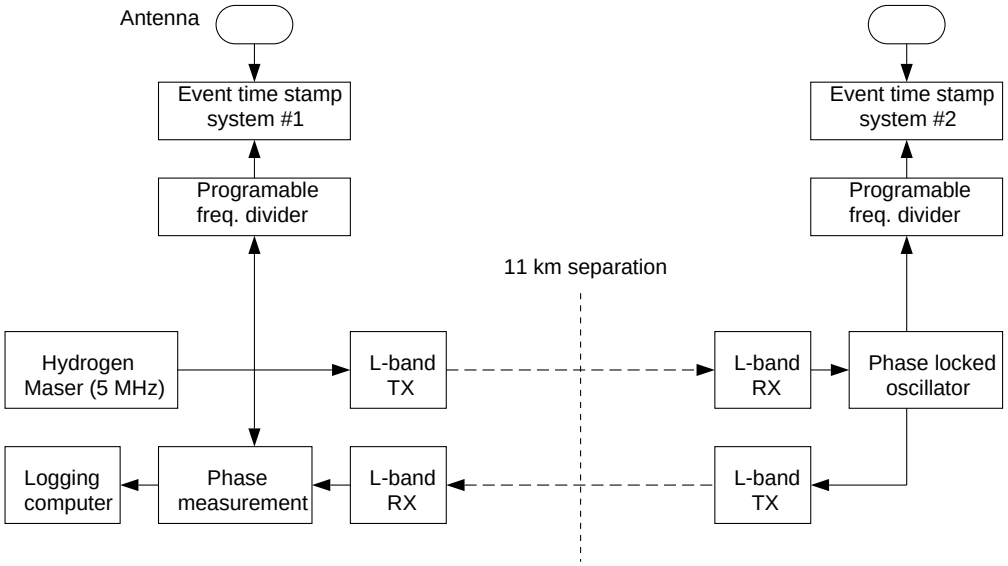


Figure 2.7: *Experimental set-up for 11 km separated event time-stamp system tests.*

link which forms a small part of the MERLIN long baseline radio interferometry experiment centered at the Jodrell Bank laboratories.

Figure 2.7 gives a simplified picture of the experimental setup. The outgoing L-band link allows the remote station oscillator to be phase locked to the central hydrogen maser. The absolute phase offset remains unknown since the absolute link delay is not measured. However, the remote oscillator wavetrain is re-broadcast back to the central site allowing any change of the link propagation delay to be monitored. Except during the most extreme weather conditions the delay is stable to $\ll 1$ ns over any 24 hour period.

By synchronizing the frequency dividers using the GPS 1 pps pairs of event pulses were generated 11.2 km apart, with a time delay between each pair of $\approx 200$ ms. The dividers were set such that the event pulse pairs stepped relative to the GPS 1 pps epoch at a rate of 3 ms $s^{-1}$.

Figure 2.8 shows the results from a typical 12 hour test run with the event time-stamp systems separated by 11.2 km. The increased wander of the short term mean compared to the co-located and 500 m separated data shown in figures 2.4 and 2.5 is due to one or more of the following effects:

- Incorrect antenna coordinates causing error modulation with satellite motion. Since the sky-view at the remote site was heavily obstructed by a large radio telescope dish the relative accuracy of the antenna coordinates derived via simultaneous position survey will have been reduced.
- Multipath reflection in the non-ideal antenna environments. This is the most probable cause since the wander appears to correlate with satellite elevation angle in a complex manner.

## 2.5 Conclusions

To measure the incidence angle of an EAS with $< 1^\circ$ error using a single baseline of 5 km a time interval measurement error of $< 130$ ns is required out as far as $60^\circ$ from the vertical (simple 2D case). However, although in the next generation experiment it is intended that data will be collected from detectors $\approx 3$ km or more from the shower axis, much better angular reconstruction accuracy will be possible using the time information from detectors closer in. Far from core the shower front is sparse and time dispersed, and hence poorly defined for a detector with practical area. Assuming a baseline of 1.5 km a time interval error of $< 40$ ns is implied. When adding in quadrature the $< 10$ ns rms total error which has been demonstrated above will have a negligible impact on the directional accuracy of the ground array system.

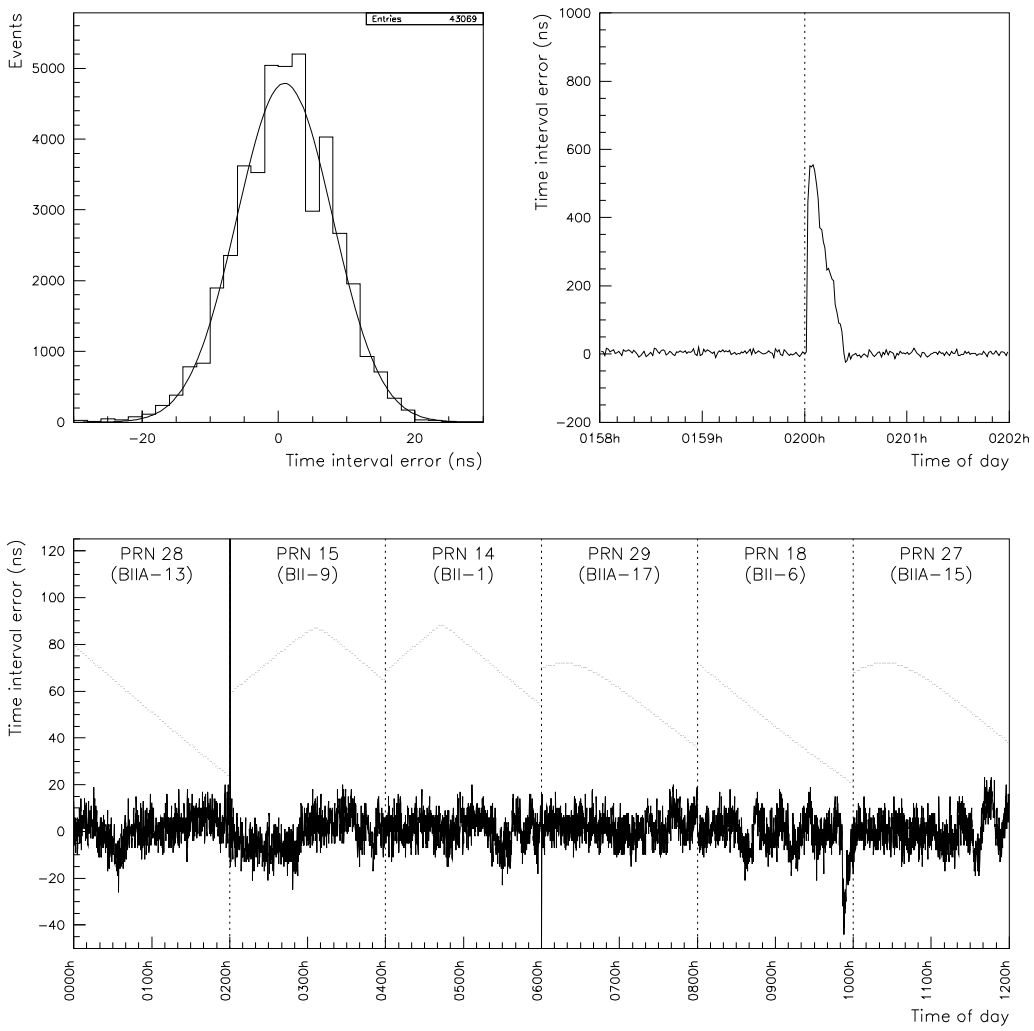


Figure 2.8: *Apparent event time difference with the time-stamping systems separated by 11.2 km during the morning of 26/1/95. The upper line of the lower plot shows the elevation angle of the satellite being used for time recovery, its PRN code being given at the top of the plot. The upper left plot shows the distribution of the data. The upper right plot is an expanded view of the switch-over transient at 0200h. Note that the arbitrary offset has been subtracted from the raw data (see text).*

The latest GPS receiver modules capable of high accuracy timing are now $<$ \$500 in quantity, and the market continues to develop rapidly[2] It therefore appears that this technology represents an excellent solution to the synchronization problem presented by an array of semi-autonomous EAS detector units.

[2]The Motorola Oncore VP is probably the best available unit for this application at the time of writing.

# Chapter 3

## Transient waveform capture using FADC devices

As mentioned in section 1.5.2 the feasibility of constructing a next generation detector of the highest energy cosmic rays is dependent on several areas of recent technological innovation. Due to the large number of surface detector stations to be deployed it is critical that the unit cost be kept as low as possible. Also, regardless of cost, for purely logistical reasons reliability must be very high. These two considerations severely constrain the range of particle detection techniques which can be envisaged.

However, the physics requirement that sufficient information be obtained in order that some measurement of the mass of the primary UHECR particles can be made, at least on a statistical basis, is highly contradictory with the above. For example the traditional approach to this problem has often been to attempt measurement of the muon/electron ratio of the shower using (expensive) buried muon counters, in conjunction with unshielded surface detectors.

In order to extract a maximal amount of information from a relatively simple particle detector a high speed transient capture system may be advantageous. Such systems are rapidly becoming cheaper to implement due to improvements in flash analogue to digital converter (FADC) technology. Another promising approach to this problem is the monolithic switched capacitor array which may be more suitable

in this application due to its intrinsically low power consumption, and lower cost of support circuitry.

To gain knowledge of, and experience with, FADC devices and systems a CAMAC transient capture module was designed by the author. The implementation and testing of this unit is described in the sections which follow. The module can be described as a general purpose laboratory and small scale experimental instrument. For the eventual giant array application a highly refined design would be required, and in any case, as already mentioned, technology is moving very rapidly in this area.

## 3.1 FADC technology

The FADC is a very simple, and inherently fast, analogue to digital converter architecture. It is in effect a "brute force" approach making use of one comparator for every possible output code; for an $n$ bit output $2^n$ comparators are required. A basic block diagram is shown in figure 3.1. The comparators are arranged as a ladder with one input of each being connected to the analogue signal to be digitized. The other input of each comparator is driven from the taps of a chain of precision resistors. A reference voltage defining the valid analogue input range is applied across this chain. Hence the comparator outputs are "on" up to the point where the resistor chain voltage is equal to the analogue input voltage, and "off" above that point. This "thermometer" code is then encoded to produce a conventional $n$ bit binary number in the required format.

Very large scale integration (VLSI) techniques have recently been applied to FADC design resulting in monolithic devices having up to 8 bit digitization ranges; 10 bit devices are also starting to appear. Clock rates have been pushed up, and several companies now offer 8 bit devices capable of operation at speeds as high as $\geq 500$ MSPS (Mega Samples Per Second).

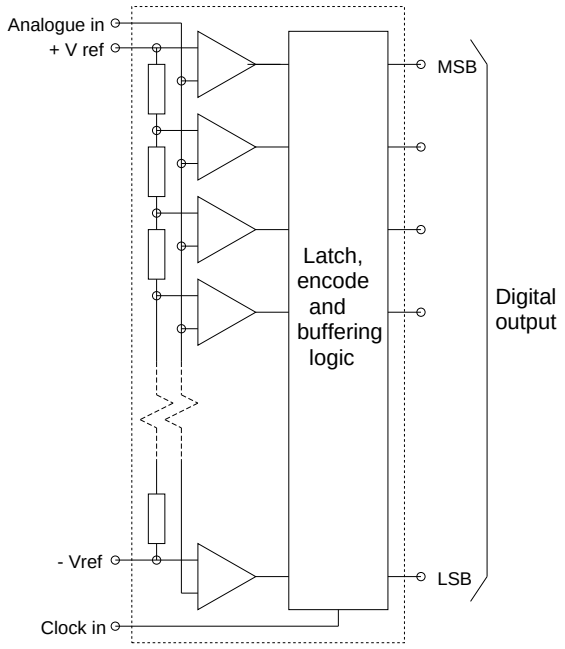


Figure 3.1: *Block diagram of an FADC device.*

## 3.2 Application and performance requirements

Due to the time spread of the shower front at large core distances ($\geq$ 1 km) in ultra-large EAS ($> 10^{19}$ eV) it is necessary to record up to $\approx$ 10 $\mu$s of time (see figure 4.2 in the next chapter). Due to the limited response speed of low cost large area detectors very little extra information will be derived by increasing the sample rate of the transient capture system beyond $\approx$ 200 MSPS. Currently available FADC devices capable of $>$ 40 MSPS have $\leq$ 8 bits. (However, since the recorded signal trace is dispersed in time the effective dynamic range of the system is far greater than this when considering the total time-integrated signal measurement.)

## 3.3 Description of the transient capture system

The CAMAC module which has been developed uses the CXA1176AK FADC device manufactured by the Sony corporation[1]. The complete system has the following performance specifications and features:

- Two independent channels in a single width CAMAC module.
- Sample rate of 100 MSPS with an 8 bit digitization range on both channels simultaneously.
- Analogue front end input bandwidth of $\approx$ 150 MHz ($-3$ dB).
- Programmable analogue input range of any 2 volts between $-2$ V and $+2$ V.
- Record length up to 16 K samples on each channel, programmable in 2 sample steps. (160 $\mu$s at full sample rate.)
- Pre-trigger samples programmable up to 100 % in 2 sample steps.
- Selectable internal triggering from either channel. Trigger thresholds programmable.
- External trigger input. Threshold front panel adjustable.
- External clock input. Threshold front panel adjustable.
- Trigger injection via CAMAC command for test purposes.

Figure 3.2 shows a block diagram of the transient capture system. Construction is on a four layer commercially produced PCB. The FADCs are clocked continuously, either from an internal 100 MHz frequency source, or from a front panel

[1]Due to problems with pricing and supply later versions of the unit use the Datel ADC308 device, a pin compatible equivalent part

input. When the module is armed the FADC output data is stored continuously into a variable length ring buffer implemented using fast SRAM, and a loop address counter. The fastest currently available SRAM cannot operate on a 10 ns write cycle, so a 1:2 multiplexing scheme is used to store into 2 banks of 20 ns memory. When a trigger event occurs, either internally or externally generated, a second counter is activated, and runs for a programmed number of clock cycles before halting the acquisition. The module then asserts a CAMAC LAM and waits for readout.

The FADC chips are surface mounted to avoid glitching problems which occurred in earlier versions. All other components are conventionally through-hole mounted. Front panel connectors are LEMO type. Power consumption and cost has been held down by use of the minimum possible quantity of ECL circuitry, 74ACT series being used wherever possible. Total power consumption of the complete module is $\approx$ 10 W at full sample rate on both channels.

## 3.4 Testing of the transient capture system

The CAMAC transient capture system was subjected to a range of tests which are described in the following sections:

### 3.4.1 Simple waveform tests and the beat frequency test

Digitization of simple lower frequency waveforms, whilst visually pleasing, is a poor test of transient capture system performance. The essential purpose of a high speed system is the recording of fast signals, and low frequency results do not extrapolate to higher frequencies. For instance limitations of the input buffer bandwidth, and

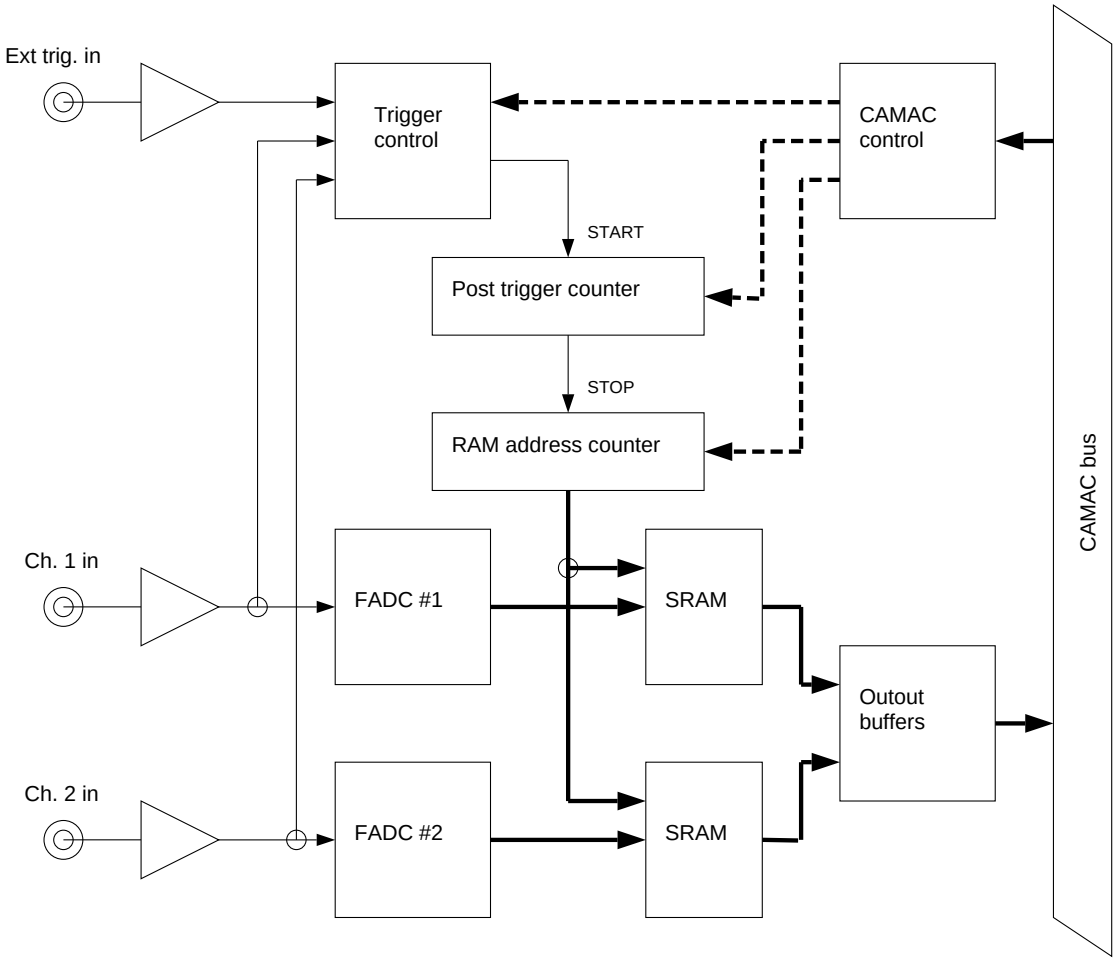


Figure 3.2: *Block diagram of the CAMAC transient capture system.*

sample epoch jitter are two key characteristics which determine performance, but which are only relevant when observing rapidly changing waveforms.

An alternative visual test which is more illuminating is the beat frequency test. By applying an input sinewave with frequency a few percent larger or smaller than half the sample rate an envelope curve is observed with period equal to the difference between these two frequencies [59]. The digitizer is thus being tested in a situation where the signal dynamics are close to the useful maximum, and limitations of the input buffer, sample epoch, and sample clock stability are clearly exposed. Figure 3.3 displays the results from simple 1 MHz sine, square and triangle capture, and beat frequency tests at 50.3 MHz for the two channels of a single module. Notice that the beat frequency envelope curves are smooth and monotonic for each rising and falling edge. There is little evidence of missing output codes; however, there is a small degree of asymmetry apparent which is probably due to slew rate limitation of the analogue input buffers.

### 3.4.2 MRPG test

For the giant array application the probable front end sensor type is the photo-multiplier tube (PMT). Hence it is interesting to view the module performance when capturing fast, large amplitude pulses from a mercury relay pulse generator (MRPG) — these pulses approximate closely in form to PMT pulses. Figure 3.4 shows the results of this test. The two channels of the module were connected to the MRPG in turn; the waveform trace from the unconnected channel is also shown. Note the extremely low quiescent noise of the system ($< 1$ bit), and small inter-channel cross-talk.

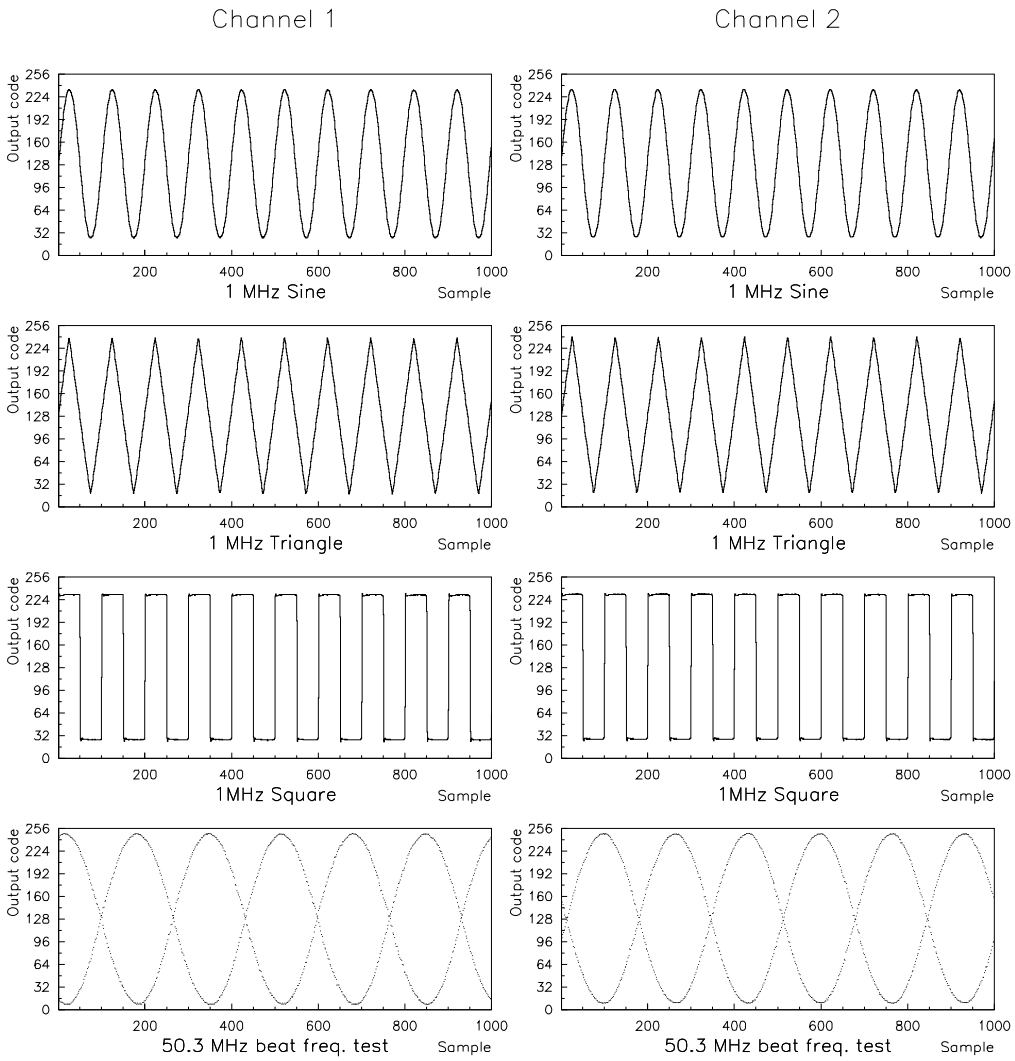


Figure 3.3: *Simple tests of the transient capture system performance. The left and right columns show results from the two channels of a single module.*

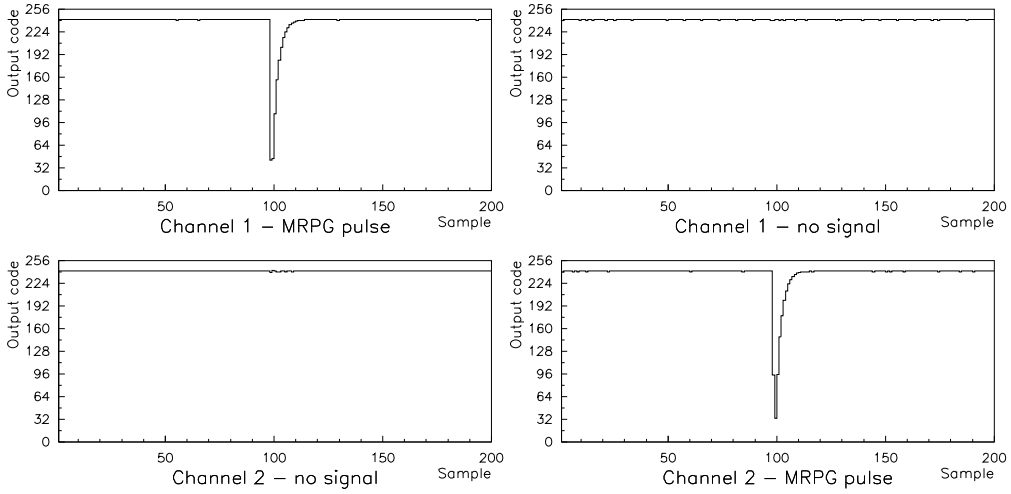


Figure 3.4: *Cross-talk test of the transient capture system performance. Channel 1 and channel 2 tests are shown to the left and right. In each case both the connected and unconnected channel traces are shown. Cross-talk and noise are seen to be small.*

### 3.4.3 Effective bits performance testing

A rigorous test of a transient capture system's dynamic performance is the effective bits test. The intent of this procedure is to provide a standard through which transient recorders may be compared to one another, and which encapsulates the performance of a unit within a single number for a given input frequency [60].

With the module running at maximum sample rate a series of input sinewaves with amplitude of $\approx 80\%$ full scale, at a series of selected frequencies are applied from a digital RF synthesizer, and data recorded using an arbitrary trigger. This data is then subjected to a curve fitting procedure with amplitude, DC offset, phase and frequency as free parameters. The fitted curve is then subtracted from that observed, and the distribution of the residuals generated. An ideal converter would exhibit a rectangular distribution between $\pm 0.5$ bits. The theoretical rms quantization error $\Psi_{ideal}$ of an ideal digitizer is found mathematically to be $1/\sqrt{12}$ bits

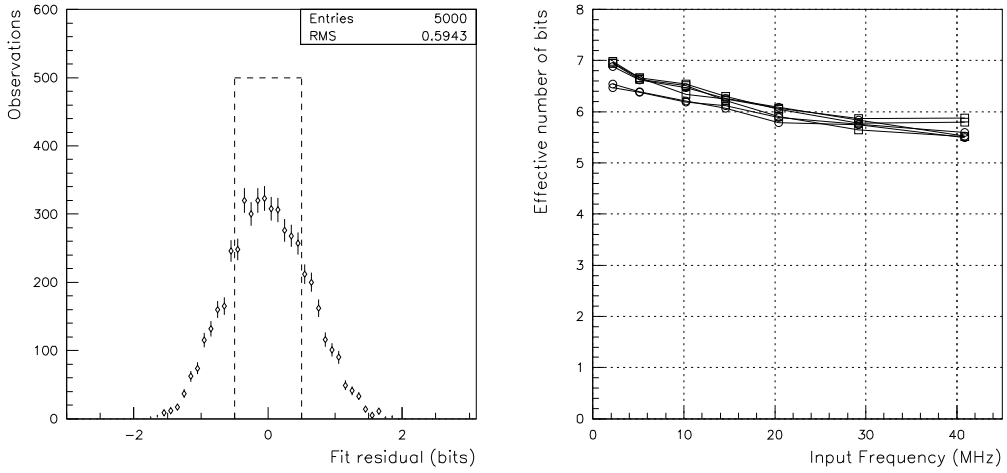


Figure 3.5: *Effective bits test of the transient capture system performance. On the left the distribution of the fit residuals is shown for a single channel at a particular frequency. The distribution which would correspond to ideal behaviour is also shown as a broken line. On the right the resulting effective bits parameter is plotted; points are shown for the 6 channels of 3 modules.*

(= 0.289 bits) [61]. The effective number of bits (ENB) is defined to be,

$$ENB = N - \log_2 \left( \frac{\Psi_{act}}{\Psi_{ideal}} \right),$$

where N is the nominal number of bits, and $\Psi_{act}$ is the rms value of the curve fit residuals.

In figure 3.5 the distribution of the fit residuals is shown for a single channel at a single frequency. The resulting effective bits parameter calculated using the above equation is also plotted at 7 input frequencies for several different module channels. The observed value of $\leq 7$ bits is a little disappointing since the FADC device itself has better inherent characteristics [62]. However, it was clear that some portion of the apparent non-ideal error was due to limitations of the RF synthesizer being used, rather than the transient capture module itself[2]

[2]Two different RF synthesizers which were tried gave significantly different results, showing

## 3.5 Conclusions

A versatile 2 channel 100 MSPS transient capture module has been designed, implemented and tested. Specifications and performance are comparable to the LeCroy model 6841, a unit costing $\approx$ \$5000. Three of the modules have been deployed at the South Pole to record air Čerenkov pulses from EAS in conjunction with the SPASE-II experiment.

For the next generation detector of the highest energy cosmic rays a much more highly refined and simpler design will be required to reduce the power consumption and cost as far as possible. Investigation of monolithic switch capacitor array devices is strongly recommended.

that limitations of sinewave purity and stability were affecting the test procedure. Unfortunately a generator of known performance was not available.

# Chapter 4

## Predicted nature of the EAS front with reference to water Čerenkov detectors

At ground level, far from the core of an EAS, the shower front consists of a "swarm" of gammas, electrons and muons. There is also a flux of (evaporation) neutrons which are generally sub-relativistic, and so delayed with respect to the main shower front, and large numbers of atmospheric Čerenkov photons. The relativistic hadron flux is negligible beyond 50 m from the core.

To design an optimal detector for a sparse ($\approx$ 1.5 km spaced) ground array it is necessary to have information regarding the characteristics of the shower front at large distances from the core. In this work the MOCCA EAS simulation program written by A. M. Hillas has been employed to this end [63, 64]. MOCCA[1] (MOnte Carlo CAscade) is a highly detailed 4-dimensional cascade simulation incorporating a realistic atmospheric model, and implementing a "thin-sampling" technique. The specifics of the shower simulation code will not be discussed here.

A $10^{19}$ eV EAS consists of $\sim 10^{10}$ particles at shower maximum. It is thus impossible to follow every particle unless truly enormous computational resources were to be available. Shower simulations such as MOCCA employ the thin-sampling technique whereby below a certain threshold energy only a fraction of

[1]The copy of MOCCA used for all of the work described here is the "Chicago" version called "mocorbin_ze".

the particles are followed, these being assigned weights to conserve total energy. This process works very well in terms of massively reducing the required computation time, but has limitations for the present application.

In this chapter the technique used to mitigate the effect of the thinning limitation is described, and some investigation of MOCCA's predictions regarding the nature of the shower front at large core distances is presented. For the reasons discussed in Chapter 1 it is important that a next generation EAS experiment should have the maximum capability for determining the mass of the primary cosmic ray particles which can be achieved at realistic cost. Thus it is necessary to investigate the predicted differences at ground level between showers of different types in order to optimize the detector unit and experimental configuration for this purpose. As two extreme examples proton and iron primaries have been used in the simulations. The response of a deep water Čerenkov detector to the predicted shower front is then investigated, with special reference to the expected differences between heavy and light initiated showers.

## 4.1 EAS simulation methodology

The fraction of the number of shower particles reaching ground level which are at large core distances ($> 1$ km) is extremely small ($\ll 0.1\%$), and hence in this region the shower-to-shower fluctuations caused by the thinning process come to dominate. To remove these artificial fluctuations large sets of showers have been run under the same initial conditions and the average of each set taken.

Batches of 100 showers have been generated for proton and iron nuclei primaries at 0°, 30°, 45° and 60° zenith angles. All the simulations are for primary energy of $1 \times 10^{19}$ eV, and an atmospheric depth at ground level of 1000 g cm$^{-2}$ (close to sea

level). The thinning threshold was set to $10^{-6}$ of primary energy (10 TeV). This effort represents several thousand hours of CPU time on current state-of-the-art workstations.

Output from MOCCA is in the form of a ground particle list giving particle type, impact coordinates, trajectory, energy, arrival time, and weight. To allow simple visualization, and as a first step in the full array simulation process which is described in Chapter 6, these output lists have been binned into multi-dimensional arrays. Each particle is projected onto the plane perpendicular to the shower axis, and passing through the core impact point, and then added to a 5-dimensional array to give differential numerical flux density for each particle type in each energy/time bin, at each interval of core distance. Only gamma, electron and muon particles are recorded.

There are 20 logarithmic intervals of core distance (10 per decade from 0.05 km to 5 km), 30 logarithmic intervals of time (10 per decade from 0.01 $\mu$s to 10 $\mu$s), and 40 logarithmic intervals of particle energy (5 per decade from 0.1 MeV to 10 TeV), giving a total of 24,000 bins for each particle type[2]. Positive and negative electrons are binned together, as are positive and negative muons. Unfortunately the statistics available from 100 runs do not allow further dimensions of binning such as impact position sector relative to the shower axis, and particle trajectory angle.

This procedure smoothes out the fluctuations induced by the shower thinning process, but also loses the physical fluctuations which are due to variations in the atmospheric depth of the first interaction point, and in shower development. Additionally any shower asymmetry at ground level due to geomagnetic effects

[2]Bin upper edge values are given by $r_u = 0.05 \times 10^{i/10}$, where $1 \leq i \leq 20$ and $r_u$ is in meters, $t_u = 10 \times 10^{i/10}$, where $1 \leq i \leq 30$ and $t_u$ is in ns, and $E_u = 0.1 \times 10^{i/5}$, where $1 \leq i \leq 40$ and $E_u$ is in MeV. Note that particles arriving at $t < 10$ ns are placed in the first time bin.

and, for non-vertical showers, additional attenuation across the shower footprint, will be lost in this process.

## 4.2 Predicted nature of the shower front

Figure 4.1 shows the mean differential numerical flux density at 0.9 km as derived from the batch of 100 simulated showers run on the basis of vertical proton primaries. The flux is shown as $d^2N/d\log(E)d\log(t)$ m$^{-2}$, i.e. the number of particles arriving per m$^2$ in each logarithmic bin of energy and time. A correlation between particle energy and arrival time is seen for both gammas and muons, although curiously to a much lesser extent in the case of electrons[3]. This figure demonstrates the highly detailed information which is available from the shower simulation runs. However, to ease interpretation it is useful to integrate the arrays, first in the dimensions of time and energy separately, and then in both these dimensions simultaneously.

Figure 4.2 is derived from data of the type displayed in figure 4.1 and shows the time integrated energy spectra and energy integrated time profiles of the shower components. These are shown both as the numerical particle flux densities $dN/d\log(E)$ & $dN/d\log(t)$ m$^{-2}$, and the energy flux densities $dE/d\log(E)$ & $dE/d\log(t)$ MeV m$^{-2}$; plots for 4 annular core distance bins are shown. There are several things to note:

- The gammas dominate over the electrons by a factor of $\approx 10:1$, both in terms of numerical density and energy density at each core distance.
- The energy spectra of all the shower components soften slightly with increas-

[3]It was suggested to me by Alan Watson that this may be because some of the low energy electrons are produced "locally" by the muons and high energy gammas.

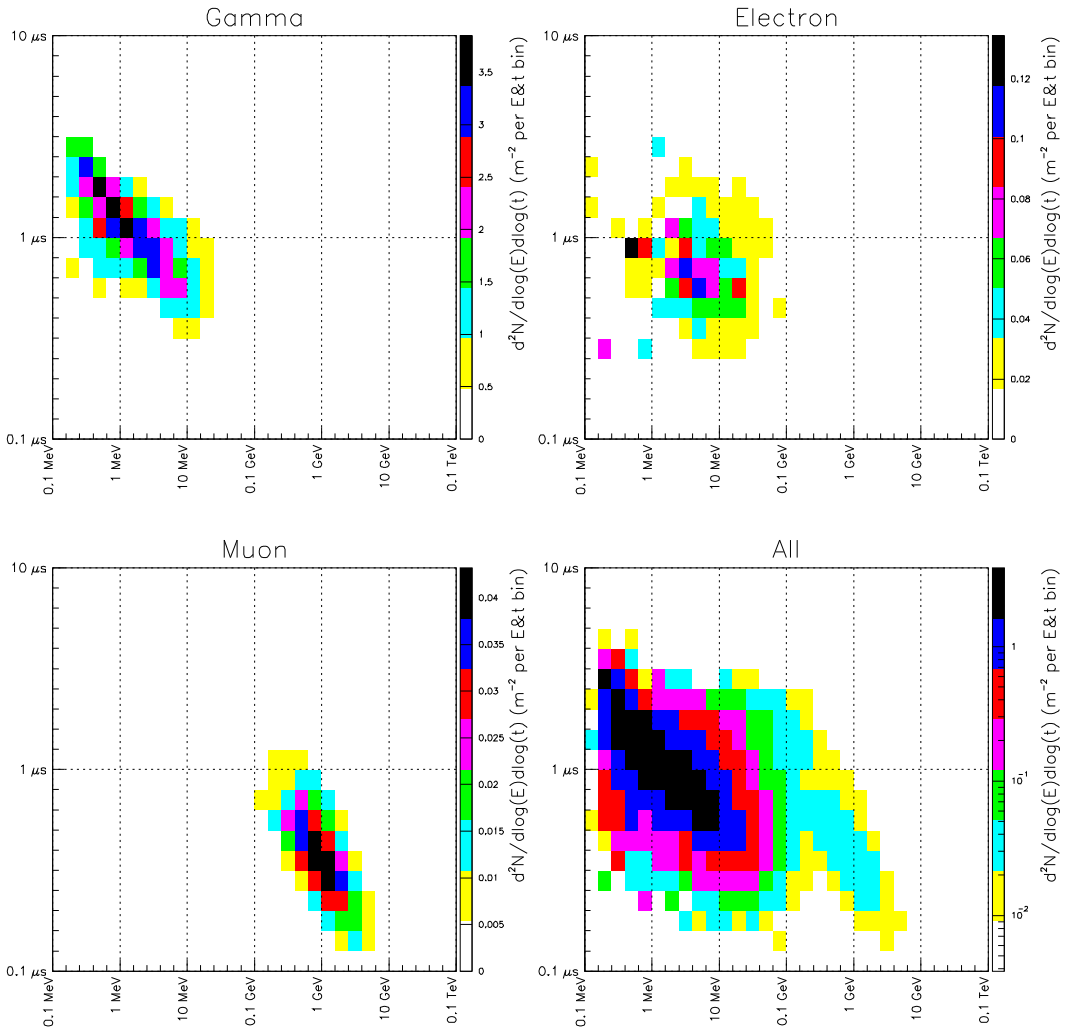


Figure 4.1: *Differential numerical flux density of shower particles at 0.9 km from the core of a $10^{19}$ eV EAS, as predicted by shower simulation. The colour scale shows the flux in units of particles $m^{-2}$ per logarithmic time and energy bin. $\gamma$, e and $\mu$ components are plotted separately, and an all particles plot is also shown. Note that the numerical flux density scale for the all particles plot is logarithmic to allow the muons to be seen on the same scale as the electromagnetic particles. (These plots represent the mean of 100 vertical proton-initiated runs, assuming ground level atmospheric depth of 1000 g $cm^{-2}$.)*

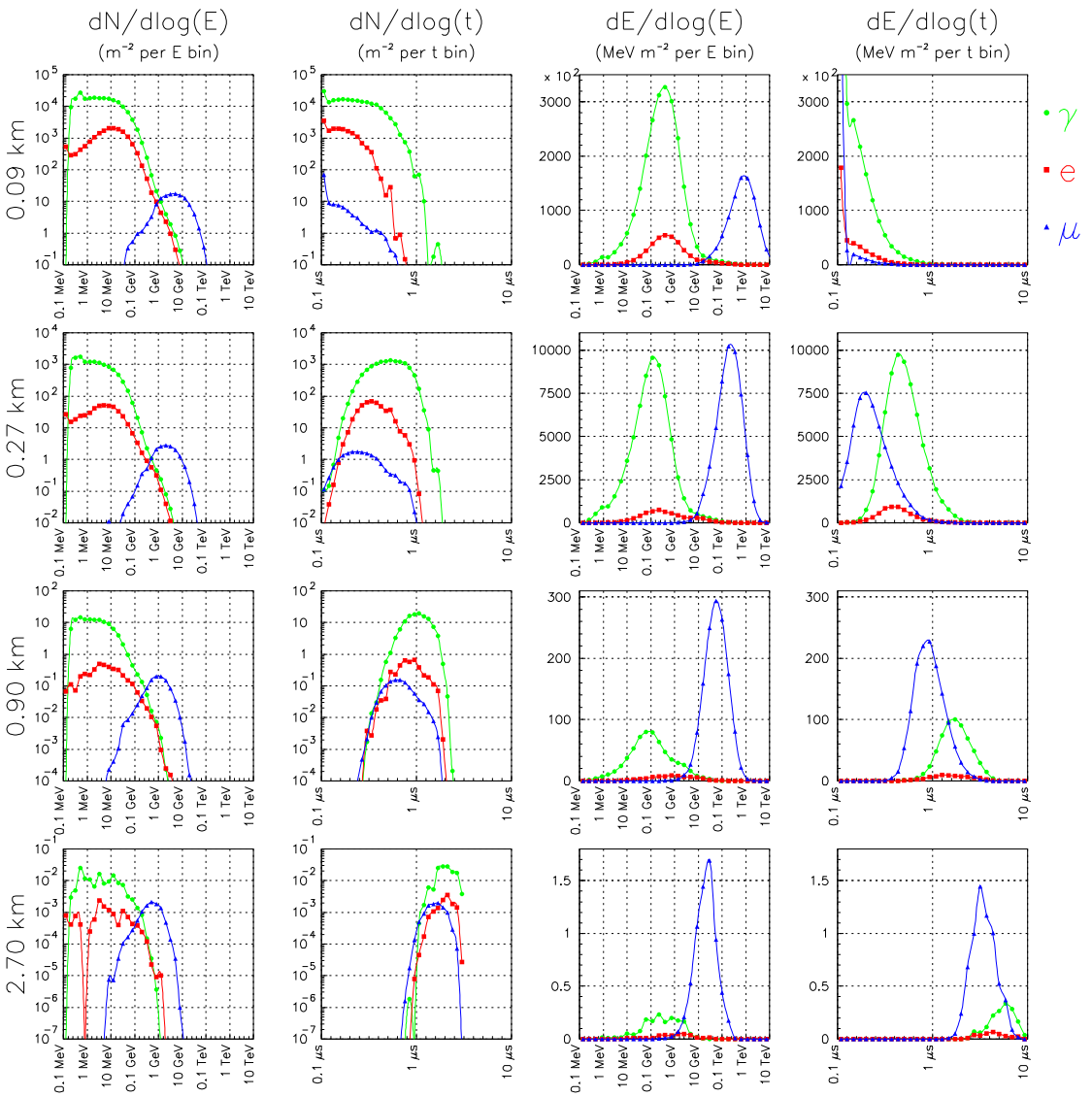


Figure 4.2: *Differential energy spectra and time profiles of particles at four distances from the core of a $10^{19}$ eV EAS, as predicted by shower simulation. The key is the same for each plot and is shown at top right. The quantity being plotted is indicated at the top of each column, and the core distance to the left of each row. Note that the vertical axis scale is logarithmic for the numerical density plots, and linear for the energy density plots. (These plots represent the mean of 100 vertical proton-initiated runs, assuming ground level atmospheric depth of 1000 g cm$^{-2}$.)*

ing core distance; e.g. the peak of the muon $dN/dlog(E)$ distribution falls from $\sim$ 10 GeV at 90 m from core to $\sim$ 1 GeV at 2.7 km.

- The fraction of the total energy flux reaching ground level which is muonic increases with core distance. Far from the core the bulk of the total energy flux is carried by the shower muons.

- The increasing delay of the shower front with increasing core distance is clearly seen, as is its increasing time dispersion with core distance.

By integrating the shower simulation output arrays in the dimensions of particle energy and arrival time simultaneously lateral distribution plots of the predicted numerical and energy flux densities may be generated. Figures 4.3 and 4.4 show the results from the 8 large batches of Monte Carlo showers which were generated.

The detailed predictions shown in figures 4.1 and 4.2 are in good qualitative agreement with measurements made at Haverah Park and elsewhere, albeit mostly at smaller core distances in showers several decades lower in energy [65, 7]. However there are many reasons to believe the MOCCA results to be essentially correct even at energies $\geq 10^{19}$ eV, the ability to reproduce water Čerenkov lateral distribution shapes being particularly persuasive in this regard (see Chapter 6).

At ground level the expected differences between showers initiated by primaries as disparate as protons and iron nuclei are not great; figure 4.5 shows the predicted numerical and energy flux density ratios for each shower component. We can see that the electromagnetic ratios are close to unity, rising from somewhat less than one with increasing core distance. The reason for this is almost certainly as follows. Iron nuclei have a larger interaction cross section and hence on average start to shower higher in the atmosphere. At ground level iron-initiated showers will therefore be further past shower maximum, and close to core the electromagnetic

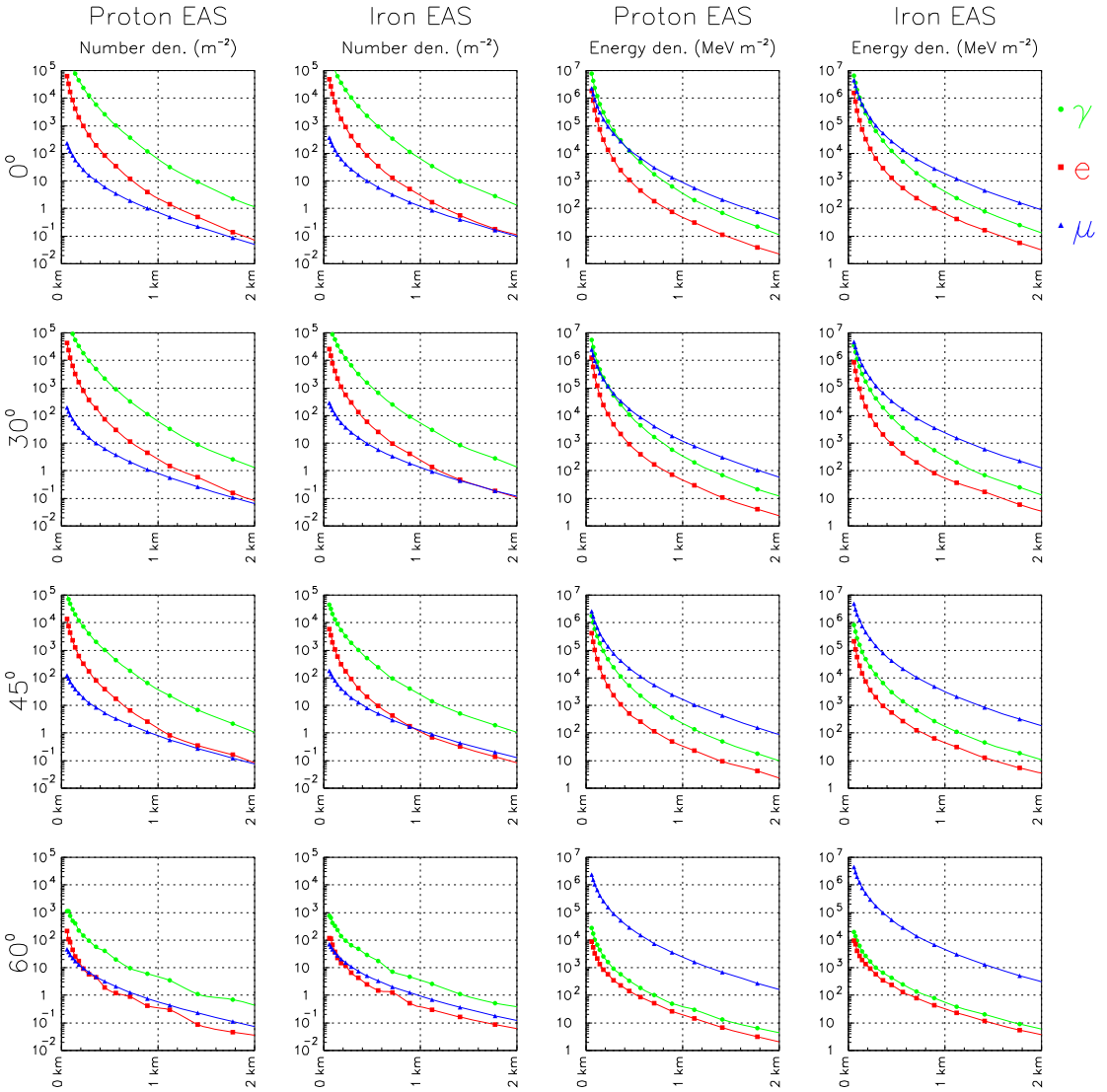


Figure 4.3: *Comparing the lateral distributions of the shower components for $10^{19}$ eV EAS, as predicted from shower simulation. Both numerical flux density and energy flux density plots are shown for proton and iron-initiated showers at $0, 30°, 45°$ and $60°$. The key is the same for each plot and is shown at top right. The shower type and quantity being plotted are indicated at the top of each column, and the shower incidence angle to the left of each row. Note that at core distances $> 100$ m the bulk of the shower energy flux is carried by the $\mu$ component. (These plots represent the mean of batches of 100 showers each, assuming ground level atmospheric depth of 1000 g cm$^{-2}$.)*

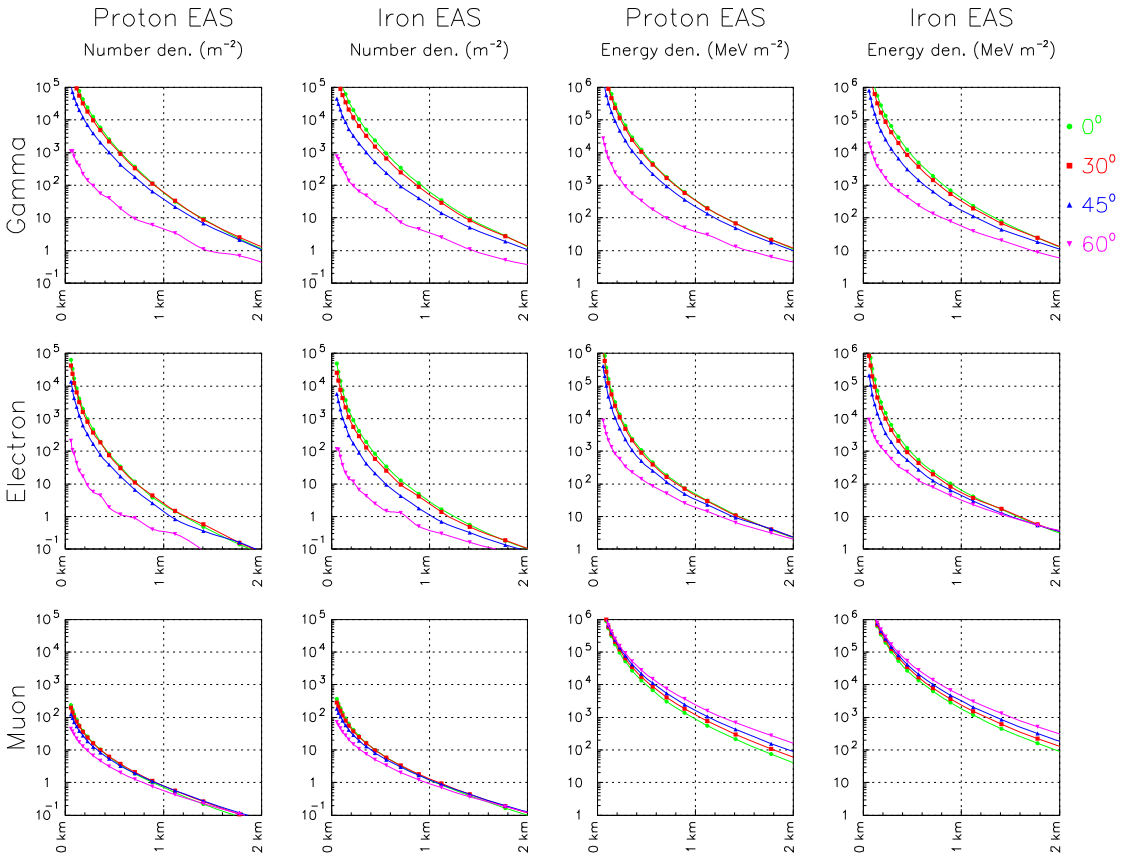


Figure 4.4: *Comparing the lateral distribution at four zenith angles for $10^{19}$ eV EAS, as predicted from shower simulation. This figure re-displays the same data as figure 4.3. Both numerical flux density and energy flux density plots are shown for the $\gamma$, e and $\mu$ components of proton and iron-initiated showers. The key is the same for each plot and is shown at top right. The shower type and quantity being plotted is indicated at the top of each column, and the shower component to the left of each row. Note that the $\mu$ numerical flux density falls much more slowly than that of the electromagnetic particles with increasing zenith angle, and that the corresponding energy flux density actually rises. (These plots represent the mean of batches of 100 showers each, assuming ground level atmospheric depth of 1000 g cm$^{-2}$.)*

cascade has been attenuated more than in the case of later developing proton-initiated showers of equal energy. However, the divergence of particles from the shower axis grows with increasing atmospheric depth for simple geometric reasons, and also due to multiple scattering, and hence the fraction of particles beyond any given core distance also grows. It is probable that these two effects combine to give the predicted behaviour.

Note that there are 50–100% more muons in the iron-initiated showers, the ratio rising somewhat with core distance, and falling somewhat at increasing zenith angles. This may be understood as follows. Shower muons have their origin in charged pion decay. The fraction of the initial shower energy which is given to the muonic component falls with increasing energy. An iron-initiated shower may crudely be thought of as the superposition of 56 proton-initiated showers of correspondingly lower energy, and hence it is easy to see that iron showers are expected to be "muon-rich" when compared to proton showers. Figure 4.5 also shows that the mean muon energy is also predicted to be somewhat higher in iron-initiated showers.

Although the absolute number of muons for a shower of given energy and primary type is dependent on the details of the hadronic interaction model used, the difference ratios between proton and iron-initiated showers displayed in figure 4.5 are much less model dependent [34]. Hence an experimental system capable of measuring a parameter sensitive to the muon to electromagnetic ratio would require reference to uncertain Monte Carlo results to make an absolute determination of the primary mass of observed showers. However, if, for instance, the hypothesis of a mixed composition were made such a detector would be able to split the observed data into "heavy like" and "light like" fractions with much less model dependency. Such a capability might be extremely important in anisotropy analysis etc.

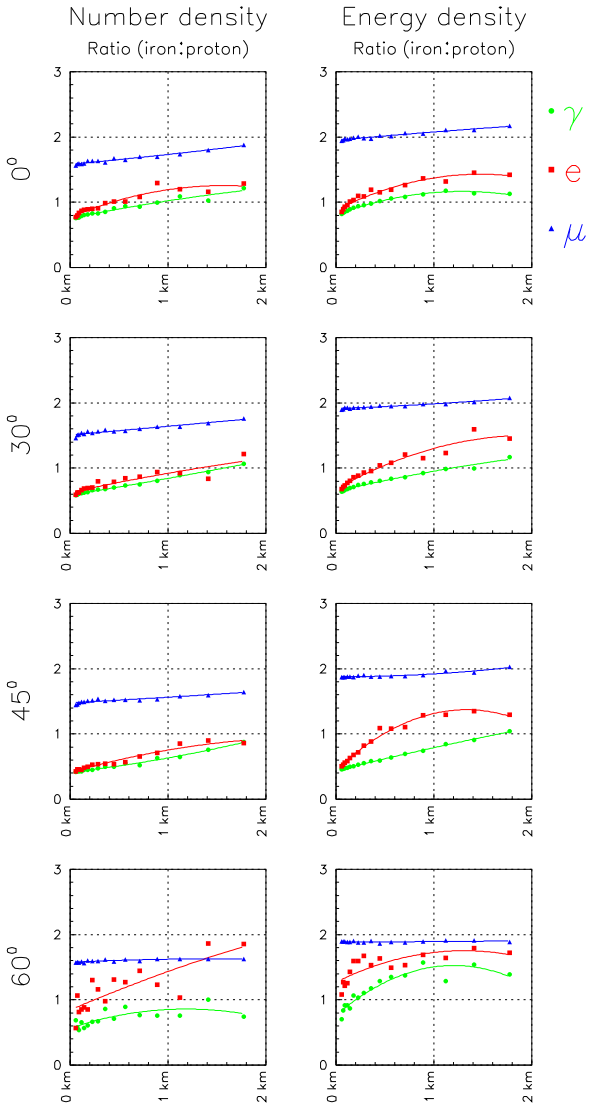


Figure 4.5: *Comparing the lateral distributions of showers initiated by $10^{19}$ eV proton and iron primaries, as predicted from shower simulation. The ratios of the numerical flux density and energy flux density are shown at $0, 30°, 45°$ and $60°$. The key is the same for each plot and is shown at top right. The quantity being plotted is indicated at the top of each column, and the shower incidence angle to the left of each row. Note that the muonic ratios are consistently higher than the electromagnetic ratios. (These plots represent the mean of batches of 100 showers each, assuming ground level atmospheric depth of 1000 g cm$^{-2}$.)*

## 4.3 Response of a water Čerenkov detector

The discussion and figures in the previous section are equally useful when considering the response of a ground array of particle detector units of any type to incident EAS. From here on the discussion is focused exclusively on water Čerenkov detectors, these having been selected as the favoured technology for the next generation experiment (see section 5.1 for justification of that selection).

Detailed consideration of the interaction of the shower particles with the mass of a water Čerenkov detector is presented in the next chapter. In this section the general implications of figure 4.2 are investigated. Note that the shower muons are rather hard, the peak of the $dN/d\log(E)$ distribution being at $E \geq 1$ GeV right out to the largest core distances, while the electromagnetic particles are rather soft, the equivalent distributions peaking at $E \leq 10$ MeV. The rate of energy loss for a minimum ionizing particle in water is $\approx 2$ MeV cm$^{-1}$. Hence for water of practical depth ($\approx$ 1 m) a large fraction of the muonic energy will "punch through" the detector volume. However, the majority ($\approx 85\%$) of the electromagnetic energy will be absorbed (mean free path of gammas in water is $\leq 0.5$ m).

> *Hence the total time integrated water Čerenkov signal density is to a first approximation proportional to the muonic numerical density plus the electromagnetic energy density.*

### 4.3.1 Primary type sensitivity through direct $\mu$:em signal ratio measurement

As stated in section 1.5.1 sensitivity to the chemical composition of UHECR is a key goal for a next generation experiment. On the basis of the above statement

regarding water detector response, the first column of figure 4.6 re-displays the relevant iron:proton ratios from figure 4.5. The ratio of the total electromagnetic energy density, and the ratio of the muonic numerical density, are both seen to rise somewhat with increasing core distance. Making the following approximations it is possible to get an indication of the muonic to electromagnetic signal fraction expected for a given water depth:

- That energy deposition is approximately proportional to Čerenkov light yield.
- That the mean muon track length is 1.2 m, and hence that they deposit an average of 240 MeV each.
- That all the incident electromagnetic energy is absorbed.

Close to the shower core ($\leq$ 100 m) the last approximation will break down as some of the increasingly hard electromagnetic energy starts to penetrate through the detector (see figure 4.2). Note that the muonic to electromagnetic signal ratio is a strong function of core distance. In a real experimental situation this is an undesirable feature in a parameter which is to be used in primary type separation. Errors in core location will lead to errors in primary type classification. However, the predicted difference of the ratio between primary types is rather constant at increasing zenith angles up to 45°.

The above discussion is only useful if a water Čerenkov detector can somehow be devised which is capable of separating the muonic and electromagnetic fractions of the total signal which it records. At first sight this may appear to be impossible. However, by exploiting the increasing time dispersion of the shower front at larger core distances, together with the much harder energy spectra of the muonic component it may be possible. Muons penetrating through deep water detectors will release short, large bursts of light early in the time profile of the shower compared

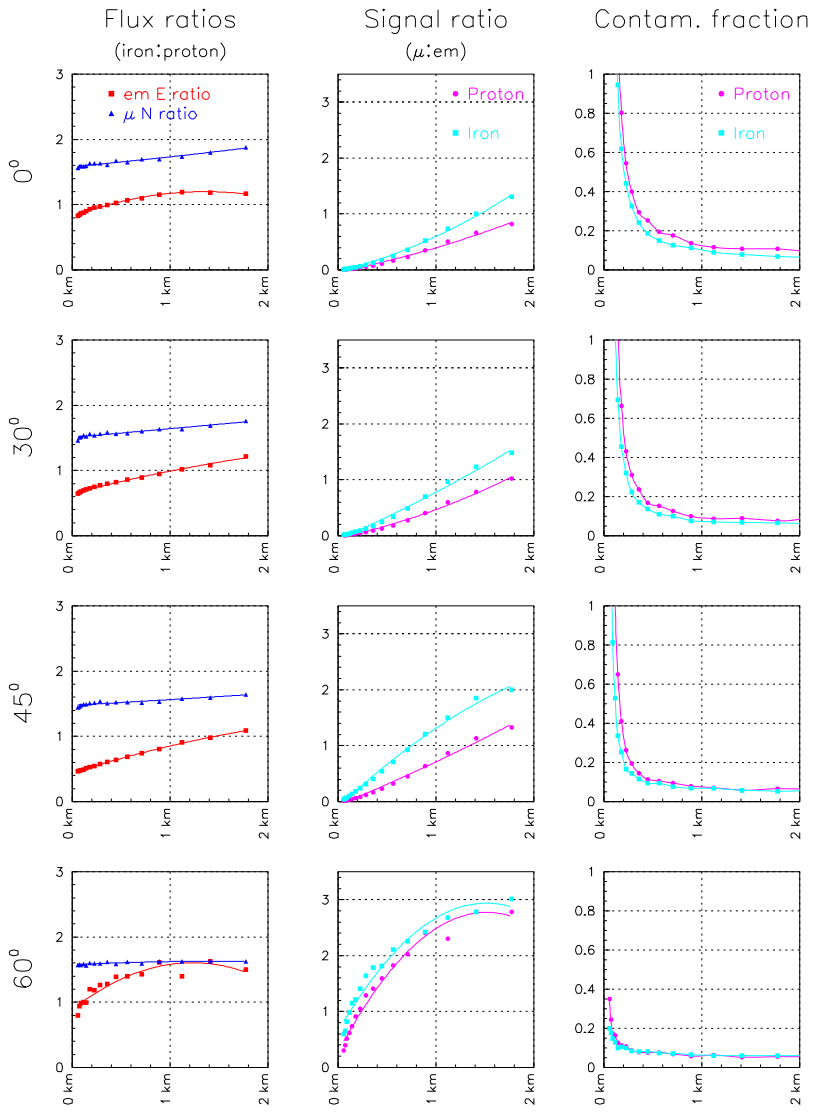


Figure 4.6: *Lateral distribution ratios relevant to primary type discrimination by direct μ:em signal ratio measurement using water Čerenkov detectors. The quantity being plotted is indicated at the top of each column, and the shower incidence angle to the left of each row. The key is the same for each column and is shown at the top of that column. In the first column the ratio of the total energy density carried by electromagnetic particles in iron and proton-initiated showers is plotted, with the numerical density ratio of the muons. The second column shows the approximate μ:em signal ratio for a water Čerenkov detector 1.2 m deep (see text). The final column shows the "contamination fraction" (see text). (These plots represent the mean of batches of 100 showers each, assuming ground level atmospheric depth of 1000 g cm$^{-2}$.)*

to the much more numerous, but lower energy, electromagnetic particles, which individually release only small amounts of light.

Using a modern transient capture system (probably an FADC) attached to the Čerenkov light detector output it may be possible to recognize the characteristic muon pulses, and hence to separate the observed signal into muonic and electromagnetic fractions[4]. This will only ever be practical at large core distances ($\geq 1$ km) where the density is such that near simultaneous particle arrival, (dubbed "pile-up"), effects do not dominate. The proposed technique is predicated on the assumption that few individual electromagnetic particles have sufficient energy to generate as much Čerenkov light as a penetrating muon, since if they do they will be indistinguishable.

The third column of figure 4.6 shows the predicted "contamination fraction" of electromagnetic "fake muons"; at core distances $\geq 1$ km this is $\leq 15\%$. To first approximation an electromagnetic particle entering a water Čerenkov detector 1.2 m deep with energy $> 250$ MeV will produce an equal, and indistinguishable, burst of light to a muon entering with energy $> 400$ MeV. (The difference in the required energy is due to the higher mass of muons — see figure 5.6 in the next chapter.) Note that the hard electromagnetic component attenuates rapidly at increasing zenith angles. It is probable that the 7% which remains even at zenith angle of 60° is almost entirely secondary to the shower muons themselves, and hence does not strictly represent contamination.

This proposed muon recognition technique also demands that the proportionality of the detector be good; i.e. that the signal observed be closely proportional to the Čerenkov light deposited. It is important to realise that the "fake muon" fraction discussed above is the *lower limit* fixed by the nature of the shower par-

[4]This suggestion was made by James Cronin.

ticles themselves; a practical detector will inevitably be poorer. In the following two chapters further consideration is given to the potential, and limitations, of this direct muonic to electromagnetic signal ratio measurement.

### 4.3.2 Primary type sensitivity by measurement of shower front time dispersion

The arrival time dispersion of the water Čerenkov signal is a parameter which is sensitive to primary particle mass. (At Haverah Park a parameter dubbed rise time, or $t_{1/2}$, defined as the 10% to 50% signal arrival time interval, was measured and used to infer information regarding depth of shower maximum $X_{max}$ [29, 30].) The source of the electromagnetic shower particles reaching ground level may, to a first approximation, be thought of as a line. Figure 4.7 demonstrates that the total path length differences between particles whose progenitors leave the dense on-axis cascade at the top and bottom of this line source are smaller for showers which occur higher in the atmosphere. This difference in geometric path length translates into increased time dispersion at ground level. Since proton-initiated showers tend to develop deeper in the atmosphere we expect their signal time spread to be, on average, larger than for showers initiated by heavier primaries.

However, in ultra-large ($> 10^{19}$ eV) showers there is measurable signal at very large distances from the shower core ($\geq 1$ km). By reference to figure 4.8 we see that the predicted muonic signal fraction at these distances is significant ($\geq 30\%$). The muons can be much better approximated as having a point source early in the shower development, and this leads to their arriving, at larger core distances, earlier than the electromagnetic particles, and with less time dispersion. The result is a faster rising total signal in showers developing at given atmospheric depth, but having a larger muonic signal fraction.

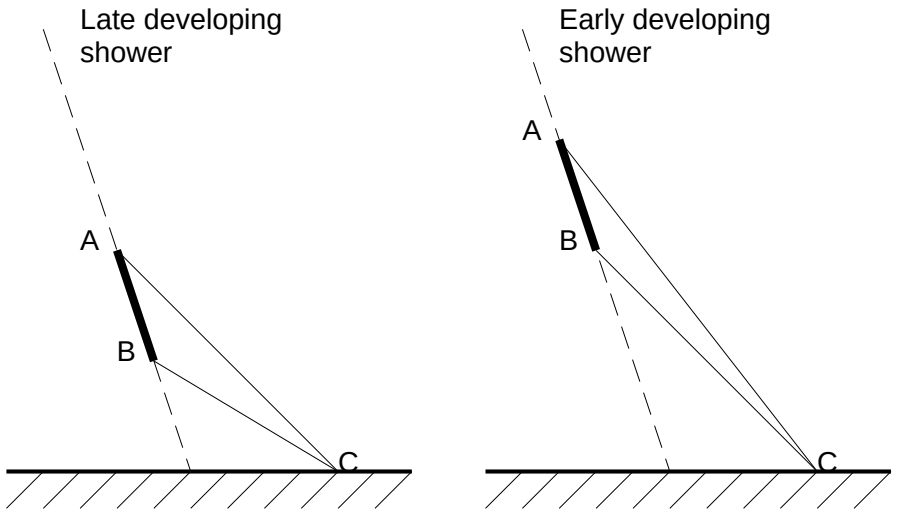


Figure 4.7: *Schematic illustration of the geometric shower front dispersion effect. The shower axis is indicated by a dotted line, the "line-source" of the particles reaching the ground at C being indicated by the bold section AB. Notice that for the late developing case the path length difference ABC − AC is larger than in the early developing case.*

Since muon-rich heavy initiated showers are expected to develop on average higher in the atmosphere the above two effects compound to produce a correlation between the time dispersion of the total observed water Čerenkov signal, and the mass of the shower primary. Figure 4.8 illustrates these effects well, and shows the predicted rise of the integrated total signal. The same simple approximations regarding detector response made in the last section are repeated here.

By examination of figure 4.8 it is possible to see that a major part of the difference in the 10% to 50% rise time between proton and iron-initiated showers comes from the differing muonic to electromagnetic signal ratio, rather than from the geometric effect, as Hillas has been careful to point out [16]. This is an important point — in order to maximize the compositional sensitivity of a rise time parameter it is necessary that the signal contribution from the muonic and electromagnetic

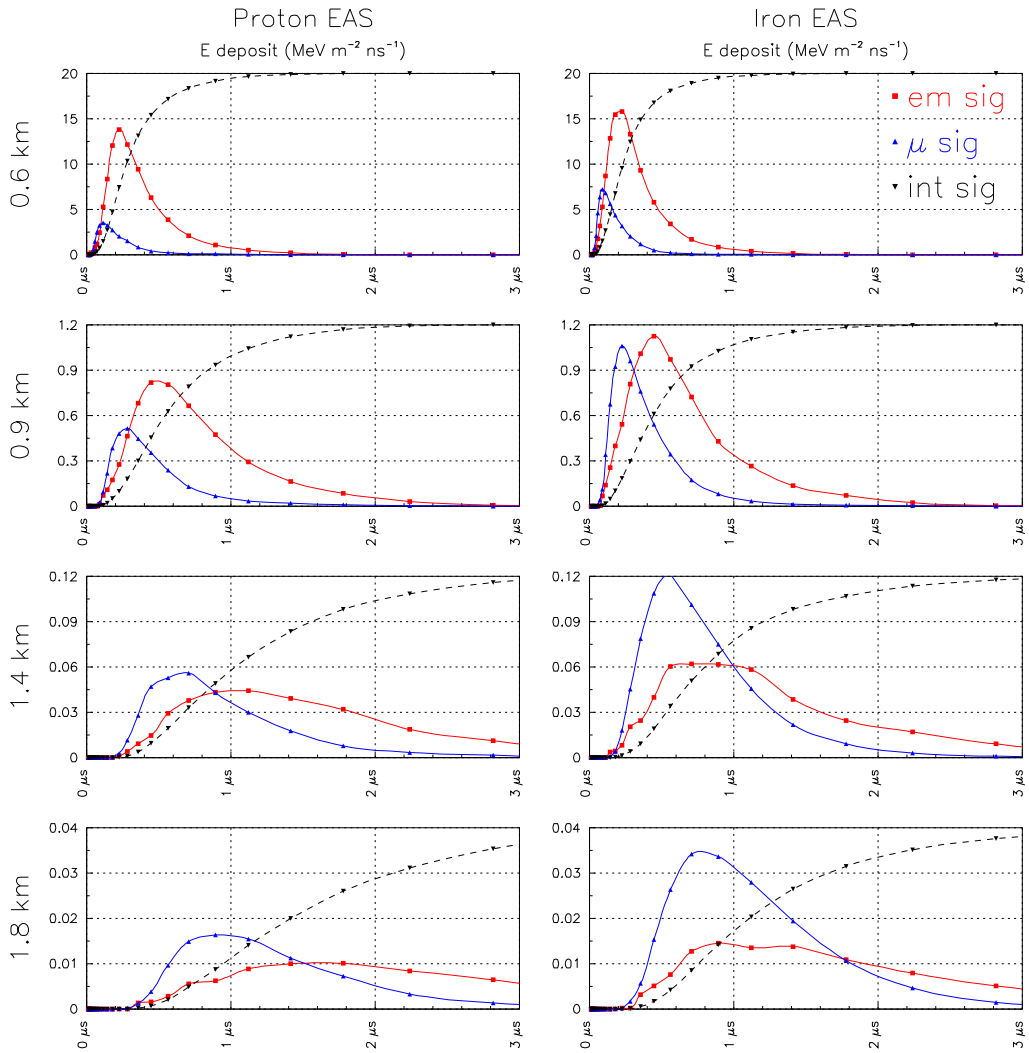


Figure 4.8: *Time profiles of energy deposition into a 1.2 m deep water Čerenkov detector at four distances from the core of a $10^{19}$ eV EAS. Differential energy flow curves are shown for the total electromagnetic signal and the muonic signal; the total signal is shown in the integrated form. The key is the same for each plot and is shown at top right. The shower type and quantity being plotted are indicated at the top of each column, and the core distance to the left of each row. Note that the vertical scale is always 0 to 1 for the total integrated signal curves. (These plots represent the mean of batches of 100 showers each, assuming ground level atmospheric depth of 1000 g cm$^{-2}$.)*

shower components should be similar in magnitude in the core distance range where measurement can be made. For showers of given energy this dictates the optimum atmospheric depth of an array site. For a 1.5 km spaced array observing showers of $10^{19}$ eV we can see from figure 4.6 that an array site significantly higher than 1000 g cm$^{-2}$ would be undesirable. (Referring forward to figure 6.6 note that the increasing separation of the simulated proton and iron-initiated rise times versus core distance with increasing zenith angle is due to the above effect.)

# Chapter 5

## The water Čerenkov technique applied to EAS detection — detector design, simulation and prototype testing

The water Čerenkov technique appears to be the most effective detector type for the ground array system of a next generation (hybrid) EAS detector. It is believed that a suitably designed water tank array can adequately address the physics requirements outlined in section 1.5.1, whilst proving more cost effective than other techniques.

For 20 years a 12 km$^2$ EAS array employing more than 200 water Čerenkov units was operated at Haverah Park in the UK [24]. The experience gained during this experiment provides much useful information in the context of the current discussion, demonstrating that an array based on this technique can operate long term, with both high stability and low maintenance. Haverah Park also provides us with experimental data against which to check the detailed Monte Carlo simulations of ultra-large EAS, which are described in the previous chapter, and on which much of the next generation experimental design must be based. The agreement from the comparisons made thus far is good, and is detailed in the next chapter.

In this chapter the perceived advantages of the water Čerenkov technique are first examined, and the proposed detector and array designs are outlined and discussed. A custom simulation program has been written by the author to model

the interaction of an EAS front with a water Čerenkov detector. This is described in some detail to allow the reader to assess the reliability of its results; the relevant particle interaction processes are detailed including the Čerenkov effect itself. Practical considerations such as material characteristics, PMT positioning, mechanical realization, and water purification are then discussed. Some experimental results from a prototype detector unit are included in these sections. Finally the possible use of wavelength-shifting materials to enhance detector performance is examined.

## 5.1 Advantages of the water Čerenkov technique

At moderate altitudes a surface array observes EAS well past the shower maximum. Sea level is $\approx 1000$ g cm$^{-2}$ while shower maximum for a $1 \times 10^{19}$ eV shower occurs at $\approx 750$ g cm$^{-2}$ (see figure 1.7). Beyond cascade maximum shower attenuation is expected to be approximately exponential, and indeed is observed to be so using the argument that showers of given energy must be observed with equal intensity at increasing zenith angles (and also directly from the Fly's Eye cascade curves). The overall shower is numerically dominated by electromagnetic particles, but at large core distances ($> 500$ m) most of the energy is carried by the muonic component. The electromagnetic component attenuates more rapidly than the muonic component. Hence different types of detector produce different effective attenuation lengths dependent on their relative sensitivities to these two shower components.

For the Haverah Park water Čerenkov array the attenuation coefficient for signal density at 600 m from shower core was shown experimentally to be $760 \pm 40$ g cm$^{-2}$ [8], whilst for the Yakutsk scintillator array a value of $500 \pm 40$ g cm$^{-2}$ was derived [66] (both sites are close to sea level). This effect makes a water

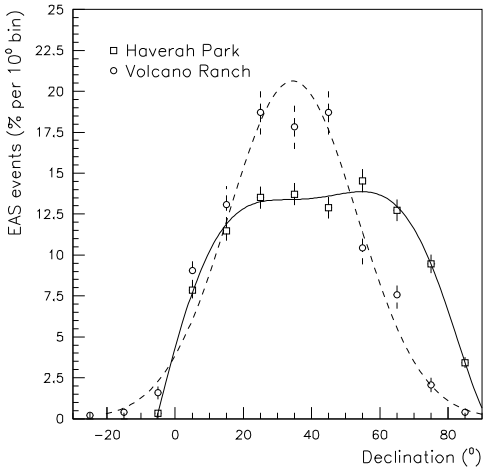


Figure 5.1: *Comparison of the declination distribution of showers recorded by large EAS arrays employing different detector types. The water Čerenkov Haverah Park array was at an atmospheric depth of 1018 g cm$^{-2}$ and latitude of 54° N. The Volcano Ranch scintillator array was at an atmospheric depth of 834 g cm$^{-2}$ and latitude of 35° N. Shower size is in the range $1 \times 10^{18} < E < 4 \times 10^{18}$ eV. Haverah Park data is restricted to zenith angles < 60°, whilst the Volcano Ranch data is for all zenith angles. The FWHM of the Haverah Park distribution is $\approx$ 75° as opposed to $\approx$ 45° for Volcano Ranch — hence the water Čerenkov array has more than twice the solid angle acceptance. This figure is adapted from [17].*

Čerenkov array less sensitive to the atmospheric depth of the site. Also, at a given atmospheric depth, the array energy threshold will rise more slowly with increasing zenith angle providing greater solid angle acceptance at given energy. This results in more collecting power per detector unit, but most importantly, a more uniform sky view in terms of declination angle. Figure 5.1 shows experimental declination distributions from the Haverah Park and Volcano Ranch arrays which illustrate this point.

A secondary advantage of deep ($\geq$ 1 m) water Čerenkov detectors is the large depth to lateral size ratio. This results in the detector projected area falling much more slowly at increasing zenith angles (i.e. the detector projected area in the plane perpendicular to the incident shower axis). Hence statistical sampling fluctuations

due to limited detector area grow much more slowly with zenith angle. Thin detectors of any type are inferior in this respect.

## 5.2 Detector design and array spacing

In its simplest form a water Čerenkov detector can be described as a volume of (clear) water acting as a Čerenkov radiator viewed by one or more sensitive light detectors. In this application the fact that the water also acts as a massive absorber and detector of the very numerous shower gamma rays is very important. Conceptually the proposed design for the ground array unit is a cylindrical volume of water viewed from above by a number of large ($\approx$ 200 mm diameter) photomultiplier tubes (PMTs), the walls of the tank being highly reflective diffusive white surfaces. The reasoning behind this design is made clear in the remainder of this chapter.

The detector area necessary is a function of the array grid spacing, and shower threshold energy desired. Since each station entails many fixed costs independent of detector area (electronics, deployment etc.), and for given array coverage the number of stations required is inversely proportional to the square of the array spacing, it is important that the spacing should be as large as possible to minimize the total system cost. Conversely it is also necessary to collect sufficient information on an event-by-event basis such that direction reconstruction and energy assignment can be carried out with the required accuracies (see section 1.5.1). These conflicting considerations indicate that a grid spacing of 1.5 km is close to optimal for an array intended to measure showers with energy $> 1 \times 10^{19}$ eV. With such a spacing the number of triggered stations will still be large enough ($>$ 15 to 20 units) to make rather over-determined measurements of events at the very highest energies ($\geq 10^{20}$ eV). This is highly desirable due to the rather

controversial nature of shower reconstruction based on distant measurements, and indicates that if a graded array design is selected the spacing should nowhere be greater than 1.5 km.

Once a spacing has been selected the required detector area is dictated by the need to make a statistically useful measurement of the shower front density at core distances of this order. The problem of triggering the detector on the weak signal of a distant EAS in the presence of the very high ground level background rate must also be considered. Again, keeping the total system cost to a minimum dictates that the smallest possible detector be used which will allow the experimental goals to be met. On the basis of these considerations a detector area of $\approx 10$ m$^2$ is probably close to optimal. The requirement that parameters be measurable which are sensitive to the mass of the primary cosmic ray particles also impacts on the detector spacing and area which are required.

The accurate determination of the optimal values for array grid spacing and detector area should rely on full simulations of detector response and triggering, coupled with reconstruction of the event data so generated in a manner identical to that which would be used for real data. This has yet to be carried out in a rigorous manner — the remainder of this thesis is largely the author's contribution to that end.

In all the following a cylindrical detector 1.2 m deep with a radius of 1.8 m has been assumed (top surface area 10.2 m$^2$). The depth is a nominal value selected to allow direct comparison with the existing experimental data from Haverah Park. 1.2 m is $\approx 3.5$ radiation lengths of water, and sufficient to absorb $\approx 85\%$ of the incident electromagnetic shower energy at core distances $> 100$ m. However, a somewhat greater depth ($\approx 2.0$ m) may be preferred to enhance the muonic content information which can be extracted from the PMT output time profiles.

For practical reasons it might be desirable to form each detector station from a number of smaller units, but this may degrade the ability to measure parameters sensitive to primary particle mass. The measurement of total time integrated light yield, and arrival time dispersion is only affected at second order by the lateral size (and shape) of the detector units. However, if it is planned to deduce information regarding the muonic signal fraction from the short, large bursts of light produced by long track length (penetrating) muons, it is important to keep "corner-clipping" effects to a minimum. This implies a detector with as large a lateral size to depth ratio as possible, and hence a single unsegmented unit. However, an internally subdivided single tank, or multiple smaller units placed in physical contact, might work equally well provided the PMT signals are analysed with reference to one another.

A single unsegmented tank is most efficient in terms of the photocathode area required for a given photoelectron yield; i.e. the ratio of photocathode to tank wall area is maximal. The cylindrical shape is desirable as it has inherently uniform response to showers of given zenith angle incident at all azimuthal angles.

## 5.3 Detector simulation

A simple, but very fast, Monte Carlo simulation of the response of a cylindrical or rectangular water Čerenkov detector to incident gamma ray, electron and muon particles has been written. Figure 5.2 is a graphical display illustrating the operation of this program for a detector unit of the proposed size and shape.

The particle interaction modelling is very simple and is taken largely from Rossi [67] and Review of Particle Properties [68] (RPP). The reason that a complete custom program has been written for detector simulation, rather than using

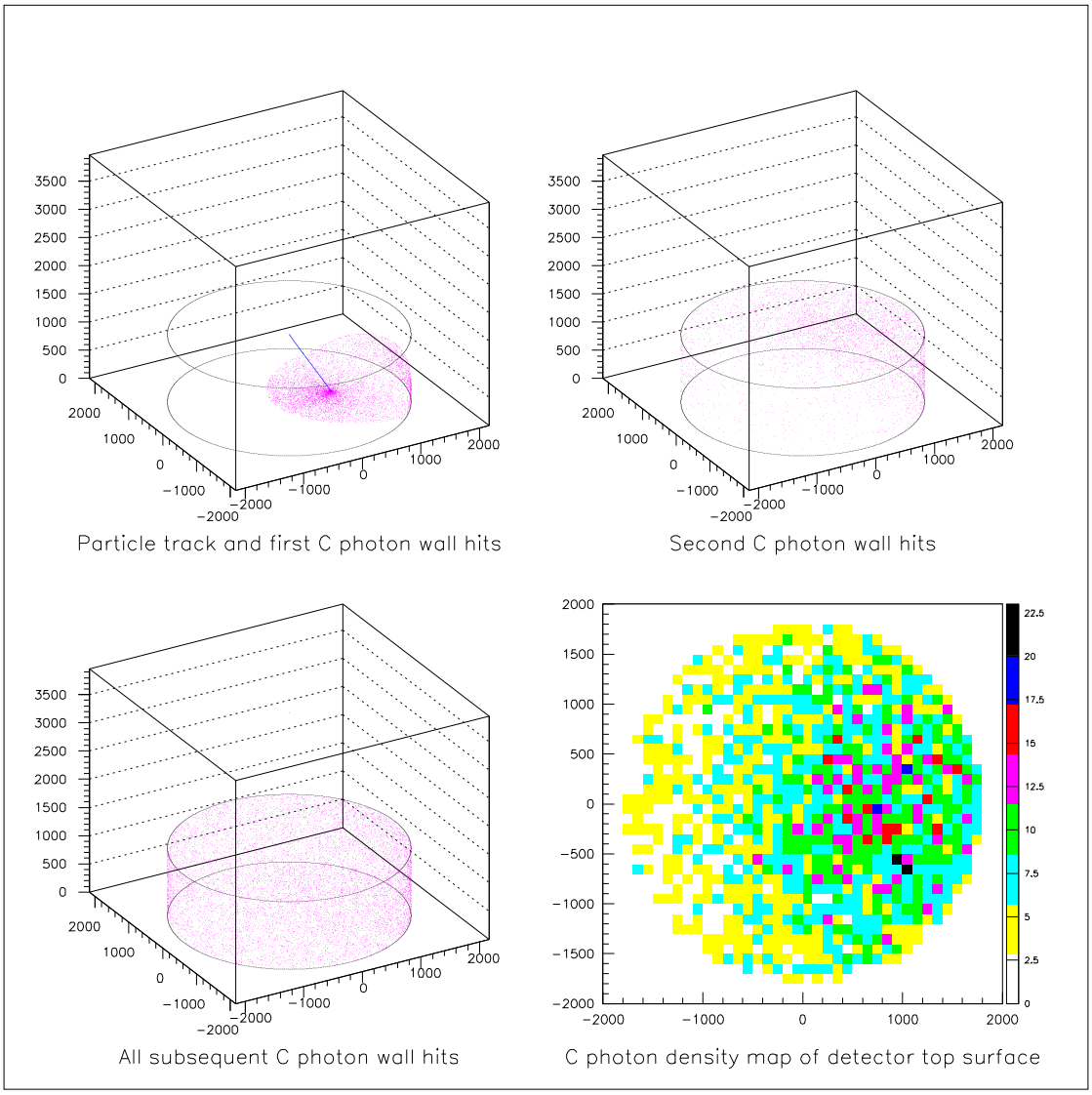


Figure 5.2: *Simulation display for the proposed water Čerenkov detector unit. A single 1 GeV muon was injected at the center of the top surface travelling at 30° to the vertical. The upper left plot shows the incident particle track and the positions where the Čerenkov photons released first reflect from the tank walls. The upper right plot shows the positions of the second photon reflections. Reflections continue until the photons have been absorbed in the water or by the tank lining material; all reflection positions after the second are shown in the lower left plot. The distribution of reflection positions over the detector top surface integrated over all reflections is quite uniform — at lower right a density map of the detector top surface is shown.*

existing codes such as GEANT or EGS4, is simply to obtain very high running speed in the specific application under investigation. The use of this program allows the simulation of complete sets of shower front particles passing into large water Čerenkov detectors. (A vertical $10^{19}$ eV shower front striking a 10 m$^2$ detector at 0.5 km from the core corresponds to a flux of $\approx 20,000$ particles, the bulk being soft gamma rays.) Examination of figure 4.2 indicates that correct treatment of electromagnetic particles in the energy range 1 MeV $< T_{em} <$ 10 GeV is required.

Each injected particle is propagated through a volume larger than the detector volume; this allows for side entry of corner-clipping particles. When outside of the detector propagation is linear at velocity $c$ and no interaction modelling takes place.

### 5.3.1 Gamma rays

The probability for a gamma ray of given energy to interact at each step increment is calculated from a look-up table of mean free path lengths in water. When an interaction occurs the branching ratio to Compton effect or pair production is determined from a second look-up table. This data is displayed in figure 5.3 (taken from RPP figures 11.1 and 11.2).

**Pair production** Pair production is the interaction between an incident gamma ray and the Coulomb field of nuclei; i.e. $\gamma + Z \rightarrow e^+ + e^- + Z$. There is a small additional effect due to interaction in the Coulomb field of atomic electrons. The pair production process is closely analogous to that of bremsstrahlung.

The energy split ratio delivered to the two halves of the electron/positron pair

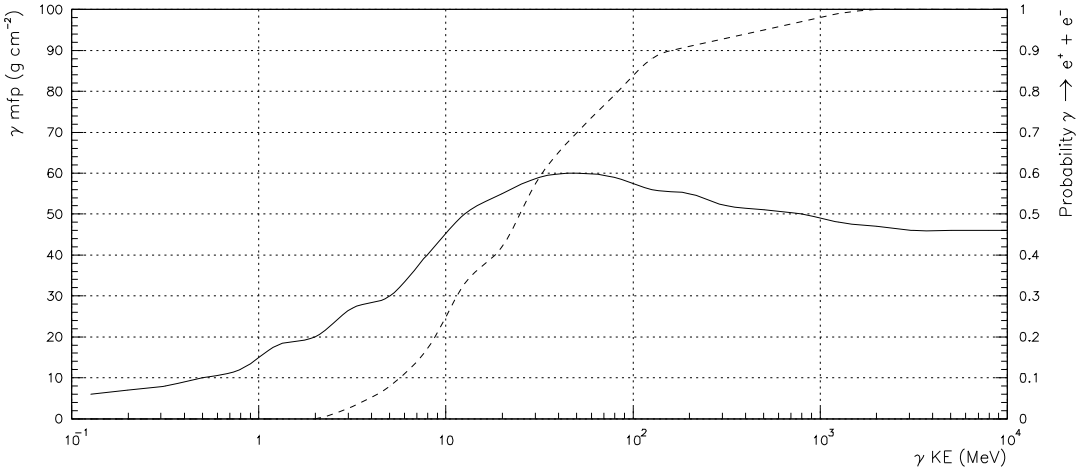


Figure 5.3: *Gamma ray interaction properties in water, as used in detector simulation. The solid line shows mean free path as a function of gamma ray energy. The broken line shows probability that a pair production interaction will occur as opposed to a Compton scatter.*

is determined assuming a flat probability distribution between 0 and 100%; this is an approximation, but close to the truth in the energy range of interest (see Rossi page 82). Since the nucleus acquires a recoil momentum the angles at which the electrons are emitted cannot be uniquely calculated from their energies. It is possible for incident gamma rays of given energy to emit pairs of electrons with the same energy split ratio at different angles on an event-by-event basis. However, the rms angle of emission can be shown to be,

$$\theta_{plane}^{rms} \approx \left(\frac{m_e}{T_\gamma}\right) \ln\left(\frac{T_\gamma}{m_e}\right),$$

where $m_e$ is the electron rest mass energy, and $T_\gamma$ is the incident gamma ray energy (see Rossi page 83)[1]. A single space angle value is sampled on the assumption that the projected (plane) angular distribution has a Gaussian form. This value is used for both of the outgoing particles. In fact multiple scattering leads to deflections

[1]EGS4 makes the approximation that the electron and positron are emitted at a fixed angle $\theta = m_e/T_\gamma$ relative to the incident gamma ray [69].

of the same order after only a few cm so this approximation is unimportant (e.g. $\theta_{plane}^{rms} \approx 1.5°$ for $T_\gamma = 100$ MeV).

**Compton scattering** Compton scattering is an elastic collision between an incident gamma ray and an atomic electron.

Compton scattering is modelled using a simplification of the theoretical result due to Klein and Nishina (see Rossi page 78). The out-going gamma ray energy is selected by sampling from a normalized probability distribution using the rejection method. If the incident gamma ray energy is $T_\gamma$ the relative probability for the outgoing gamma ray energy to be $T'_\gamma$ is approximately,

$$P(T'_\gamma) \propto \frac{1}{T'_\gamma}\left[1 + \left(\frac{T'_\gamma}{T_\gamma}\right)^2\right],$$

and the possible range for the scattered gamma ray energy is $\frac{m_e}{2} < T'_\gamma < T_\gamma$. Note that the probability of the gamma ray leaving the interaction with more than half its incident energy is very small ($< 1\%$).

Since Compton scattering is a 2-body process the angles at which the scattered gamma ray and electron leave the interaction can be computed kinematically:

$$\theta_\gamma = \arccos\left(1 + \frac{m_e}{T_\gamma} - \frac{m_e}{T'_\gamma}\right) \quad \& \quad \theta_e = \arctan\left(\frac{1}{\tan\left(\frac{\theta_\gamma}{2}\right)\left(1 + \frac{T_\gamma}{m_e}\right)}\right).$$

### 5.3.2 Electrons and muons

The processes of ionization energy loss, multiple scattering and Čerenkov light emission are modelled for electrons and muons. Electron bremsstrahlung is also simulated.

**Ionization losses** Charged particles propagating through matter lose energy through Coulomb interactions with atomic electrons. The electrons are raised to excited states or ejected from the atoms entirely. The high energy tail ($E > m_e/2$) of the energy distribution of ejected electrons are referred to as delta rays. (If the incident particle is an electron/positron the process is referred to as Moller/Bhabha scattering.) Note that delta ray production is not treated in the detector simulation code; this is not expected to have any significant impact on the results.

The total ionization energy loss, including the high energy tail, for singly charged particles heavier than electrons is given by the Bethe-Bloch formula,

$$-\frac{dT}{dx} = K\frac{Z}{A}\frac{1}{\beta^2}\left[\ln\left(\frac{2m_e\gamma^2\beta^2}{I}\right) - \beta^2 - \frac{\delta}{2}\right],$$

where $I$ is the mean excitation energy, $\delta$ is the density effect correction, and $K = 4\pi N_A r_e^2 m_e$, where $N_A$ is Avagadro's number, and $r_e$ is the classical electron radius (see RPP section 10.2)[2]. For a compound $Z/A$ is the the number of electrons per molecule over the molecular weight (10/18.02 for water). Calculation of the mean excitation energy $I$ requires a detailed consideration of atomic and molecular structure. However, values are available for common substances; for water $I$ = 75.0 eV. The density effect correction $\delta$ is also highly complex, but values may be computed using the following parameterizations:

$$\begin{aligned} x < x_0 \quad & \delta = 0, \\ x_0 < x < x_1 \quad & \delta = 2\ln(\beta\gamma) + C + a(x_1 - x)^{m_s}, \\ x_1 < x \quad & \delta = 2\ln(\beta\gamma) + C, \end{aligned}$$

where $x = \log(\beta\gamma)$, and the parameters values for water[3] are $a = 0.2065$, $m_s$ =

[2]The expression above is an approximation based on the assumptions that $\beta > Z\alpha$, and $\gamma < M/2m_e$, where $\alpha$ is the fine structure constant, and $M$ is the mass of the incident particle — both valid in the range of interest here.

[3]Values for the mean excitation energy of water $I$, and the parameters and procedure for

3.0070, $x_0 = 0.240$, $x_1 = 2.5$, and $c = -3.502$.

Ionization losses by electrons and positrons are somewhat different. The expressions are:

$$-\frac{dT}{dx} = K\frac{Z}{A}\frac{1}{\beta^2}\left[\frac{B_0(T_e)}{2} - \ln\left(\frac{I}{m_e}\right) - \frac{\delta}{2}\right];$$

where for electrons,

$$B_0(T_e) = \ln\left[\frac{\tau^2(\tau+2)}{2}\right] + \left[\frac{1+\tau^2/8-(2\tau+1)\ln 2}{(\tau+1)^2}\right];$$

and for positrons,

$$B_0(T_e) = \ln\left[\frac{\tau^2(\tau+2)}{2}\right] + 2\ln 2 - \left(\frac{\beta^2}{12}\right)\left[23 + \frac{14}{(\tau+2)} + \frac{10}{(\tau+2)^2} + \frac{4}{(\tau+2)^3}\right];$$

where $\tau = T_e/m_e$ $(= \gamma - 1)$. $K$, $I$ and $\delta$ are the same as in the heavy particle case above[4].

The above information is used by the simulation code at run start to generate a look-up table of the mean ionization loss per g cm$^{-2}$ of water traversed for electrons and muons. A 50:50 mix of positrons and electrons is assumed. The results from these calculations are shown in figure 5.4.

calculating the density effect correction $\delta$ are taken from the EGS4 manual [69, section 2.13].

[4]These expressions are taken from Seltzer and Berger [70]. However Rossi (page 27) quotes the formula,

$$-\frac{dT}{dx} = K\frac{Z}{A}\frac{1}{\beta^2}\left[\ln\left(\frac{\pi m_e \gamma^{3/2}}{I}\right) - a - \frac{\delta}{2}\right],$$

where $a = 2.9$ for electrons, and $a = 3.6$ for positrons. This formula yields results which differ significantly from the more complex formulae above only at $T_e < 1$ MeV. Since in the high energy limit $\delta/2 \propto \ln\gamma$, the Rossi form makes the differing slopes of the relativistic rise in energy loss rate for electrons and muons more readily understandable.

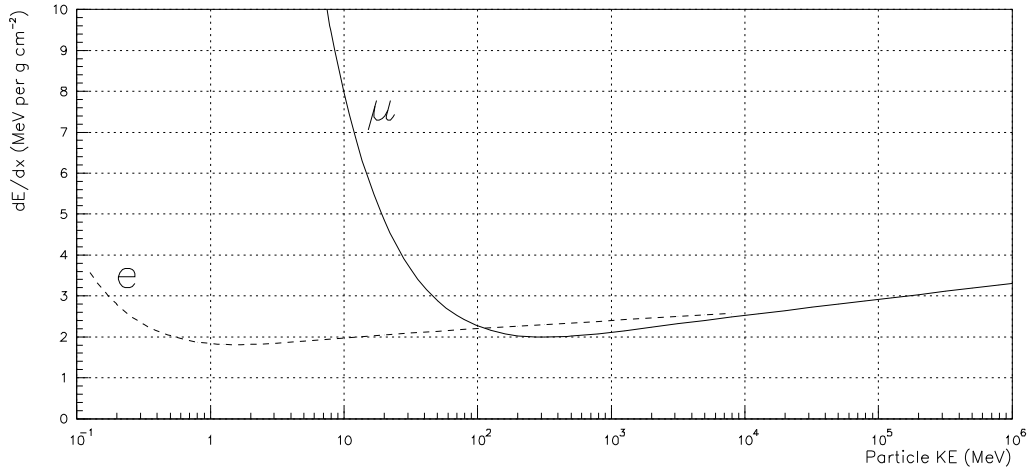


Figure 5.4: *Ionization loss characteristics in water, as used in detector simulation. The solid curve shows the mean ionization loss per g cm$^{-2}$ of water traversed for muons, and the broken curve the same for an equal mix of electrons and positrons.*

The minimum energy down to which it is useful to follow particles is related to the track increment step size $\Delta x$. This step size must be chosen on the basis of a trade off between accuracy (small steps), and fast running speed (large steps). For all the results presented here $\Delta x$ was set to 5 mm. The cutoff energy below which particles are rejected is set to $\frac{dT}{dx}_{min}\frac{\Delta x}{2}$. Hence particles are followed until $T < 0.5$ MeV, and since the rate of Čerenkov emission at these energies is rapidly cutting off, this limitation will not have a significant impact.

**Multiple scattering** Charged particles propagating through matter are subject to deflection by many small angle scatterings. The bulk of this deflection is due to interactions with the Coulomb fields of nuclei. This is modelled by deflecting the particle through a small space angle at each track increment step. The projected rms deflection angle $\theta^{rms}_{plane}$ is calculated using the approximation,

$$\theta^{rms}_{plane} \approx \frac{13.6MeV}{\beta cp}\sqrt{\frac{\Delta x}{X_0}}\left[1 + 0.038\ln\left(\frac{\Delta x}{X_0}\right)\right],$$

where $\beta c$ and $p$ are the velocity and momentum of the particle, and $\Delta x/X_0$ is the length of the track increment in units of radiation length; for water $X_0 =$ 36.1 cm (see RPP section 10.6). A space angle scattering value is sampled on the assumption that the projected (plane) angular distribution has a Gaussian form. This approximation is good for the central 98% of the true distribution, but underestimates the number of larger angle scatters ($\theta_{space} >$ several $\theta^{rms}_{space}$). (Hence hard scattering is underestimated in the simulation code, and this might have some effect on electromagnetic/muonic signal separation — see section 5.4.)

**Bremsstrahlung** Bremsstrahlung is the interaction between an incident charged particle and the Coulomb field of a nucleus through which it passes; e.g. $e + Z \rightarrow e + Z + \gamma$. There is a small additional effect due to radiation in the Coulomb field of atomic electrons. The bremsstrahlung process is closely analogous to that of pair production.

Since suitable published data could not be located, (as was the case for pair production), electron bremsstrahlung is modelled using theory given by Rossi (page 48). (The effect of radiative processes on muons is insignificant at energies $<$ 100 GeV, and can safely be ignored.) If the total incident electron energy is $E_e$, ($E_e = T_e + m_e$), then the screening influence of the atomic electrons is determined by the quantity,

$$\gamma = 100 \frac{m_e}{E_e} \frac{\nu}{1-\nu} Z^{-1/3},$$

where $\nu$ is the fraction of the total incident electron energy $E_e$ which is transferred to the outgoing gamma ray ($\nu = T'_\gamma / E_e$).

When $E_e \gg m_e$ the expressions for $\Phi(E_e, \nu)d\nu$, the differential radiation probability per g cm$^{-2}$ of material traversed, are as follows:

no screening, $\gamma \gg 1$

$$\Phi(E_e,\nu)d\nu = k\frac{d\nu}{\nu}\left[1+(1-\nu)^2-\frac{2}{3}(1-\nu)\right]\left[\ln\left(\frac{2E_e}{m_e}\frac{1-\nu}{\nu}\right)-\frac{1}{2}\right];$$

complete screening, $\gamma \approx 0$

$$\Phi(E_e,\nu)d\nu = k\frac{d\nu}{\nu}\left\{\left[1+(1-\nu)^2-\frac{2}{3}(1-\nu)\right]\ln(183Z^{-1/3})+\frac{1}{9}(1-\nu)\right\};$$

intermediate cases,

$\gamma < 2$

$$\Phi(E_e,\nu)d\nu = k\frac{d\nu}{\nu}\left\{\left[1+(1-\nu)^2\right]\left[\frac{f_1(\gamma)}{4}-\frac{1}{3}\ln Z\right]-\frac{2}{3}(1-\nu)\left[\frac{f_2(\gamma)}{4}-\frac{1}{3}\ln Z\right]\right\};$$

$2 < \gamma < 15$

$$\Phi(E_e,\nu)d\nu = k\frac{d\nu}{\nu}\left[1+(1-\nu)^2-\frac{2}{3}(1-\nu)\right]\left[\ln\left(\frac{2E_e}{m_e}\frac{1-\nu}{\nu}\right)-\frac{1}{2}-c(\gamma)^{-1/2}\right];$$

where in each case,

$$k = 4\alpha\frac{N}{A}(Z^2+Z)r_0^2.$$

Note that the term $(Z^2+Z)$ in the expression for $k$ takes account of bremsstrahlung interactions which occur in the Coulomb field of atomic electrons, in addition to those in the nuclear field (see Rossi page 54).

Rossi presents $f_1(\gamma)$, $f_2(\gamma)$ and $c(\gamma)$ in graphical form. To facilitate computation these functions can be approximated by the following expressions:

$$
\begin{aligned}
0 < \gamma < 0.8 \quad f_1(\gamma) &= -3.52\gamma + 20.79, \\
f_2(\gamma) &= -2.86\gamma + 20.29; \\
0.8 < \gamma < 2 \quad f_1(\gamma) &= f_2(\gamma) = -1.91\gamma + 19.40; \\
2 < \gamma < 15 \quad c(\gamma) &= 0.5\exp(-0.45\gamma) + 0.01.
\end{aligned}
$$

Since the above expressions are derived under the assumption that $T_e \gg m_e$ the results are increasingly approximate for $T_e < 10$ MeV. However, referring to figure 4.2, note that the shower simulation prediction is that the bulk of the electromagnetic energy flux is carried by particles with $T > 10$ MeV. Hence this limitation is not expected to have a significant impact.

The above expressions are used by the simulation code at run start to generate a 2-d look-up table of the differential probability of a bremsstrahlung interaction per g cm$^{-2}$ of water traversed for electrons of various energies. The calculation is performed separately for hydrogen and oxygen, and a weighted mean of the results taken according to the mass ratio of the water molecule (2:16). Values are tabulated for each percentage transfer of the initial electron kinetic energy $T_e$ from 1% to 99%, at five values of $T_e$ per decade. A very small fraction of the energy loss via bremsstrahlung goes into gamma rays having $< 1\%$ of the incident electron energy (see Rossi page 51). The resulting table is then numerically integrated, the total probability of an interaction per g cm$^{-2}$ recorded, and the table normalized to represent relative energy transfer probability. Some results from this process are displayed in figure 5.5.

Since the nucleus acquires a recoil momentum in a bremsstrahlung interaction the angles at which the incident electron, and the product gamma ray, leave the the interaction are not uniquely determined by the fractional energy transfer. It is possible for an electron of given energy to emit gamma rays of the same energy at different angles. However, the rms angle at which the gamma ray is emitted can

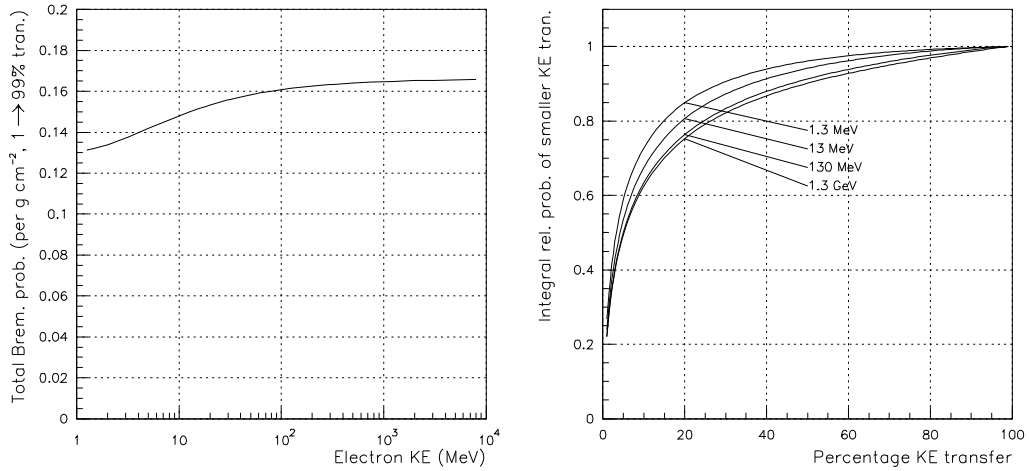


Figure 5.5: *Electron bremsstrahlung interaction properties in water, as used in detector simulation. The left plot shows the total probability per g cm$^{-2}$ of a bremsstrahlung interaction taking place which transfers between 1% and 99% of the incident electron kinetic energy to a gamma ray. The right plot shows the integral relative probability that a percentage transfer smaller than a given value results.*

be shown to be,

$$\theta_{plane}^{rms} \approx \left(\frac{m_e}{E_e}\right) \ln\left(\frac{E_e}{m_e}\right),$$

where the symbols are as above (see Rossi page 53)[5]. A single space angle value is sampled on the assumption that the projected (plane) angular distribution has a Gaussian form. The incident electron is assumed to be undeflected. In fact electron multiple scattering leads to deflections of the same order after only a few cm so these approximations are unimportant (e.g. $\theta_{plane}^{rms} \approx 1.5°$ for $E_e = 100$ MeV).

**Čerenkov radiation** Čerenkov light is produced by a charged particle moving through a transparent medium with velocity $\beta \geq 1/n$, where $n$ is the refractive

[5]EGS4 makes the approximation that the the product gamma ray is emitted at a fixed angle $\theta = m_e/E_e$ relative to the electron trajectory [69].

index. In water $n = 1.33$ and a particle must have kinetic energy of greater than half its rest mass energy to radiate Čerenkov light (0.25 MeV for electrons and 53 MeV for muons). The angle of emission is $\theta = \cos^{-1}(1/\beta n)$ with respect to the particle trajectory; 42° for a fully relativistic particle in water.

The yield of Čerenkov photons $N$ for a small element of particle track $\Delta x$ meters is given by the following equation,

$$N = 2\pi\alpha\Delta x \left(\frac{1}{\lambda_1} - \frac{1}{\lambda_2}\right)\left(1 - \frac{1}{\beta^2 n^2}\right),$$

where $\alpha$ is the fine structure constant, and $\lambda_1$ and $\lambda_2$ are the lower and upper wavelength integration limits [71]. When kinetic energy is equal to rest mass energy ($\beta = 0.86$) the rate of Čerenkov radiation is $\approx 80\%$ of maximum. Figure 5.6 shows the total rate of emission, and the emission angle, as a function of particle energy for electrons and muons. Figure 5.7 shows the Čerenkov emission spectrum in water, together with some other spectral distributions which are important, and which are discussed in the next section.

In the detector simulation code a full ray-tracing approach is employed. The above expressions are used to calculate the light yield for each track increment step, and also the emission angle. Each Čerenkov photon is then followed as it passes through the water, reflecting from the tank walls, until it is absorbed or reaches a photomultiplier tube. Hence the output from the detector simulation program is a simple list of photoelectron release times.

### 5.3.3 Material characteristics

If the detector simulation code is to be realistic information is required about the spectral characteristics of the light transmission, reflection and detection processes.

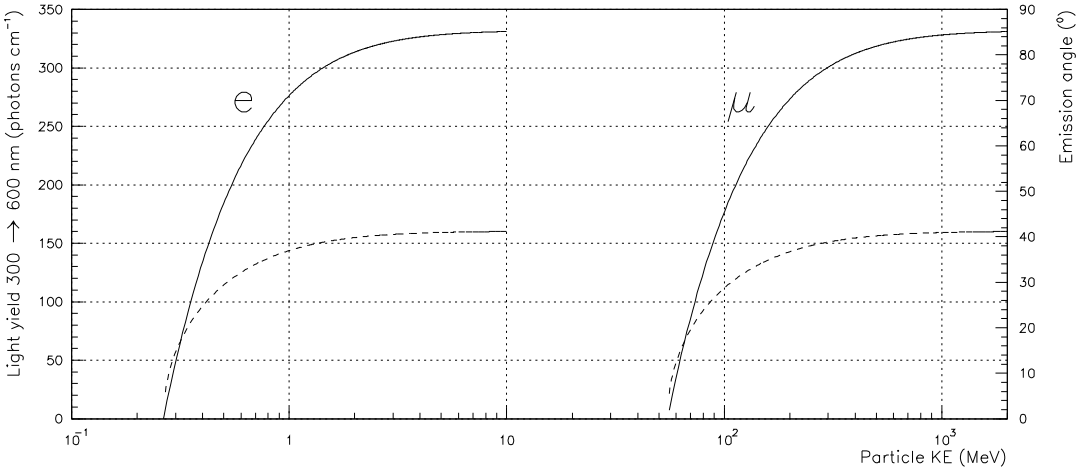


Figure 5.6: *Čerenkov emission characteristics for muons and electrons in water, as used in detector simulation. The solid line shows emission rate integrated between 300 and 600 nm. The broken line shows angle of emission relative to the particle trajectory.*

In figure 5.7 the Čerenkov emission spectrum and PMT quantum efficiency (detection) curves are shown. These are well known quantities; their convolution is also shown. Clearly the wavelength region between 300 and 500 nm is crucially important. The spectral diffuse reflectivity of a material called Tyvec is shown, it being the best potential lining material identified so far (but see section 5.6). Finally the absorption length of ultra-pure laboratory water is shown, and is seen to be $\geq 10$ m across the wavelength range of interest[6]. However the spectral characteristic of water containing particulate impurity is a function of the numerical density, size spectrum, and composition of the impurity particles. Values much below the ultra-pure curve shown are expected for water whose quality is practical for this

[6]The quantum efficiency curve is taken from the data sheet of the Hamamatsu R1408 PMT, a hemispherical tube 200 mm in diameter, having a bialkali photocathode and a borosilicate glass envelope (used in the IMB experiment).

The reflectivity curve for Tyvec shown is for light incident at 30° to the normal; however the angular dependence is small. These measurements were made by Surface Optics Corporation for UCI School of Physical Sciences.

The ultra-pure water absorption length curve is taken from a 1981 review of the available data [72].

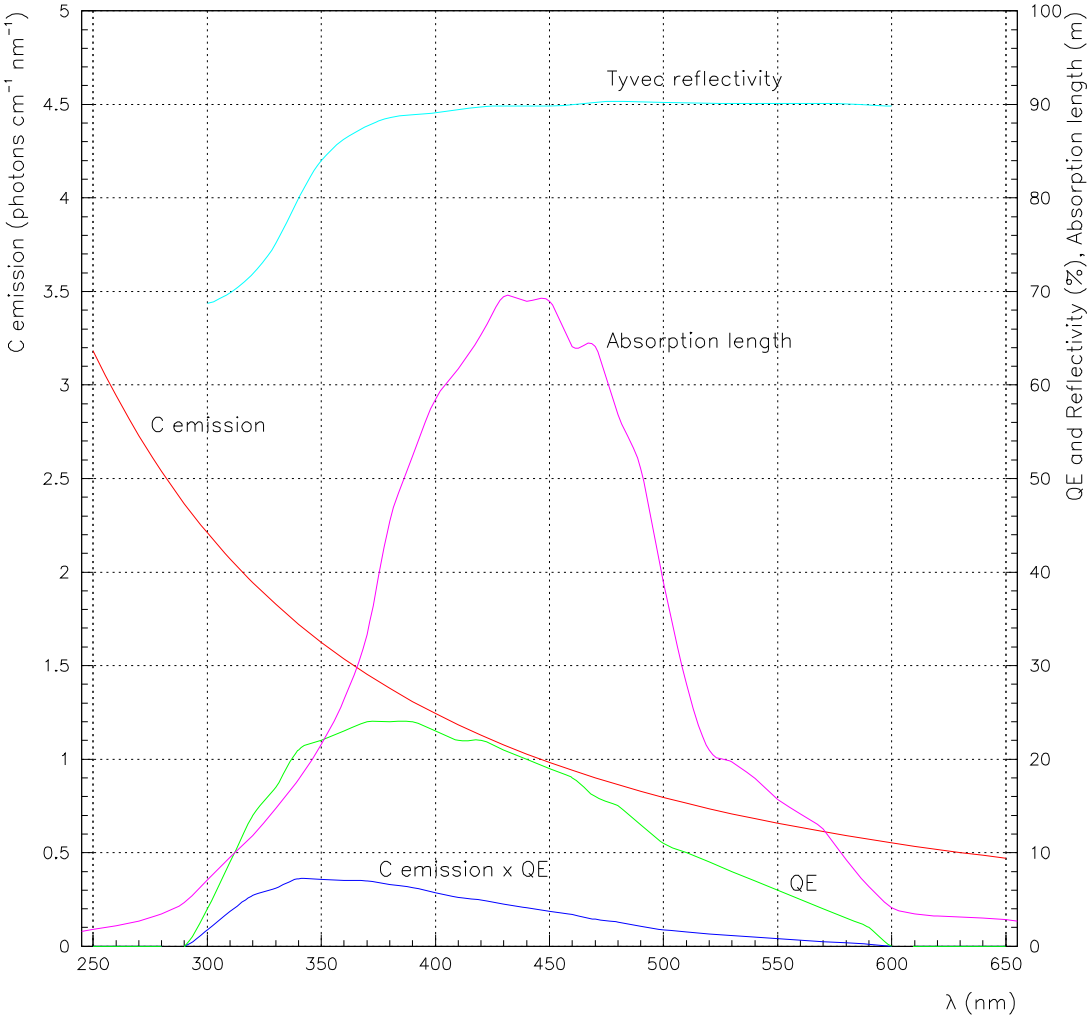


Figure 5.7: *Some important spectral characteristics for a water Čerenkov detector. Quantum efficiency shown is for a bialkali photocathode. Absorption length is for ultra-pure water. Tyvec is a fibrous plastic sheet material often used for wrapping scintillator detectors. See section 5.3.3 for further details.*

application. Behaviour varies greatly depending on the source and purification processing of a particular water sample (see section 5.7 for further discussion, and some preliminary measurements).

In the absence of good data on the absorption length of specific water samples, spectral effects have not so far been explicitly included in the simulation code by assigning each Čerenkov photon released a wavelength sampled from the emission spectrum. Instead, and also to speed up the simulation process, the number of Čerenkov photons emitted for each particle track increment is set to the integral of the convolution of the emission and detection characteristics, and fixed water absorption length and lining material reflectivity are assumed. The validity of these approximations depends upon the extent to which the true values vary over the spectral range of interest (300 to 500 nm), in combination with the size and geometry of the detector. Further work on these points is clearly required.

Approximations regarding the physical parameters of materials made for the purposes of simulation are listed below. These numbers represent effective values over the range 300 to 500 nm, and are believed to be realistically achievable:

- 15% effective photocathode quantum efficiency (when convolved with the Čerenkov emission spectrum).
- 85% reflectivity of the tank lining material.
- 7 m water absorption length.
- 10% : 90% split between perfectly specular and perfectly diffuse reflection behaviour for photons reflected from the lining material. (In fact the split ratio assumed has little effect on the results.)

It should be emphasized that to a very good approximation the parameter values

assumed affect only the absolute photoelectron yield for a given incident particle. They do not affect the validity of the comparisons with experimental data detailed in the next chapter, where simulated detector calibration has been carried out.

## 5.4 PMT selection, positioning and detector proportionality

In terms of photocathode area per unit cost 200 mm diameter PMTs are probably most efficient. The detector simulation code described in the previous section has been used to investigate the number of such tubes required, and their optimal positioning, for the proposed 10 $m^2 \times 1.2$ m deep unit. With the assumed material parameters listed above 3 PMTs give a mean total yield of $\approx 50$ photoelectrons in response to a vertical through-going muon, which probably results in acceptable Poisson fluctuations. The assumptions are thought to be realistic/conservative and this number therefore should be a lower limit.

For a deep detector such as is being considered here the usual concept of uniformity can be misleading. At non-vertical angles of incidence penetrating particles will have a spread of in-detector track lengths due to the corner-clipping effect. The best that can be asked of a deep Čerenkov detector is that the output signal amplitude should be closely *proportional* to the amount of light released into the detector volume, and hence, to a good approximation, to the energy deposition. The basic measurement of total time integrated light yield at large core distances demands a reasonable degree of proportionality. (At 0.9 km from a $10^{19}$ eV EAS the muon density is $\approx 1$ $m^{-2}$, which already results in large Poisson fluctuations when using a 10 $m^2$ unit — further degradation is undesirable.) However, the proposal to directly measure the muonic signal fraction by exploiting the short, large bursts of light produced demands proportionality on a particle-by-particle basis, and is a considerably more stringent constraint.

Also, if this technique is to be successful it is necessary that the decay time of each muon pulse should be fast enough that pile-up effects are controlled. Hence even if very long water attenuation lengths and high lining material reflectivity were to be feasible, they would probably not be desirable. The requirement for prompt light dictates a minimum acceptable photocathode to tank wall area ratio, regardless of attenuation length and reflectivity.

The simulation indicates that good proportionality between Čerenkov light released and photoelectron yield is obtained when the 3 PMTs are placed at 120° spacing on a circle of radius 1.2 m (2/3 of the detector radius). To maintain proportionality it is vitally important to avoid direct Čerenkov radiation onto the photocathode. Figure 5.8 illustrates this point clearly.

Even with the PMTs on the top surface direct irradiation of the photocathode can still occur when a particle travels through the tank at $> 48°$ zenith angle (since the angle of Čerenkov emission in water is $\leq 42°$). Use of plane faced PMTs would completely suppress direct radiation right up to the maximum 48° angle between particle trajectory and the zenith, and hence would be preferable to the more usual hemispherical designs. Near-isotropic decay of muons which stop in the detector volume is an unavoidable source of direct photocathode irradiation.

It should be noted that the shower particles arrive with a large spread of angles relative to the shower axis. However, the high energy particles which produce significant Čerenkov radiant track lengths have a much smaller spread of angles. (Preliminary investigation of the shower simulation predictions indicate that particles with energy $> 10$ MeV have median space angle deviation of $< 20°$ relative to the shower axis.) Particles do not scatter significantly away from their incident trajectory while passing through the water until the last few cm of the track where little or no Čerenkov radiation is produced. However, further investigation of this point is required.

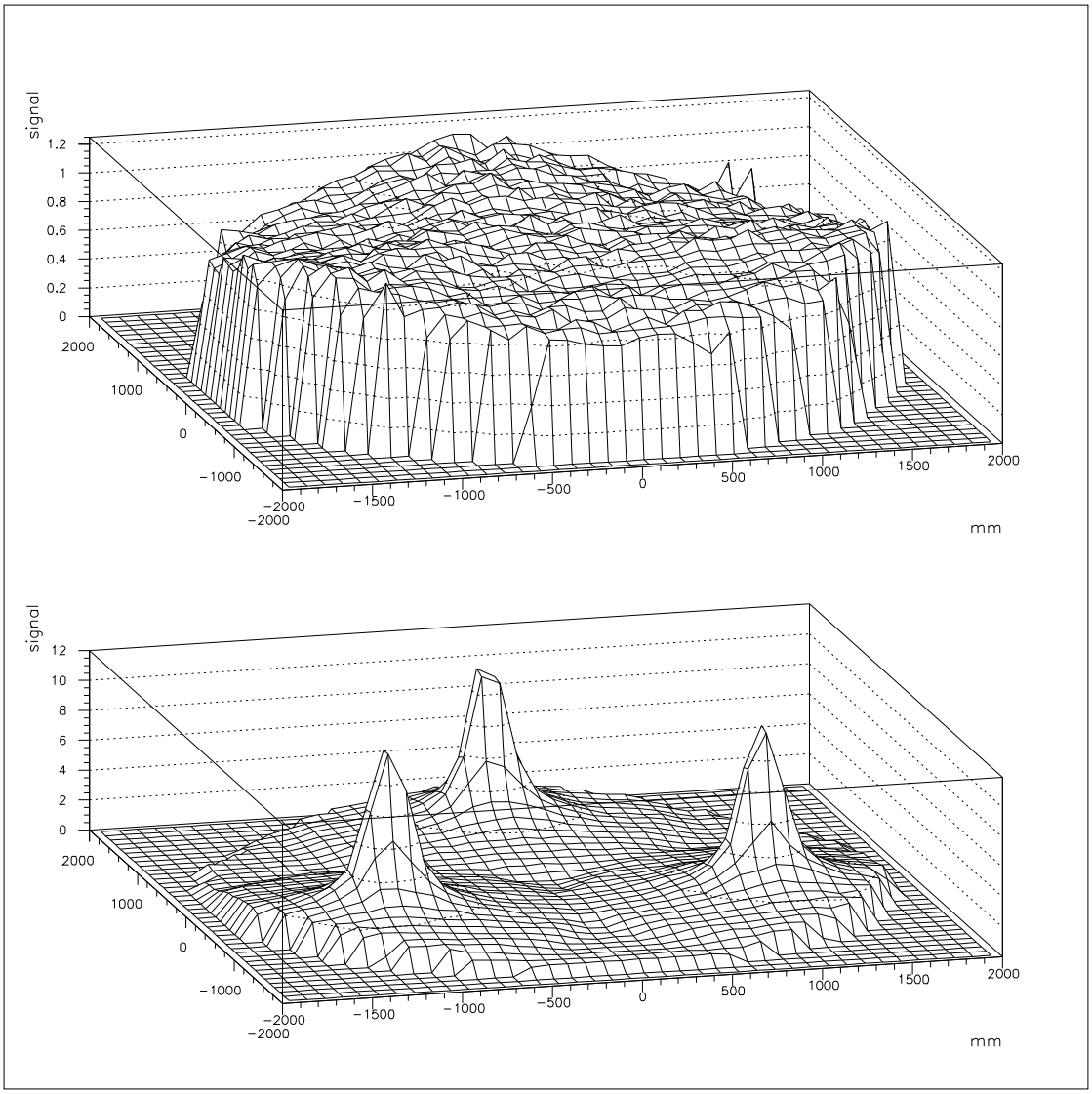


Figure 5.8: *Simulated non-proportionality plot for the proposed water Čerenkov detector unit. The upper plot shows response with PMTs placed at the top looking down, and the lower plot is identical with the PMTs at the bottom looking up. Many 1 GeV muons were injected vertically at random positions over the detector top surface, and the resulting photoelectron yields averaged in 10 cm square bins. The vertical axis scales are relative to the overall mean signal in the down looking case.*

Note that the the effect of Čerenkov radiation in the glass of the PMT face has yet to be simulated. Minimization of this effect is a secondary reason for positioning the PMTs downward looking and in direct contact with the water. Due to the similar refractive indexes of glass ($n \approx 1.5$) and water ($n \approx 1.3$) some portion of the Čerenkov light radiated in the PMT face will escape into the detector volume, rather than being reflected back onto the photocathode[7]. If the refractive index of the water can be made more equal to the PMT envelope glass, for example by use of potassium chloride as a solute, this effect can be further suppressed.

Tests on a cylindrical 6.6 $m^2 \times 1.2$ m deep prototype tank constructed at FNAL are qualitatively consistent with the simulation shown in figure 5.8, although conditions were not identical. The prototype tank had 4 Hamamatsu R1408 200 mm diameter PMTs arranged in a circle with diameter 2/3 that of the detector. Using a 4-paddle scintillator telescope trigger the analogue sum of the signals from all 4 tubes was recorded for muons penetrating the tank vertically. The charge distributions derived from sets of several thousand events at 3 positions are shown in figure 5.9. It is thought that the large high side tail of the "above-tube" distribution is due to the sub-set of muons which pass through the tube itself (note that the PMTs used were hemispherical).

## 5.5 Simulation of PMT output

The detector simulation code output is a simple list of photoelectron release times for each injected particle. These may be used to construct the time/amplitude signal profile which would be observed from the PMTs using a few simple ap-

[7]The Čerenkov emission angle for a $n = 1.5$ medium is $\approx 48°$. For a vertical particle, and a plane faced PMT only $\approx 4\%$ of the incident light will be reflected back at a $n = 1.5$ to $n = 1.3$ interface. However, the total internal reflection angle for such an interface is $\approx 60°$ so at particle zenith angles of $> 12°$ an increasingly serious problem starts to arise

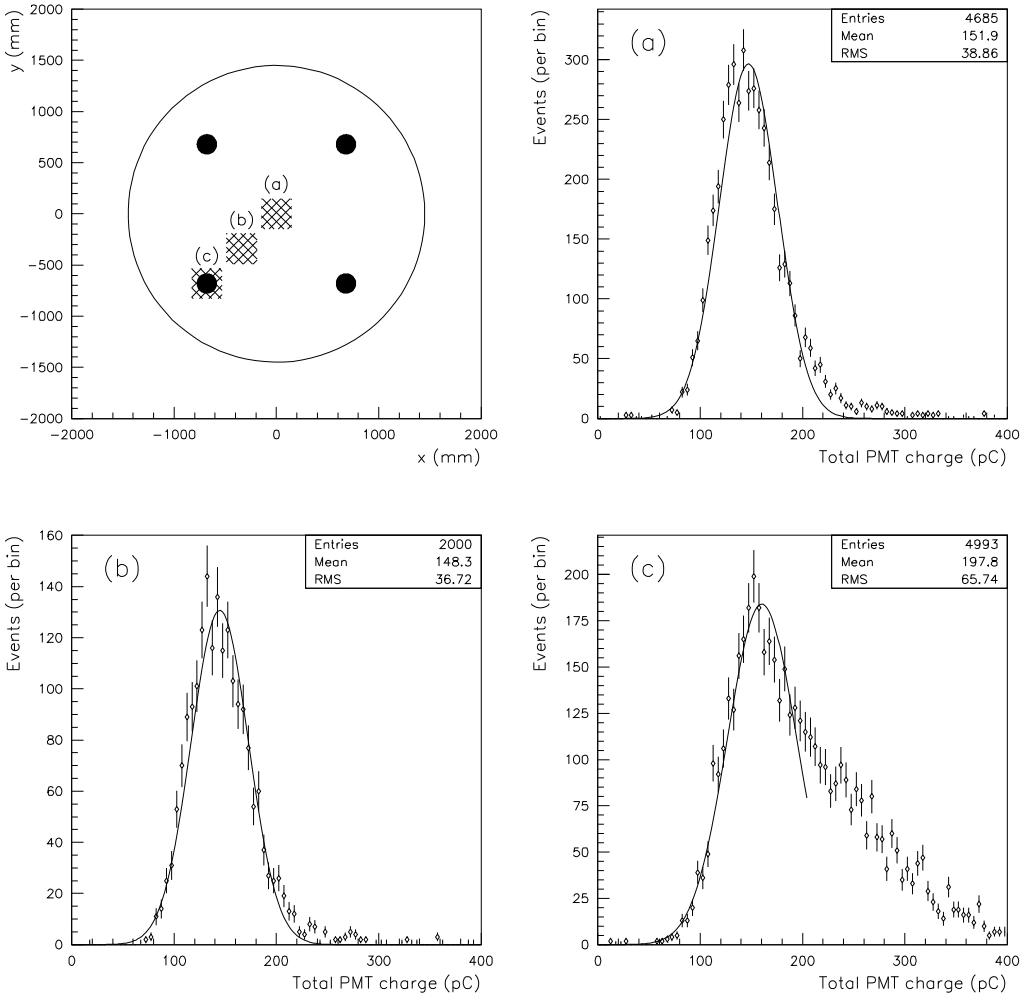


Figure 5.9: *Test results from a cylindrical 6.6 $m^2 \times 1.2$ m deep prototype water Čerenkov tank. The top left plot is a diagram of the detector top surface showing the positions of the 4 PMTs and also where the 3 calibration runs labeled (a), (b) and (c) were taken. (Scintillator paddles were placed above and below the tank to trigger on vertical through-going muons.) The charge distributions shown are the analogue sum of the signals from all 4 tubes. The high side tail of plot (c) is due to muons which pass through the tube itself.*

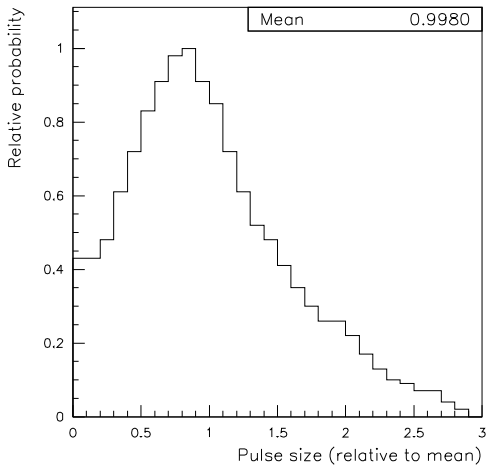


Figure 5.10: *Single-electron spectrum assumed for the purposes of PMT output simulation.*

proximations. For each photoelectron a small Gaussian shaped pulse with a fixed FWHM is added to the aggregate time profile. The pulse width assumed in this work is 12 ns which is similar to the performance of good current 200 mm diameter PMTs[8].

The amplitude of each photoelectron pulse is sampled from a distribution to reflect the single-electron spectrum characteristics of a real tube. Figure 5.10 shows the distribution which has been assumed in this work[9]. Fluctuations in the multiplication occurring at the first dynode are the major cause of this effect. Note that there is always a large proportion ($\approx 10\%$) of very small pulses ($< 1/3$ of the mean); these are real signal pulses caused by photoelectrons being inelastically back-scattered at the first dynode [73].

In all of the work presented here the signals from the (3) PMTs are assumed

[8]The 12 ns value refers to the width of the current pulse arriving at the PMT anode. It does not refer to the more often quoted transit time jitter, which for recent tube designs is $< 2$ ns, and which is assumed to be zero in the simulation presented here.

[9]The single-electron amplitude spectrum shown was inferred from curves given by the Hamamatsu R1408 data sheet. Note that large PMTs have relatively poor characteristics in this respect due to the inevitably large range of photoelectron incidence angles at the first dynode.

to be summed together and passed to a fast transient capture system. (Hence the PMTs are assumed to have equal transit times and to be set to exactly equal gains. Fluctuations in PMT transit times are also not currently considered.) Practical transient capture systems have 2 relevant limitations:

- Limited dynamic range — current fast FADC devices offer $\leq 8$ bit resolution.
- Limited time resolution.

In addition FADCs perform "epoch" sampling — the output code represents the near-instantaneous input voltage relative to the device clock signal. This is an advantage in many applications, but a disadvantage for fast PMT signal capture where, in addition to the pulse shape, the integrated pulse amplitude is also of interest. However, it may be possible to design a "time-slice integrating" front end circuit to overcome this limitation. In the following work a 200 MSPS 8 bit transient capture system is assumed, this being the fastest sample rate which can be contemplated using current technology when taking into account the stringent limitations of unit cost and power consumption imposed by the overall project constraints. If it is found that effective muonic signal separation is not possible even at this very high sample speed then reconsideration of the experimental approach will be required. Conversely it might be possible to reduce the simulated sample rate without degrading the predicted performance.

At this stage of the simulation development it is instructive to view the predicted detector output profile in response to particles of several types and energies; see figure 5.11. Note that peak pulse height correlates rather poorly with the number of photoelectrons released.

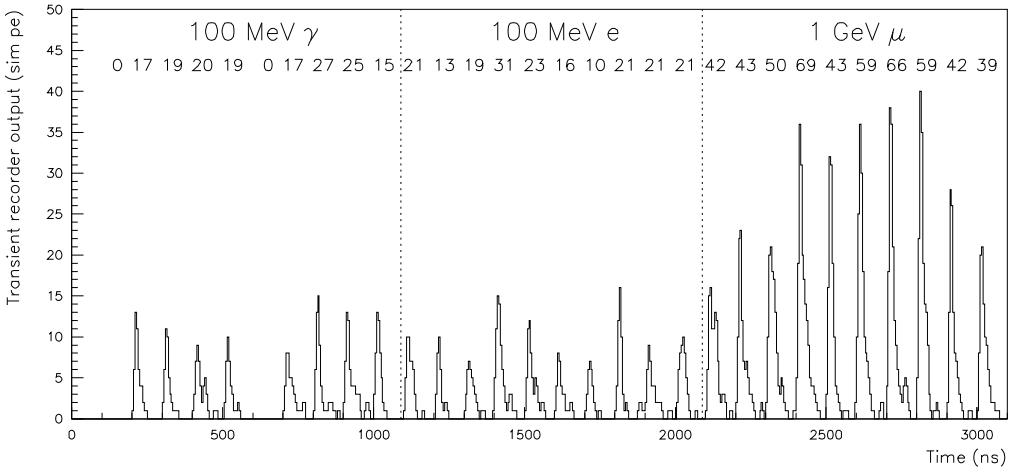


Figure 5.11: *Example of simulated detector output. 100 MeV Gamma and electron, and 1 GeV muon particles (10 of each) have been injected at 100 ns intervals. The number of photoelectrons released by each particle is indicated. The pulse profiles shown assume a 200 MSPS transient capture system with an 8 bit dynamic range where gain is set such that the mean pulse height from a single photoelectron corresponds to 1 output count. Each particle was injected vertically at random coordinates on the detector top surface.*

## 5.6 Mechanical realization

The Haverah Park detectors were made from galvanized iron tanks of rectangular cross section (1.85 m $\times$ 1.24 m $\times$ 1.29 m high); the tanks were filled to a depth of 1.2 m. The walls (sides, top and bottom) were lined with a white diffusive PVC material supplied by ICI under the commercial name "Darvic". The side and top sheets were suspended from pins welded near the top of each vertical side. The tanks were air tight and opened only to replace defective photomultiplier tubes (on average once every five years). A single 100 mm diameter plane faced PMT was positioned in the center of the top surface viewing vertically down with the face dipped into the water. Only two tanks were re-filled during the entire 20 year run of the experiment, and loss of performance over this time was $< 10\%$. A total of 225 tank units as described above were deployed in clusters of up to 34 m$^2$ total

top surface area, each cluster being housed in a heated, concrete floored hut of wooden construction.

For the next generation ground array a detector unit is required which can withstand a harsh desert environment for a period of at least 15 years. A major goal of any design intended for mass production is of course low unit cost. Additionally the experimental logistics demand near zero maintenance requirements from the surface array unit.

In terms of cost efficiency and durability steel is probably the best material available for fabrication of large tanks. It has been suggested that by using stainless steel inexpensive light weight tanks of suitable performance can be constructed. A prototype tank 6.6 $m^2 \times 1.2$ m deep was fabricated at Fermilab using $\approx 2$ mm thick 304L grade material. Problems of water corrosion in the region of the welds were encountered only a few days after filling. However techniques are available which produce welds not susceptible to corrosion, and further investigation is required.

Currently the possibility of using a thicker carbon-steel tank sand-blasted and coated inside and out with several layers of high grade epoxy paint is being investigated. At the time of writing a full scale 10 $m^2$ prototype is under construction. It is proven from experience in the water storage and processing industry that correctly applied epoxy paint of certain grades can withstand water immersion for $> 10$ years. Durability of the paint is enhanced by immersion, as it is by non-exposure to sunlight.

A major factor motivating the use of epoxy paint is the possibility that it can both protect a steel tank from corrosion, and also serve as the reflective internal lining material. Conventional white epoxies use titanium dioxide as the reflective pigment. This has poor reflectivity in the crucial 300 to 400 nm wavelength range, and is not suitable for this application. Investigation is under way to determine if

a suitable pigmentation compound which is epoxy resin miscible can be identified. An epoxy paint containing barium sulphate is being formulated and tested.

If this turns out to be impossible, or if epoxy paint is rejected for some other reason, a galvanized steel tank lined with a reflective sheet material might be considered (much like the Haverah Park tanks). Tyvec, a white fibrous plastic material manufactured by Dupont for various industrial and commercial purposes, has proven diffuse reflectivity, measurements of which are shown in figure 5.7. It also has the advantage of being relatively inexpensive. Consideration is required to find a suitable mechanism which can be used to secure the sheet material to the walls such that it will not be dislodged when 12 tonnes of water are rapidly pumped into the tank.

## 5.7 Water purification and reliability issues

During the construction of the giant ground arrays $\sim 10,000$ tonnes of sufficiently purified water will need to be generated at each site, or brought in from the nearest available source of suitable natural water. The Haverah Park tanks were filled with untreated water from a nearby borehole in magnesium limestone which proved to be perfectly adequate. The transport of water across the array to each individual detector site represents a considerable challenge. It is likely that an extremely large and durable vehicle will have to used. All of these questions are difficult to address until specific sites have been chosen.

Some preliminary tests of water purification via filtration were conducted by the author at Fermilab. A 55 gallon oil drum was adapted for use as a small water Čerenkov tank, a Hamamatsu R1408 200 mm diameter hemispherical PMT being mounted in the center of the top surface. The interior was lined with Tyvec and completely filled with water.

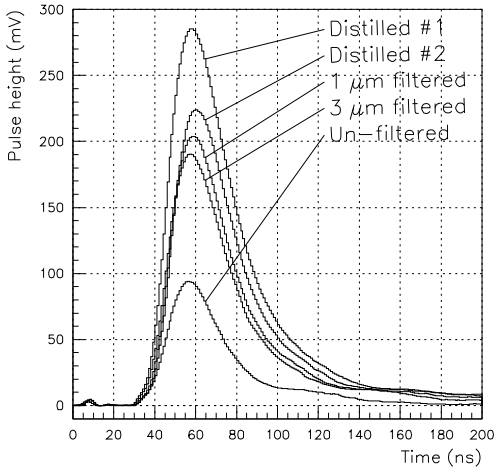


Figure 5.12: *Preliminary Water filtration test results. The time/amplitude profiles shown are each the average of 100 vertically penetrating muon events recorded on a 400 mega sample per second (MSPS) digital oscilloscope. (A cut has been made to remove multiple muon air shower events.)*

The tank was filled with distilled water, unfiltered water from the site mains supply, and mains water passed through a simple disposable cartridge filter. A 4-paddle scintillator telescope was used to trigger readout for vertically penetrating muons passing through the tank. Figure 5.12 shows the average time/amplitude profiles for sets of 100 events collected with each grade of water. Repeatability was checked both for a given fill of water, and also for re-fills of the same type. The filtered water results were found to be fully reproducible. However, it was discovered that some barrels of distilled water from the laboratory stores gave better results than others, presumably due to contamination in the barrels. Two examples are shown, one being little better than the 1 $\mu$m filtered water.

During these tests it was found that even very small amounts of iron oxide contamination have a very adverse effect on the ability of water to transmit light in the important 300 to 500 nm wavelength region. If a steel tank is to be used it is therefore vitally important that the corrosion suppression is perfect. Note that galvanization has proven success in this application.

The possible use of additives to suppress biological activity and prevent problems with freezing needs further consideration. Common salt (sodium chloride) is a promising candidate. It is highly soluble, cheap, and transparent in solution. Concentrated salt solutions are sterile, and freeze only at temperatures $\leq 10^{\circ}$ C. If potassium chloride were to be used instead it may be possible to increase the refractive index of the solution to $\approx 1.5$. This would provide the additional benefits of a $\approx 30\%$ increase in Čerenkov light yield and suppression of non-proportionality effects arising from Čerenkov radiation in the PMT envelope glass. Also the significant reduction of the mean free path for gamma rays would lead to more complete absorption of the electromagnetic shower component.

Another technique which is used to suppress biological activity in water is displacement of the dissolved oxygen by bubbling through nitrogen, combined with the use of a nitrogen over-blanket to prevent re-absorption.

## 5.8 Possible use of wavelength-shifting materials

It may be possible to enhance the performance of the proposed water Čerenkov detector by use of wavelength-shifting materials, either dissolved in the water, incorporated into the tank lining, or coated directly onto the PMT faces. Referring to figure 5.7 we can see that there are many Čerenkov photons in the 200 to 300 nm wavelength region, beyond the reach of a glass encapsulated photomultiplier. If these could be absorbed and re-radiated in the tube response region (300 to 500 nm) a gain in light yield of factor 2 to 3 would be achieved.

The substance 4-Methyl Umbelliferone is probably the best water soluble wavelength-shifter which is known [74, 75]. Concentrations of $\approx 10$ mg $l^{-1}$ reportedly increase light yield by factor $\approx 2$ in Čerenkov detector applications. Importantly,

this particular substance exhibits good long term stability, and the light yield is relatively insensitive to the pH of the solution. However, since the re-radiation from a dissolved wavelength-shifting material is isotropic problems may arise due to pseudo-direct tube face irradiation. A particle whose trajectory passes very close to a PMT will produce an anomalously large number of photoelectrons, leading to a degradation of the proportionality between total radiated Čerenkov light and detected signal. For this reason it may well be preferable to incorporate the wavelength-shifting dye into the tank lining material. The absorption length of water in the wavelength range of interest is still several meters so much of the UV light will reach the tank walls. However, the mean path length to reach a photomultiplier tube is much longer, and hence it is probably not efficient to coat the wavelength-shifter onto the PMT face in this application.

# Chapter 6

## Full simulations of a super-giant water Čerenkov EAS array

The detector simulation program described in Chapter 5 has been used in conjunction with the binned output arrays from shower simulation described in Chapter 4 to generate full simulated experimental data from a super-giant water Čerenkov array. A hexagonal array grid with spacing of 1.5 km between detectors is assumed. The individual detector units are as detailed in sections 5.2 and 5.4. This chapter first outlines the procedure used to generate simulated EAS event data. There follows a description of the Haverah Park experiment this being the only previous giant EAS array based on the water Čerenkov technique. Extensive comparisons are described between the new model calculations and Haverah Park results. These confirm that the simulations may be trusted as a design tool for a next generation experiment, good agreement being demonstrated. Finally some conclusions are drawn and further lines of work and improvements are suggested.

## 6.1 Overview of the simulation procedure

The generation of simulated experimental data is achieved by the following procedure:

- Output from MOCCA is in the form of a ground particle list giving particle type, impact coordinates, trajectory, energy and arrival time. As described in section 4.1 these lists have been used to generate multi-dimensional arrays giving numerical flux density for each particle type in energy/time bins, at intervals of core distance. Figure 4.1 shows an example of the information available in a single annular bin of core distance. These differential density arrays — one for each selected primary type at each zenith angle of incidence — form the starting point of the detector array simulation procedure.

- For each primary type and zenith angle random azimuthal angles and core impact positions are selected, and showers projected onto the simulated array grid. For each detector unit the core distance in the shower plane is calculated and the density array re-sampled to generate a list of shower particles striking the detector, each particle being assigned random impact coordinates on the plane of the detector top surface, and random energy and arrival time within the relevant bin. An interpolation algorithm is used to generate densities at specific core distances since the bins of annular core distance are somewhat coarser than might be preferred (10 logarithmic bins per decade). By sampling over an area in the plane of the detector top surface, but larger than it, all corner-clipping effects are automatically included.

- For each detector unit taking part in an event the detector simulation program described in section 5.3 is invoked using the particles lists as input. Each particle is tracked through the detector volume, interacting and radiating Čerenkov light. The resulting photons are ray-traced until absorbed in the water, upon reflection, or at a PMT. A list of photoelectron release times is updated for each detector.

- The photoelectron lists are used to construct simulated time/amplitude signal profiles for the summed signal from all PMTs as described in section 5.5.

- This profile is then scanned and an alert condition is imposed to simulate the lowest level (hardware) trigger of a detector station. The criterion used is at present somewhat arbitrary, but exploits the time dispersion of EAS fronts at large core distances, and is thought to be simple to implement electronically. A GPS event time-stamp (see Chapter 2) is generated which reflects the fluctuation of the detector trigger time relative to the shower plane arrival.

Figure 6.1 shows the output at the final stage of this process for a single shower. The simulated data thus generated is then available for comparison with experimental results, and event reconstruction.

There are several limitations to the above procedure which should be noted:

- Due to constraints of available processing power and storage space it is not practical to repeatedly simulate the response of individual detectors to more than $\approx 20,000$ particles using the above procedures. For a 10 $m^2$ detector this corresponds to a core distance of $\approx 500$ m from a vertical $10^{19}$ eV event. With an array grid spacing of 1.5 km there will only be one such detector in any given event.

- Note that because the shower input data from MOCCA has already been averaged to overcome the limitations of the thin-sampling technique, intrinsic shower-to-shower fluctuations will not be reproduced (see section 4.1). However, all detector imposed limitations due to limited detector size and non-proportionality of output signal to Čerenkov light release etc. are modelled in this procedure.

Possible resolutions to these problems are discussed in the last section of this chapter.

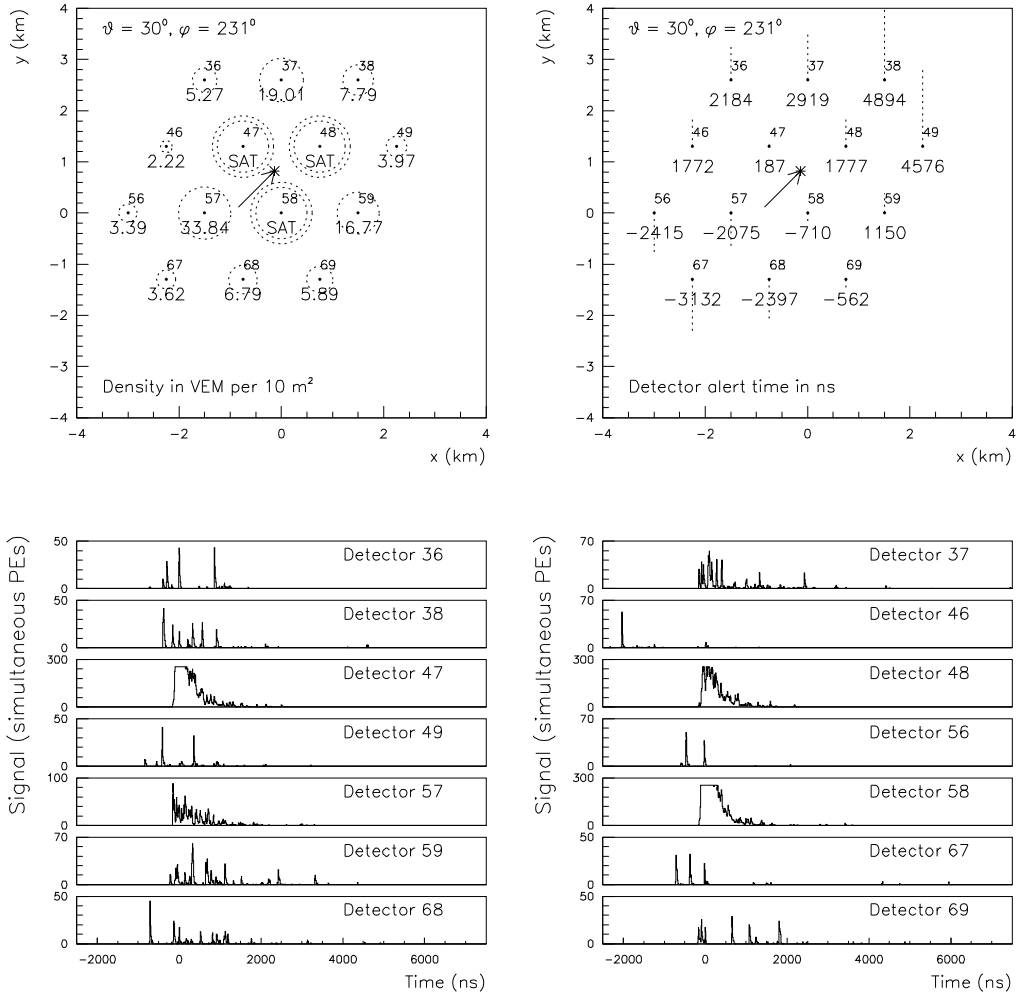


Figure 6.1: *Illustration of a simulated EAS event falling on a giant water Čerenkov surface array. The shower was initiated by a $5 \times 10^{19}$ eV iron nucleus incident at a zenith angle of 30°, the array being close to sea level. The top left plot shows a ground plane density map, the radius of the circles being proportional to the logarithm of the signal density. At top right is a map showing detector trigger times, the length of the vertical lines indicating the time relative to shower core impact. The lower part of the plot gives the simulated time/amplitude signal profiles for each triggered detector.*

## 6.2 Experimental results from Haverah Park

The Haverah Park experiment has already been mentioned in Chapter 5 in connection with the advantages of the water Čerenkov technique, and the lessons which can be learned from it with regard to construction of highly reliable detector units. In this chapter some results from this experiment are used to test the validity of the shower/detector simulation which has been developed so that it may be used with confidence as a design tool for the next generation experiment.

Haverah Park was the only previous giant air shower array employing the water Čerenkov technique. It was located 200 m above sea level at 54° N, in the UK. The 12 km$^2$ array ran from from 1968 to 1987 allowing investigation of many features of EAS structure, development and energy spectrum at energies $> 10^{17}$ eV [24, 29, 30]. The layout of the Haverah Park array is shown in figure 6.2.

### 6.2.1 Lateral distribution function

To reconstruct EAS from the sparse ground level measurements made by a conventional air shower array it is necessary to know the average lateral structure, or lateral distribution function, hereafter referred to as the ldf. The shape of the effective ldf is a function of the actual shower characteristics convolved with the response of the detector medium to the various shower components. Deep water Čerenkov detectors are highly sensitive to the higher energy ($> 1$ GeV) shower muons which produce long radiant track lengths, and at large distances from shower core the observed signal has a significant muonic component. Hence the apparent ldf as measured by a water Čerenkov array is rather different to that measured by a scintillator array.

In the early years of the Haverah Park experiment it became clear [8] that the

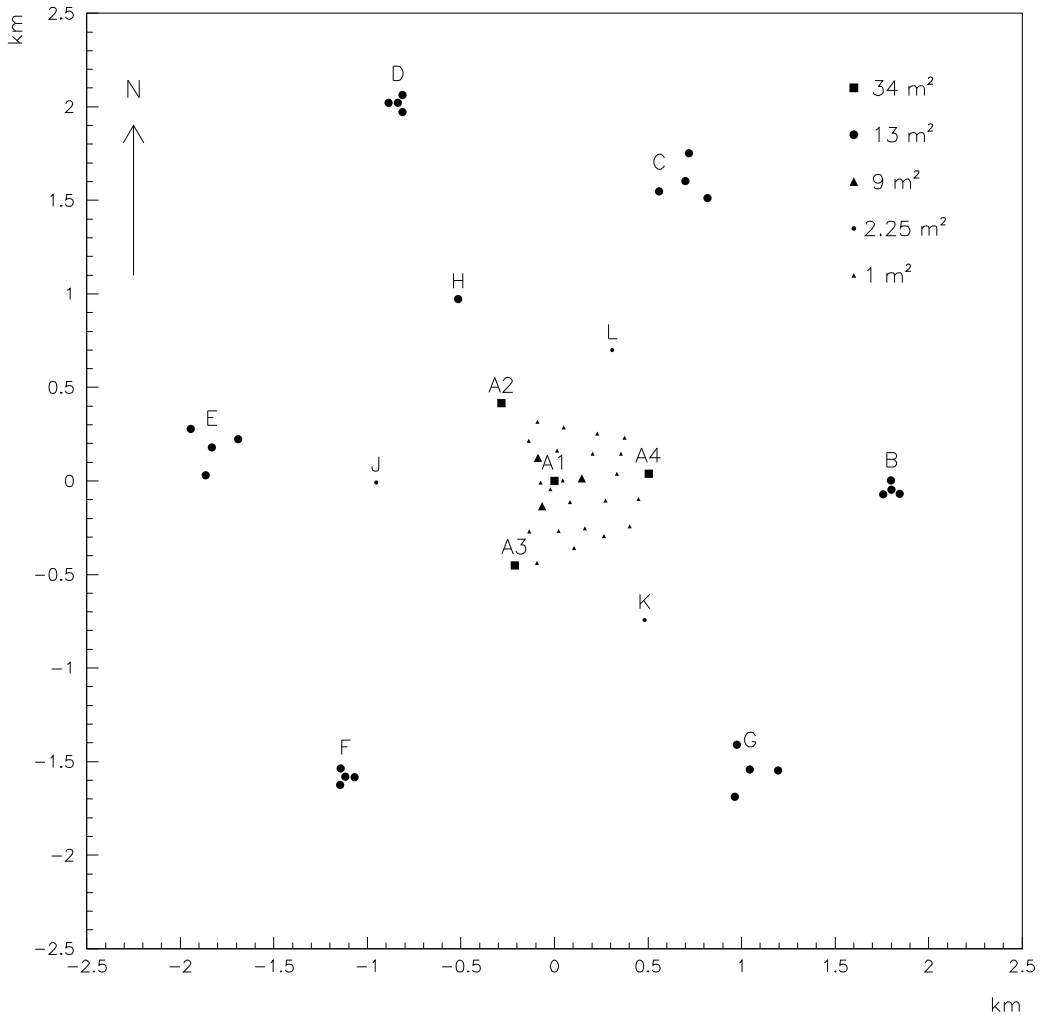


Figure 6.2: *Haverah Park array layout. The locations, areas and names of the major detector units are indicated.*

water Čerenkov ldf was well represented by the empirically derived modified power law function,

$$\rho(r) = kr^{-\left(\eta+\frac{r}{r_0}\right)}, \tag{6.1}$$

where $\rho(r)$ is the signal density at distance $r$ m, and $r_0 = 4000$ m. The slope parameter $\eta$ was observed to be strongly dependent on shower incidence angle $\theta$ according to the relation,

$$\eta = 3.78 - 1.44 \sec\theta. \tag{6.2}$$

The combination of equations 6.1 and 6.2 was shown to be approximately valid for $100 < r < 1000$ m, and $\theta < 60°$.

During the period 1979–1981 a system of $30 \times 1$ m$^2$ detectors was operated in the central part of the array as the "Infill" experiment. With a large number of closely spaced detectors core location by simple arguments of symmetry may be achieved, and very accurate and unambiguous investigation of lateral structure performed. Work by Coy *et al.* [76] led to the measurement of an expected variation of $\eta$ with shower size expressed by,

$$\eta = 3.52 - 1.22 \sec\theta + 0.15 \log(\rho_\lambda(500)), \tag{6.3}$$

where $\rho_\lambda(500)$ is a shower size (energy) parameter which will be discussed below[1]. The combination of equations 6.1 and 6.3 will be referred to as the Coy ldf and was

[1]It follows from the expressions given in this section that $\eta = 3.58 - 1.22 \sec\theta + 0.15 \log(E)$, where $E$ is shower energy expressed in units of EeV. This relationship may be more convenient in future work.

determined in the range $50 < r < 800$ m, $\theta < 45°$ and $2 \times 10^{17} < E < 4 \times 10^{18}$ eV. Use of equation 6.3 to predict $\eta$ for showers of greater energy must be regarded as an extrapolation only.

Note that the above ldfs are average descriptions of lateral structure only. There are, of course, shower-to-shower fluctuations due to fluctuations in the atmospheric depth of the initial primary interactions, and fluctuations in the subsequent cascade development. It is known that $\sigma_\eta$ increases from 0.12 at $\theta = 0°$ to 0.21 at $\theta = 45°$ for showers in the energy range indicated above [76].

Although semi-empirical in origin it is easy to understand equation 6.3 in terms of shower behaviour. As a shower penetrates through the atmosphere the cascade particles are spread laterally by multiple scattering effects. This means that the slope parameter $\eta$ is expected to decrease with increasing zenith angle $\theta$. Conversely, as shower energy increases the region of cascade maximum which is the source of the bulk of shower particles arriving at ground level shifts deeper into the atmosphere. This causes $\eta$ to increase with increasing shower energy. Both these effects are expressed by equation 6.3. In this sense $\eta$ can be termed a shower "age" parameter related to the thickness of atmospheric material through which the shower has passed since reaching maximum development. However, the variation of $\eta$ with energy is small, and can only be observed if the shower core can be accurately located independent of knowledge of $\eta$.

### 6.2.2 Shower attenuation length

The shower attenuation length has already been mentioned in section 5.1 in connection with the advantages of water Čerenkov detectors. The attenuation length $\lambda$ of the signal density at 600 m from shower core was shown to be $760 \pm 40$ g cm$^{-2}$ for the 1.2 m deep Haverah Park detectors [8]. To convert the observed signal

density in a given shower the equation,

$$\rho_\lambda(600) = \rho(600)\exp\left(\frac{1018}{\lambda}(\sec\theta - 1)\right), \tag{6.4}$$

was used, where $\rho_\lambda(600)$ is the "equivalent vertical density", and 1018 g cm$^{-2}$ is the mean atmospheric depth of the array site[2].

### 6.2.3 Event energy assignment

The assignment of primary particle energy to EAS measured only at ground level is necessarily dependent on models of shower cascade development, either analytic or Monte Carlo. Extensive work by Hillas and co-workers established that at $\approx 500$ m from shower core the observed signal density is only weakly dependent on interaction models, and assumptions regarding the mass of the primary particles [77]. Primaries interacting higher in the atmosphere result in showers with flatter lateral distributions at ground level, but which have undergone greater attenuation. At a certain core distance $\rho(r)$ will be equal in showers initiated by both light and heavy primaries. The same is true for shower-to-shower fluctuations between showers of a given primary type. For a wide range of assumptions regarding primary interactions and cascade development this distance is $\approx 500$ m.

There were additional experimental reasons favoring the adoption of the signal density at a distance of $\approx 500$ m as a shower size parameter. When showers are analysed on the basis of an assumed fixed $\eta$ value using a small number of obser-

[2] $\rho_\lambda(600)$ was the routine parameter used to express shower size throughout the Haverah Park experiment. The variation of $\eta$ with shower size expressed in equation 6.3 uses $\rho_\lambda(500)$ as the shower size parameter. This is inconvenient as the ratio of $\rho_\lambda(500)$ to $\rho_\lambda(600)$ depends itself on the value of $\eta$. An iterative process has been used in this work to converge on the correct value of $\eta$ for any given value of $\rho_\lambda(600)$. This is unnecessary and a fixed ratio of 1.8 might equally well be used.

vations the core positions will be shifted from their true locations in an attempt to impose this value on the available data. The assumed value of $\eta$ may be incorrect due either to limited knowledge of the true mean value, or to fluctuations of individual showers from the mean. It turns out that the associated mean shift in $\rho(r)$ is minimal at a distance which is close to the characteristic spacing of a given array setup (see [77, figure 2]). For the Haverah Park 12 km$^2$ array this was determined to be $\approx 600$ m, and hence $\rho(600)$ was chosen as the shower size parameter.

The simplest way to calibrate a water Čerenkov detector is by exploiting ground level background muons using a telescope arrangement of small trigger counters. Hence the unit of signal density adopted was the "vertical equivalent muon" per square meter, or VEM m$^{-2}$.

The early Hillas Monte Carlo results indicated that the conversion between $\rho_\lambda(600)$ and primary particle energy for 1.2 m deep water Čerenkov detectors is given by,

$$E = \beta \rho_\lambda(600)^\alpha, \tag{6.5}$$

where $\beta = 7.04 \times 10^{17}$ eV, and $\alpha = 1.018$. This relationship was used unchanged for all of the Haverah Park work.

### 6.2.4 Exceptional individual showers and the lateral distribution at large core distances

The original purpose of the Infill experiment was to make a detailed investigation of lateral structure at energies in the range $2 \times 10^{17} < E < 4 \times 10^{18}$ eV with the aim of detecting shower-to-shower fluctuations which could be related to the mass

of the cosmic ray primaries. However, a small number of events were collected with much higher energy which fell close to or within the boundary of the infilled array. In such cases the core location error is very small ($\Delta r < 25$ m), and the shower lateral structure is exceptionally well defined with many redundant density measurements not necessary for core location. Figure 6.3 illustrates 4 such events, and shows that there is little evidence of shower asymmetry at larger core distances ($> 100$ m).

The ldfs given in section 6.2.1 are valid only at core distances of $\leq 1$ km. It was not possible to measure densities beyond this distance in the large number of lower energy showers ($\leq 4 \times 10^{18}$ eV) from which these functions were extracted due to the experimental limitations of the detector areas and the recording systems. However, it was noted that in the very largest showers ($> 10^{19}$ eV), where meaningful densities were recorded out as far as 2.5 km from the core, that the extrapolation of the accepted ldfs seriously underestimated the data. This can be clearly seen in figure 6.3 where the predicted lateral distributions calculated on the basis of the Coy ldf are plotted, together with the raw individual density measurements, and the corrected ldf function described below.

Since in conventional analysis of EAS array data each density measurement is assigned a weight proportional to its magnitude these very small, very distant, observations will have negligible effect in showers where several measurements are available much closer to the core. However, this was not the case for the bulk of the Haverah Park data set at the highest energies ($> 10^{19}$ eV), and hence an investigation was conducted by Cunningham to determine an ldf which more accurately reproduced the observations at large distances [78]. The procedure followed was to select events each having several observations within $\approx 300$ m of the core, analyse on the basis of the accepted ldf using only those observations $< 1$ km from the core, and then determine the observed:predicted ratio for each of

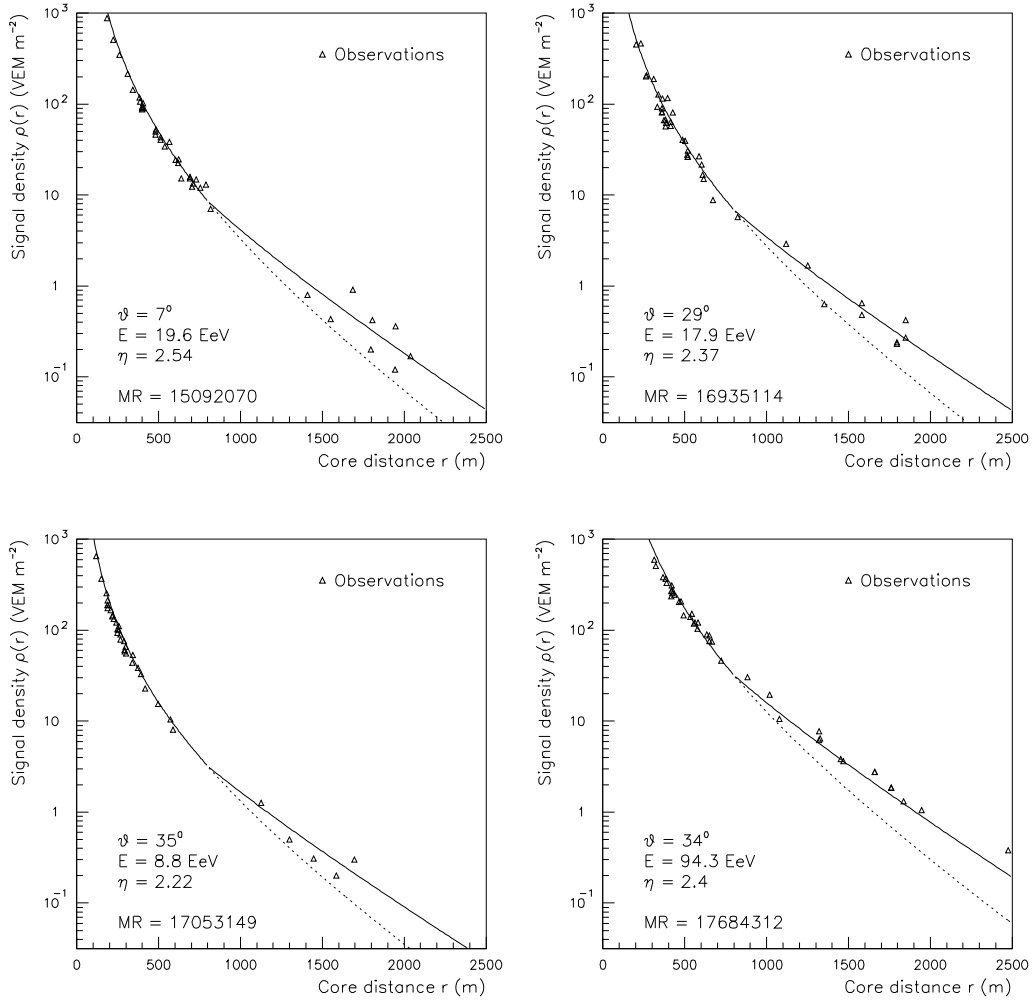


Figure 6.3: *Four exceptional ultra-large EAS recorded by the Haverah Park infilled array. For each event the assigned energy and zenith angle are indicated. The solid lines show the full Coy/Cunningham ldf calculated on the basis of the predicted $\eta$ value shown, the dotted lines which diverge at $r > 800$ m being the uncorrected Coy function. (The MR was an event code number which allowed the calculation of sidereal time.)*

the more distant measurements. The data was binned versus core distance, and a fit made to determine the average flattening of the ldf slope parameter $\eta$ at core distances $> 800$ m.

This work showed that the data could be well represented by flattening the established Coy ldf for $r > 800$ m, while joining smoothly at 800 m, using the equation,

$$\rho(r) = k \left(\frac{1}{800}\right)^{\beta} r^{-\left(\eta + \frac{r}{r_0}\right)+\beta}, \tag{6.6}$$

where $\beta$ was found to be 1.03. Cunningham used the $\approx 4$ years of data taken whilst the Infill experiment was operating in his analysis. The extension of the Coy ldf using equation 6.6 will be referred to as the Coy/Cunningham ldf, and is seen to be a good description of the experimental observations plotted in figure 6.3.

## 6.3 Comparisons of shower/detector simulation with Haverah Park results

The procedure for generating simulated experimental data described in the first section of this chapter has been used to generate batches of 100 events each using the 8 input arrays from the shower simulation runs detailed in Chapter 4. Thus data is available for both proton and iron-initiated showers at zenith angles of 0°, 30°, 45° and 60°. These sets of data have been used to check the agreement between the complete simulation procedure and experimental results from Haverah Park.

Event reconstruction error effects have not been included at this point, the exact core distance of each simulated observation being used to derive the average behaviour of each batch. Note that we do not expect perfect agreement since the

simulated detector unit is not the same size and shape as the Haverah Park units (which were in any case a variety of different effective shapes and sizes). However, in the present case these effects will contribute second order discrepancies only. The mean atmospheric depth of the Haverah Park site is 1018 g cm$^2$, very close to the atmospheric depth assumed in the MOCCA shower simulations of 1000 g cm$^2$ (see section 4.1).

### 6.3.1 Lateral distribution shape and shower attenuation

Figure 6.4 show comparisons of the shower/detector simulation results against the expected ldf shape for vertical showers. The left side of each plot pair shows the simulated data together with the empirical curve. The Coy ldf shape given by equations 6.1 and 6.3 has been used, fitting the normalization constant $k$ to the simulated data in the region $400 < r < 800$ m. For $r > 800$ m the flattened Cunningham extension expressed by equation 6.6 is shown, but the data in this region has not been used in the fit. The right side of each plot shows the ratio of the binned simulated data to the expected ldf shape; the curve shown is a simple polynomial fit intended as a guide to the eye only. For the ratio plot the empirical ldf is not normalized, the expected value of the constant $k$ being calculated using equations 6.5 (the old Monte Carlo energy assignment relation) and 6.4 (the exponential shower decay relation). Also indicated is the value of $r_k$, defined to be the ratio of the (new) simulated and (old) calculated normalization constants, and the expected value of $\eta$ as used. Figure 6.5 is equivalent to figure 6.4 but displays comparisons at zenith angles of 0°, 30°, 45° and 60°.

In figures 6.4 and 6.5 perfect agreement between the simulation results and the empirical ldf would be indicated by a flat line at unity in the ratio plots. However, the energy conversion expressed by equation 6.5 should not be regarded as sacred since this is simply the result of Monte Carlo calculations itself, and more

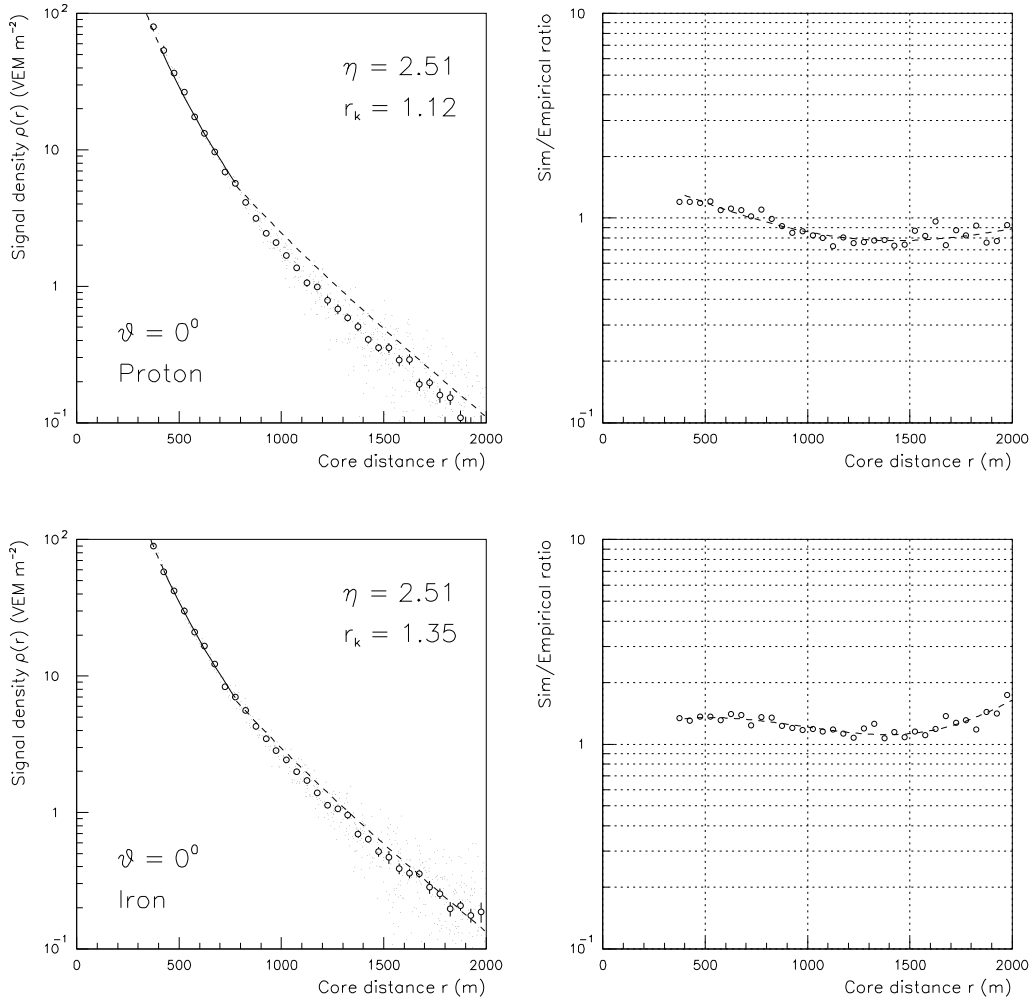


Figure 6.4: *Comparison of shower/detector simulation predictions at 0° zenith angle against the Haverah Park empirical ldf shape. The left hand plots show the raw and binned simulated data together with the Coy/Cunningham ldf shape normalized to produce a best fit in the region $400 < r < 800$ m. The right hand plots show the ratio of the simulation results against the absolute Coy/Cunningham prediction.*

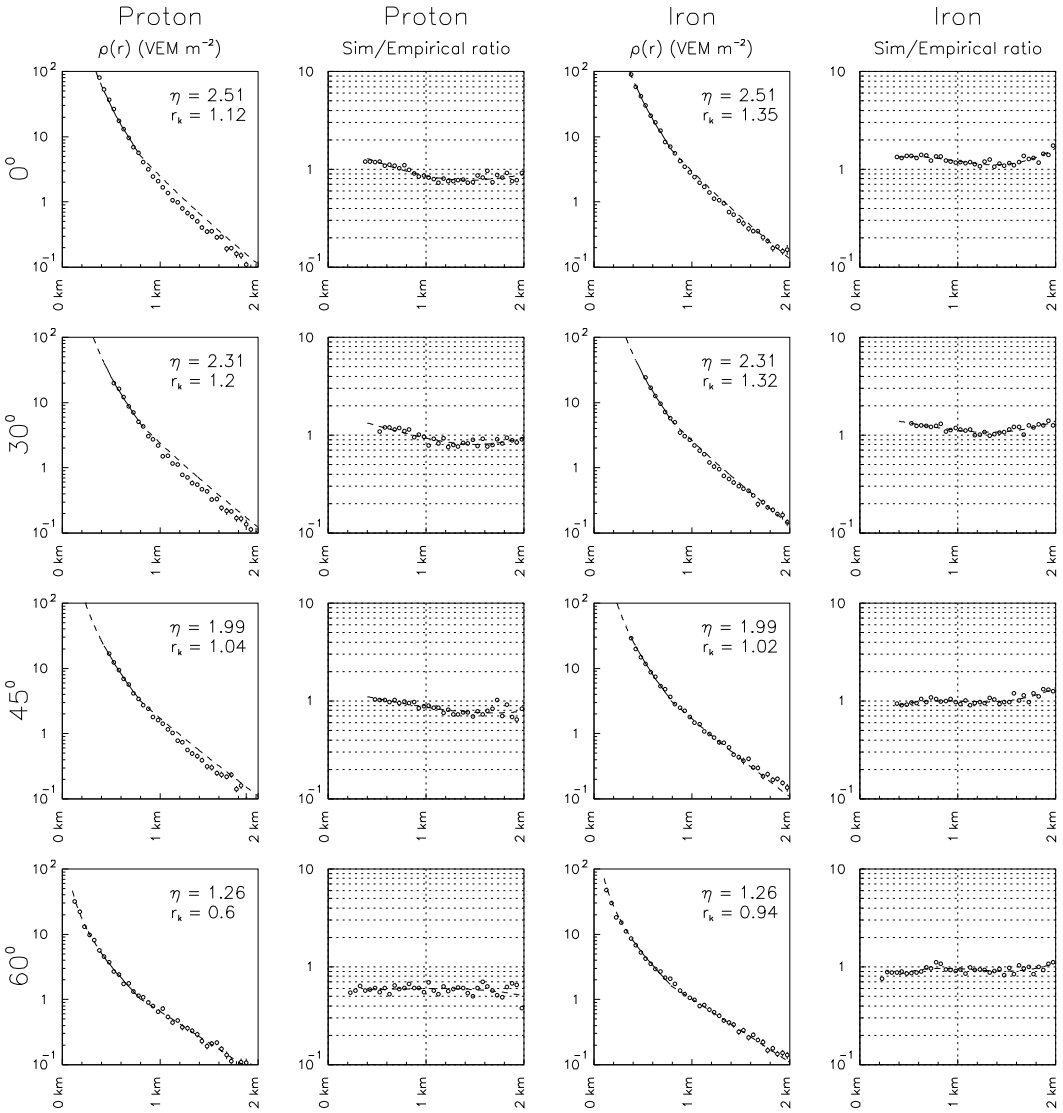


Figure 6.5: *Comparison of shower/detector simulation predictions at 4 zenith angles against the Haverah Park empirical ldf shape. This figure is a super-set of the data displayed in figure 6.4 — refer to the caption for that figure. Plots are shown for both proton and iron-initiated showers. The shower type and quantity being plotted are indicated at the top of each column, and the shower incidence angle to the left of each row.*

than 25 years old. Hence deviation from unity is acceptable although we would expect the deviation to be the same for each primary type at the four zenith angle increments, provided the assumption of exponential shower attenuation expressed by equation 6.4 is correct, and that the value of $\lambda$ used is also correct ($\lambda = 760 \pm 40$ g cm$^{-2}$).

By reference to figure 6.5 we can see that at 0° zenith angle the fit is somewhat better in the case of the iron primary simulations. This is also true at 30° and 45°. By the time we get to 60° both proton and iron-initiated showers exhibit much the same shape. This is as expected since the electromagnetic component has been almost entirely stripped away, and the only difference then predicted between proton and iron-initiated showers is a normalization shift due to their differing initial muonic contents (see figures 4.4 and 4.5).

Of course the better agreement obtained on the assumption of heavy primaries can be interpreted as a limitation of the shower Monte Carlo rather than a real physical result. Hadronic interaction models at these energies rely on extrapolation by several orders of magnitude beyond available accelerator data, and must be regarded as approximate at best. The air shower simulation program CORSIKA produces larger numbers of muons for given primary species, as does MOCCA itself when using the SYBIL hadronic interaction code. This effect might be sufficient to reverse the current situation and produce a better fit for proton primaries; further investigation is required.

The ability of the shower/detector simulation to reproduce the change in ldf slope parameter $\eta$ with increasing zenith angle is encouraging. Note that the expected value of $\eta$ shifts from 2.51 at 0° to 1.26 at 60°; this is a large change, but the simulation results track it rather closely. In table 6.1 the normalization shift results from each of the illustrated simulation runs are summarized. It is

| $\theta$ | $\sec\theta$ | $\frac{\rho(600)}{\rho_\lambda(600)}$ | $\eta$ Coy | $r_k$ p | $r_k$ fe |
|---|---|---|---|---|---|
| 0 | 1.00 | 1.00 | 2.51 | 1.12 | 1.35 |
| 30 | 1.15 | 0.81 | 2.32 | 1.21 | 1.32 |
| 45 | 1.42 | 0.57 | 2.00 | 1.05 | 1.02 |
| 60 | 2.00 | 0.26 | 1.26 | 0.61 | 0.94 |

Table 6.1: *Summary of simulation normalization ratios relative to that expected from equations 6.4 and 6.5. If the simulations were predicting perfectly exponential shower decay $r_k$ would have the same value at each zenith angle. If, in addition, the current simulations were equivalent to original Haverah Park energy calibration calculations $r_k$ would be equal to 1.*

clear that the assumed exponential attenuation of showers in the atmosphere is not cleanly reproduced, and further work might be considered worthwhile on this point. Note that the differing shape and size of the simulated unit and the Haverah Park detectors possibly contributes significantly to the disagreement.

### 6.3.2 Rise time versus core distance

The measurement of shower front time dispersion in terms of a rise time parameter, and the sensitivity of such parameters to the chemical composition of UHECRs has already been discussed in section 4.3.2. At Haverah Park the parameter chosen was $t_{1/2}$, defined as the time taken for the trace to rise from the 10% to the 50% levels relative to the eventual total. Measurements of $t_{1/2}$ were carried out on a routine basis using a photographic technique at the $4 \times 34$ m$^2$ detector sites A1–A4 from 1971 onwards.

Several empirical parameterizations of the dependence of $t_{1/2}$ on shower core distance $r$ are available. Walker and Watson [29] quote a function with six param-

eters valid for $E > 2 \times 10^{17}$ eV and $\theta < 40°$. Additionally two special studies of the largest showers ($E \approx 10^{19}$ eV) where carried out by Walker [79] and Lawrence [80]. For a given shower energy and zenith angle all these expressions reduce to a first order polynomial, whereas the data from which they are extracted shows significant non-linear behaviour. None of the expressions is valid for $\theta > 45°$ as no routine analysis was conducted in this zenith angle range. For these reasons it was decided to compare the simulation results directly against experimental observations extracted directly from the original data archive files.

Figure 6.6 shows a comparison of the shower/detector simulation predictions of $t_{1/2}$ against data from the Haverah Park array. The agreement is good particularly for the simulated iron-initiated showers. However, the same caution which applies to interpretation of the agreement of lateral distribution shape applies here. Since rise times were only measured from the film trace when the signal density was $\geq 1$ VEM m$^{-2}$, and also due to the requirement imposed that the shower core be within 1.5 km of the array center, there are few measurements beyond $\approx 1$ km.

## 6.4 Reconstruction of simulated events

The logical next step from the full simulated experimental data illustrated in figure 6.1 is to attempt event reconstruction in exactly the same manner as would be carried out for real data. By comparing the re-extracted shower parameters to the known initial simulation parameters the experimental performance of a given array system may be assessed. The author has not worked on reconstruction code directly but had significant input into the work of others[3]. A simple approach to shower reconstruction was implemented which proceeds as follows:

[3]The work of which results are presented here was carried out by K. Phuong during the Giant Array design workshop which took place at Fermilab, USA in the first half of 1995

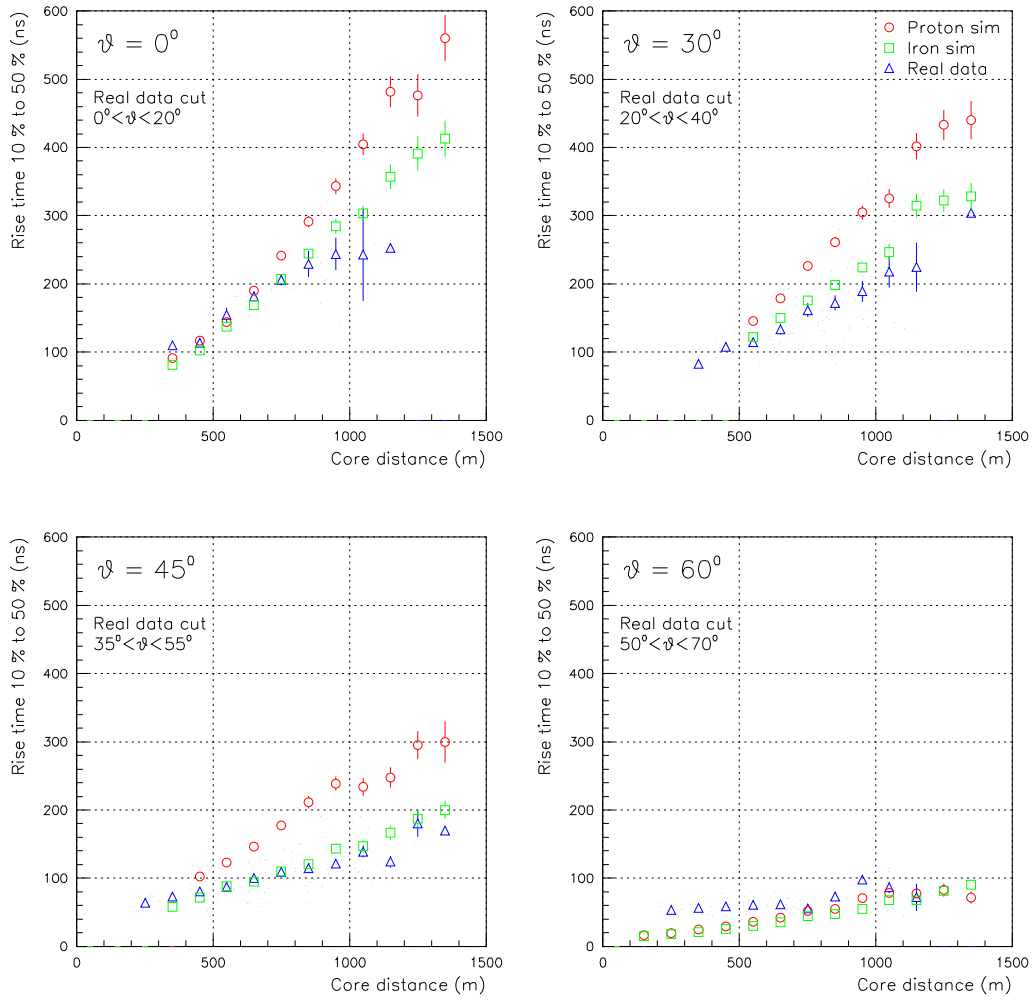


Figure 6.6: *Comparison of shower/detector simulation predictions of signal rise time against experimental data from the Haverah Park array. Each plot shows the binned experimental observations, together with the binned simulated data for both proton and iron-initiated showers. (The raw individual experimental observations are indicated by dots.) A key is shown at top right and is common to all plots. The zenith angle of the simulation runs is noted on each plot, as is the zenith angle cut imposed on the real data. In addition, to ensure data quality and comparability, the real observations are taken only from showers with energy* $5 \times 10^{18} < E < 2 \times 10^{19}$ *eV and with core position less than 1.5 km from the array center.*

- A simple plane fit is made to the simulated GPS event time-stamps to yield shower incidence angles $\theta$ and $\phi$.
- The simulated time/amplitude signal profile from each triggered station is integrated and divided by a conversion factor to yield the signal density measurement in VEM $m^{-2}$.
- Each density measurement is projected into the shower plane.
- A $\chi^2$ minimization fit is made to the density measurements with three free parameters; shower core positions $X$ and $Y$, and shower size parameter $k$. The Coy/Cunningham ldf shape is assumed.
- The fitted $k$ value is converted to the vertical equivalent using using equation 6.4. Finally shower energy is assigned using equation 6.5.

Some reconstruction results are shown in figure 6.7. Runs at energies above and below $1 \times 10^{19}$ eV were made by simply scaling the MOCCA input array density up and down in a linear manner. This figure is included simply to illustrate the questions which may be asked of the shower/detector simulation which has been developed. In the author's opinion the results are unrealistically good; shower-to-shower fluctuations which are at present averaged out at the shower simulation stage will degrade the performance.

## 6.5 Conclusions and suggested further work

A Monte Carlo event generator has been designed and implemented which produces full simulated event data for ultra-large EAS incident on a water Čerenkov ground array. The procedure is able to reproduce several features of the real data set collected by the Haverah Park 12 $km^2$ array, this being the only previous such

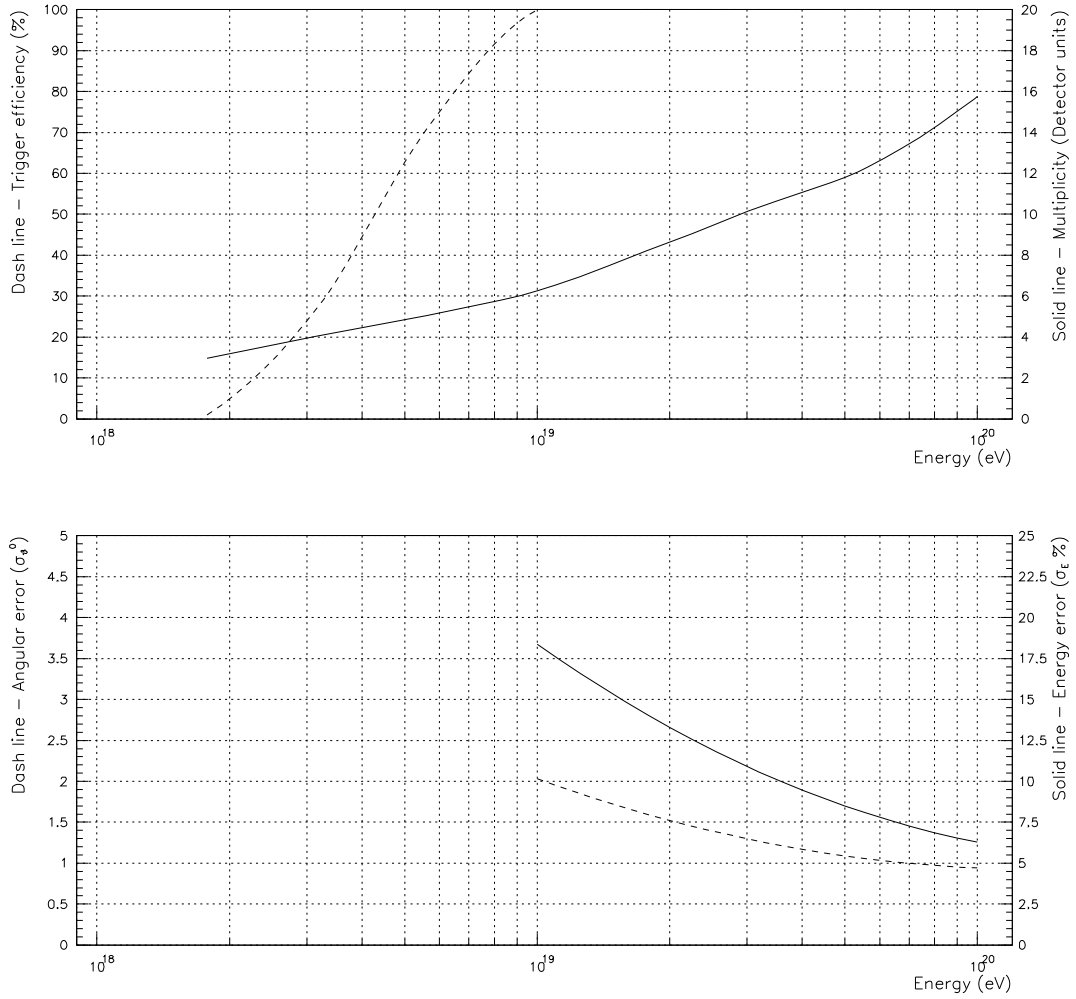


Figure 6.7: *Results of simple EAS reconstruction using simulated event data for proton-initiated showers at 30°. The upper plot shows the array trigger efficiency if > 5 detector units are required to take part in an event. The mean multiplicity of triggered units is also shown. The lower plot shows the predicted angular and energy resolution of the system. Note that $\sigma_E$ as plotted is the random error component only. The assumption of primary mass made in the energy assignment process results in a systematic shift of ≈ 30 % between proton and iron-initiated simulations.*

experiment. The agreement between the predicted and observed lateral distribution shape, and rise time versus core distance, is as good as may be expected given the differing size and shape of the simulated and actual detector units. Given the widely varying effective size and shape of the detector units used in the Haverah Park experiment it is very far from straight forward to account for these effects, and, in the author's opinion, further effort can probably be better expended on other problems. The essential point is that we may have confidence in the use of this, or similar further improved simulation procedures, as design tools for the next generation experiment. For instance it may well be that the selected sites will be at greater altitudes than the Haverah Park site, since the fluorescence detectors, which are to run in conjunction with the water Čerenkov ground arrays, require a degree of atmospheric clarity rarely found at sites close to sea level. Thus direct use of the Haverah Park ldf would be inappropriate, and Monte Carlo techniques would need to be used to predict the expected shape.

In the first section of this chapter two serious remaining limitations of the current simulation procedures were noted; they will be reiterated here and possible solutions discussed. The first problem is the inability of the detector simulation program to handle more than $\approx 20,000$ particle hits on any given detector unit given current limitations of CPU power and online storage capacity. However, detailed time/amplitude profile information is not useful in such cases, and with such large numbers of particles incident, the overall response profile can be calculated in a much simpler manner. Hence the solution to this limitation will be straightforward. The solution of the second limitation will require considerably more effort. It may be possible to modify the shower simulation code to reduce the effective thinning threshold in the core distance range which is of interest for a widely spaced detector array ($> 100$ m) without massively increasing the CPU time required to run each shower. If this can be done it might become possible to use information

extracted from single showers as input to the ground array simulation procedure. This would be the ideal situation which must be worked towards, and would also allow a full simulation of the hybrid ground array/fluorescence detector system to be constructed as an extension of the ground array simulation code.

In section 4.3.1 the possibility of making a direct measurement of the muon to electromagnetic signal ratio via analysis of the time/amplitude profile of a water Čerenkov detector output was discussed. Testing of this proposition was the primary motivation behind the development of the rather sophisticated and CPU intensive simulation code used to generate the output profile of each detector taking part in a simulated event on an event-by-event basis (see figure 6.1). The basic thesis is that in the time dispersed shower front at large core distances the short, large-amplitude pulses produced by penetrating muons passing through the tank may be exploited to make a measurement of the signal fraction which they contribute, for example, and in the simplest possible approach, by counting the number of pulses which exceed some fixed threshold. The author has put considerable effort into an attempt to develop methods of analysis capable of extracting a parameter which correlates with the muon to electromagnetic signal ratio using the simulated detector output profiles as input. The results of all attempts so far have been rather poor.

Any successful parameter must be essentially independent of the total signal density in the distance range where measurement is to be attempted. For this reason several approaches which initially looked promising turned out, on closer inspection, to be illusory. It is not sufficient for a candidate parameter to yield distinctly differing distributions of value when comparing, for instance, proton and iron-initiated showers, of the same energy, at a given core distance. In the distance range where there is sufficient time dispersion ($> 1$ km) the simulated iron-initiated showers yield $\approx 40\%$ greater total signal density than the equivalent

proton-initiated showers (see figure 6.4), largely due to the greater muon content of the iron primary showers. However, if a trace analysis technique is truly measuring the muonic to electromagnetic signal ratio, it will yield differing value distributions at given core distance when, for instance, $5 \times 10^{19}$ eV iron-initiated showers are compared with $7 \times 10^{19}$ eV proton-initiated showers. The parameters investigated so far give poor results when subjected to this test. If a parameter does not pass this test then the separation capability which it shows for proton and iron-initiated showers of equal energy is really no better than to propose separation on the basis of the differing ldf shape via, for instance a simple near:far ratio parameter. For a 1.5 km spaced array it is extremely dubious that core location can be achieved with sufficient accuracy to make this a viable approach.

It is possible to understand the reason for the failure of the parameters so far tested by considering figure 4.2 in conjunction with figure 5.11. Note that although the electromagnetic numerical flux density distribution $dN/dlog(E)$ is dominated by particles having very low energy ($\sim$ 10 MeV) the energy flux density distribution $dE/dlog(E)$ peaks at a much higher energy; i.e. even at large core distances the bulk of the incident electromagnetic signal is carried by particles with energy $\sim$ 100 MeV. Viewing figure 5.11 we can see that at 100 MeV electromagnetic particles are beginning to cross over with penetrating muons in terms of peak pulse height, due to fluctuations in photoelectron yield, light collection time, and pulse height per photoelectron. Hence only a small degree of near-simultaneous arrival (pile-up) will be required for electromagnetic particles to become indistinguishable from muons. By reference to figure 4.8 we can see that even at core distances as great as 1.4 km the bulk of the electromagnetic energy flow occurs within a time period of $\leq 1.5$ $\mu$s.

It has been suggested that better results from the muon:electromagnetic signal separation analysis might be obtained by recording the signal from each PMT

using a separate transient recorder channel, and searching for correlation between the signals as a signature of penetrating muons passing through the tank. In the author's opinion this is unlikely to improve matters considerably; consideration of the points raised in the previous paragraph leads to the conclusion that the required information is simply not available when the detector geometry is as presently assumed. To improve the situation it will be necessary to increase the tank depth to increase the Čerenkov radiant track length of penetrating muons such that they become truly distinct from the electromagnetic particles. This probably implies a corresponding increase in the total area of photocathode which is required if the photoelectron yield per muon is to be maintained (assuming the 7 m attenuation length of water currently used in the simulation does not turn out to be a significant underestimate). Alternatively, or more probably in addition, it will necessary to investigate more complex tank designs having internal segmentation — a "tank-within-a-tank" design springs to mind as one possibility.

However, in the author's opinion, experimental sensitivity to the chemical composition of UHECR primaries based on simple water Čerenkov signal time dispersion, *or other more sophisticated time dispersion parameters*, looks rather promising; see figure 6.6. The opportunity to calibrate the sensitivity of such parameters to the depth of shower maximum $X_{max}$ directly, on a shower-by-shower basis, using coincident observations from the fluorescence detector which is to form an integral part of the next generation experiment, represents an exciting opportunity.

# Bibliography

[1] V. Hess. "Observations of the penetrating radiation on seven balloon flights". *Physik. Zeitschr.*, 13:1804, 1912.

[2] P. Auger et al. "Extensive cosmic-ray showers". *Reviews of Modern Physics*, 11:288–291, 1939.

[3] P. Bassi, G. Clark, and B. Rossi. "Distribution of arrival times of air shower particles". *Physical Review*, 92:441–451, 1953.

[4] G. W. Clarke et al. "Cosmic-ray air showers at sea level". *Physical Review*, 122:637–654, 1961.

[5] J. Linsley and L. Scarsi. "Arrival times of air shower particles at large distances from the axis". *Physical Review*, 128:2384–2392, 1962.

[6] J. Linsley. "Evidence for a primary cosmic-ray particle with energy $10^{20}$ eV". *Physical Review Letters*, 10:146–148, 1963.

[7] R. M. Tennent. "The Haverah Park extensive air shower array". *Proceedings of the Physical Society*, 92:622–630, 1967.

[8] D. M. Edge et al. "The cosmic ray spectrum at energies above $10^{17}$ eV". *Journal of Physics A: Nuclear and General*, 6:1612–1634, 1973.

[9] R. G. Brownlee et al. "Design of an array to record air showers of energy up to $10^{21}$ eV". *Canadian Journal of Physics*, 46:S259–262, 1968.

[10] T. A. Egorov et al. "The Yakutsk EAS complex array". In *Proceedings of the 12th International Conference on Cosmic Rays, Hobart, Australia*, volume 6, pages 2059–2073, 1971.

[11] R. M. Baltrusaitis et al. "The Utah Fly's Eye Detector". *Nuclear Instrumentation and Methods in Physics Research A*, A240:410–428, 1985.

[12] D. J. Bird et al. "Detection of a cosmic ray with measured energy well beyond the expected spectral cutoff due to cosmic microwave radiation". *The Astrophysical Journal*, 441:144–150, 1995.

[13] N. Chiba et al. "Akeno Giant Air Shower Array (AGASA) covering 100 $km^2$ area". *Nuclear Instrumentation and Methods in Physics Research A*, 311:338–349, 1992.

[14] N. Hayashida et al. "Observation of a very energetic cosmic ray well beyond the predicted 2.7 K cutoff in the primary energy spectrum". *Physical Review Letters*, 73:3491–3494, 1994.

[15] B. Rossi and K. Greisen. "Cosmic-ray theory". *Reviews of Modern Physics*, 13:240–309, 1941.

[16] A. M. Hillas. "Shower properties relevant to large arrays". *Nuclear Physics B (Proc. Suppl.)*, 28B:67–73, 1992. (Proceedings of the International Workshop on Techniques to Study Cosmic Rays with Energies Greater than $10^{19}$ eV, Paris, France).

[17] M. Wada, editor. *Catalogue of Highest Energy Cosmic Rays*, volume 1: Volcano Ranch and Haverah Park. World Data Center C2 for Cosmic Rays, Itabashi, Tokyo, Japan, 1980.

[18] D. M. Edge et al. "Improvements to the Haverah Park Array for shower studies in the energy interval $10^{17}$–$10^{18}$ ev". In *Proceedings of the 15th International Cosmic Ray Conference, Plovdiv, Bulgaria*, volume 9, pages 137–142, 1977.

[19] K. Greisen. "Highlights in air shower studies, 1965". In *Proceedings of the 9th International Cosmic Ray Conference, London, England*, volume 2, pages 609–615, 1965.

[20] E. Loh. "The high resolution Fly's Eye Detector". In M. Nagano and F. Takahara, editors, *Proceedings of the ICRR International Symposium: Astrophysical Aspects of the Most Energetic Cosmic Rays, Kofu, Japan*, pages 345–353. World Scientific, 1990.

[21] M. Nagano et al. "Energy spectrum of primary cosmic rays between $10^{14.5}$ and $10^{18}$ eV". *Journal of Physics G: Nuclear Physics*, 10:1295–1310, 1984.

[22] M. Nagano et al. "Energy spectrum of primary cosmic rays above $10^{17.0}$ eV determined from extensive air shower experiments at Akeno". *Journal of Physics G: Nuclear and Particle Physics*, 18:423–442, 1992.

[23] S. Yoshida et al. "The cosmic ray energy spectrum above $3 \times 10^{18}$ eV measured by the Akeno Giant Air Shower Array". *Astroparticle Physics*, 3:105–123, 1995.

[24] M. A. Lawrence, R. J. O. Reid, and A. A. Watson. "The cosmic ray energy spectrum above $4 \times 10^{17}$ eV as measured by the Haverah Park Array". *Journal of Physics G: Nuclear and Particle Physics*, 17:733–757, 1991.

[25] A. A. Watson. "Some statistical problems encountered in the analysis of ultra high energy cosmic ray and ultra high energy gamma ray data". In V. Di Gesù et al., editors, *Data Analysis in Astronomy III*, volume 40 of *Ettore*

*Majorana International Science Series (Physical Sciences)*, pages 335–349. Plenum Press, 1989.

[26] D. J. Bird et al. "The cosmic-ray energy spectrum observed by the Fly's Eye". *The Astrophysical Journal*, 424:491–502, 1994.

[27] K. Asakimori et al. "Energy spectra and composition of cosmic rays above 1 TeV per nucleon". In *Proceedings of the 22th International Cosmic Ray Conference, Dublin, Ireland*, volume 2, pages 57–60, 1991.

[28] J. Linsley and L. Scarsi. "Cosmic-ray composition at $10^{17}$–$10^{18}$ eV". *Physical Review Letters*, 9:123–126, 1962.

[29] R. Walker and A. A. Watson. "Measurement of the elongation rate of extensive air showers produced by primary cosmic rays of energy above $2 \times 10^{17}$ eV". *Journal of Physics G: Nuclear Physics*, 7:1297–1309, 1981.

[30] R. Walker and A. A. Watson. "Measurement of the fluctuations in the depth of maximum of showers produced by primary particles of energy greater than $1.5 \times 10^{17}$ eV". *Journal of Physics G: Nuclear Physics*, 8:1131–1140, 1982.

[31] M. P. Chandler et al. "Primary composition of cosmic rays near $10^{17}$ eV". *Journal of Physics G: Nuclear Physics*, 8:L51–L55, 1982.

[32] M. N. Dyakonov et al. In *"Proceedings of the 23th International Cosmic Ray Conference, Calgary, Canada"*, volume 4, page 303, 1993.

[33] A. A. Watson. "Review of measurements". *Nuclear Physics B (Proc. Suppl.)*, 28B:3–15, 1992. (Proceedings of the International Workshop on Techniques to Study Cosmic Rays with Energies Greater than $10^{19}$ eV, Paris, France).

[34] T. K. Gaisser et al. "Cosmic-ray composition around $10^{18}$ eV". *Physical Review D*, 47:1919–1932, 1993.

[35] D. J. Bird et al. "Evidence for correlated changes in the spectrum and composition of cosmic rays at extremely high energies". *Physical Review Letters*, 71:3401–3404, 1993.

[36] T. Stanev et al. "Arrival directions of the most energetic cosmic rays". *Physical Review Letters*, 75:3056–3059, 1995.

[37] G. Sigl, D. N. Schramm, and P. Bhattacharjee. "On the origin of the highest energy cosmic rays". *Astroparticle Physics*, 2:401–414, 1994.

[38] R. D. Blandford and D. Eichler. *Physics Reports*, 154:1–75, 1987.

[39] E. Fermi. "On the origin of the cosmic radiation". *Physical Review*, 75:1169–1174, 1949.

[40] K. Koyama et al. "Evidence for shock acceleration of high-energy electrons in the supernova remnant SN1006". *Nature*, 378:255–258, 1995.

[41] M. Amenomori et al. "Primary cosmic rays at the knee energy region observed with the Tibet Air Shower Array". In *Proceedings of the 24th International Cosmic Ray Conference, Rome, Italy*, volume 2, pages 736–739, 1995.

[42] W. I. Axford. "The origin of cosmic rays". In M. Nagano and F. Takahara, editors, *Proceedings of the ICRR International Symposium: Astrophysical Aspects of the Most Energetic Cosmic Rays, Kofu, Japan*, pages 406–420. World Scientific, 1990.

[43] A. M. Hillas. "The origin of ultra-high-energy cosmic rays". *Annual Reviews of Astronomy and Astrophysics*, 22:425–444, 1984.

[44] N. S. Kardashev. "Cosmic supercollider". *Monthly Notices of the Royal Astronomical Society*, 276:515–520, 1995.

[45] K. Greisen. "End to the comic-ray spectrum?". *Physical Review Letters*, 16:748–750, 1966.

[46] J. W. Cronin. "Summary of the workshop". *Nuclear Physics B (Proc. Suppl.)*, 28B:213–226, 1992. (Proceedings of the International Workshop on Techniques to Study Cosmic Rays with Energies Greater than $10^{19}$ eV, Paris, France).

[47] G. Sigl, S. Lee, and D. Schramm. "A gap in the highest energy cosmic ray spectrum as a signature of unification scale physics". *Science*, 270:1977–1980, 1995.

[48] J. W. Elbert and P. Sommers. "In search of a source for the 320 EeV Fly's Eye cosmic ray". *The Astrophysical Journal*, 441:151–161, 1995.

[49] The Auger Collaboration. The Pierre Auger Project — design report, October 1995.

[50] M. Schubnell et al. "GRANITE — a stereoscopic imaging Cherenkov telescope system". In *Proceedings of the The Compton Observatory (GRO) Symposium, St. Louis, USA*, 1992. (The Whipple Collaboration).

[51] T. Miller et al. "Initial analysis of coincident events between the SPASE and AMANDA detectors". *Nuclear Physics B (Proc. Suppl.)*, 43:245–248, 1995.

[52] C. Pryke and J. Lloyd-Evans. "A high performance GPS based autonomous event time-tagging system with application in a next generation extensive air shower array". *Nuclear Instrumentation and Methods in Physics Research A*, 354:560–566, 1995.

[53] C. Pryke. "Long baseline testing of a high performance GPS based autonomous event time-tagging system with application in a next generation extensive air shower array". *Nuclear Instrumentation and Methods in Physics Research A*. (To be submitted).

[54] Rockwell International Space Operations and Satellite Systems Division. *ICD-GPS-200, Navstar GPS Space Segment / Navigation User Interfaces*, 1981. (Offical definition of the GPS signal structure and user algorithims).

[55] R. Langley. "Navstar GPS constellation status". CANSPACE, March 1994. (Internet information group).

[56] W. Lewandowski and C. Thomas. "GPS time transfer". *IEEE Special Issue on Time*, 79:991, 1991.

[57] Magnavox Electronic Systems Company. *GPS Engine Integration Guide and Applications Manual*, June 1992.

[58] G. Fidecaro. "The high frequency properties of a coaxial cable and the distortion of fast pulses". *Nuovo Cimento suppl.*, 15:256, 1960.

[59] LeCroy Corporation. "Determining digitizer performance through visual methods". Application Note AN-2005.

[60] Institute of Electrical and Electronic Engineers. "IEEE trial-use standard for digitizing waveform recorders". IEEE Std 1057, July 1989.

[61] LeCroy Corporation. "Understanding effective bits". Technical note CSD-004, 1990.

[62] H. B. Crawley et al. "Testing ADC's at sample rates from 20 to 120 MSPS". *IEEE Transactions on Nuclear Science*, 40:729–732, 1993.

[63] A. M. Hillas. "Two interesting techniques for Monte-Carlo simulation of very high energy hadron cascades". In *Proceedings of the 17th International Cosmic Ray Conference, Paris, France*, volume 8, pages 193–196, 1981.

[64] A. M. Hillas. "The MOCCA program: MOnte-Carlo CAscades". In *Proceedings of the 24th International Cosmic Ray Conference, Rome, Italy*, volume 1, pages 270–272, 1995.

[65] E. W. Kellermann and L. Towers. "The electromagnetic component of large air showers". *Journal of Physics A: General Physics*, 3:284–295, 1970.

[66] A. V. Glushkov et al. "The $\rho_{600}$ spectrum and primary energy spectrum at $E_0 > 10^{17}$ eV". In *Proceedings of the 20th International Cosmic Ray Conference, Moscow, USSR*, volume 5, pages 494–497, 1987.

[67] B. Rossi. *High-Energy Particles*. Prentice-Hall Inc., 1952.

[68] Particle Data Group. "Review of particle properties". *Physical Review D*, 50(3), August 1994.

[69] W. Nelson, H. Hirayama, and D. Rogers. "The EGS4 code system". Technical Report SLAC-Report-265, Stanford Linear Accelerator Center, Stanford, California, 1985.

[70] S. Seltzer and M. Berger. "Improved proceedure for calculating the collision stopping power of elements and compounds for electrons and positrons". *International Journal of Applied Radiation and Isotopes*, 35:665–676, 1984.

[71] J. V. Jelley. *Čerenkov radiation and its applications*. Pergamon Press, 1958.

[72] R. C. Smith and K. S. Baker. "Optical properties of the clearest natural waters". *Applied Optics*, 20:177–184, 1981.

[73] Philips Photonics. *Photomultiplier tubes principles and applications*. Philips B.V., 1994.

[74] M. Takiue, H. Fujii, and H. Ishikawa. "PPO-ethanol system as wavelength shifter for the Cherenkov counting technique using a liquid scintillation

counter". *Nuclear Instruments and Methods in Physics Research*, 227:571–575, 1984.

[75] N. A. Porter. "The effect of ultra-violet converters on the efficiency of liquid Cerencov counters. *Il Nuovo Cimento*, 5:526–527, 1957.

[76] R. N. Coy et al. "The average properties and fluctuations of the lateral distribution of large air showers". In *Proceedings of the 17th International Cosmic Ray Conference, Paris, France*, volume 6, pages 43–46, 1981.

[77] A. M. Hillas et al. "Measurement of primary energy of air showers in the presence of fluctuations". In *Proceedings of the 12th International Cosmic Ray Conference, Hobart, Australia*, volume 3, pages 1001–1006, 1971.

[78] G. Cunningham. *The cosmic ray spectrum above $10^{17}$ eV*. PhD thesis, The University of Leeds, 1982.

[79] R. Walker. *Longitudinal Development of EAS Initiated by Primaries above $10^{17}$ eV*. PhD thesis, The University of Leeds, 1981.

[80] M. A. Lawrence. *The Development and Evaluation of New Analytic and Experimental Techniques for the Study of the Highest Energy Cosmic rays*. PhD thesis, The University of Leeds, 1988.